SEARCHES FOR POINT-LIKE SOURCES OF NEUTRINOS WITH THE 40-STRING ICECUBE DETECTOR

by

JONATHAN P. DUMM

A dissertation submitted in partial fulfillment of the
requirements for the degree of

DOCTOR OF PHILOSOPHY
(PHYSICS)

at the

UNIVERSITY OF WISCONSIN – MADISON

2011

Searches for Point-like Sources of Neutrinos with the 40-String IceCube Detector

Jonathan P. Dumm

Under the supervision of Professor Teresa Montaruli
At the University of Wisconsin – Madison

The IceCube Neutrino Observatory is the first 1 km^3 neutrino telescope. Data were collected using the partially-completed IceCube detector in the 40-string configuration recorded between 2008 April 5 and 2009 May 20, totaling 375.5 days livetime. An unbinned maximum likelihood ratio method is used to search for astrophysical signals. The data sample contains 36,900 events: 14,121 from the northern sky, mostly muons induced by atmospheric neutrinos and 22,779 from the southern sky, mostly high energy atmospheric muons. The analysis includes time-integrated searches for individual point sources and targeted searches for specific stacked source classes and spatially extended sources. While this analysis is sensitive to TeV–PeV energy neutrinos in the northern sky, it is primarily sensitive to neutrinos with energy greater than about 1 PeV in the southern sky. A number of searches are performed and significances (given as p-values, the chance probability to occur with only background present) calculated: (1) a scan of the entire sky for point sources (p=18%), (2) a predefined list of 39 interesting source candidates (p=62%), (3) stacking 16 sources of TeV gamma rays observed by Milagro and Fermi, along with an unconfirmed hot spot (p=32%), (4) stacking 127 starburst galaxies (p=100%), and (5) stacking five nearby galaxy clusters (p=78%). No evidence for a signal is found in any of the searches. Limits are set for neutrino fluxes from astrophysical sources over the entire sky and compared to predictions. The sensitivity is at least a factor of two better than previous searches (depending on declination), with 90% confidence level muon neutrino flux upper limits being between $E^2 dN/dE \sim 2-200 \times 10^{-12}$ TeV cm^{-2} s^{-1} in the northern sky and between $3-700 \times 10^{-12}$ TeV cm^{-2} s^{-1} in the southern sky. The stacked source searches provide the best limits to specific source classes. For the case of supernova remnants, we are just a factor of three from ruling out realistic predictions. The full IceCube detector is expected to improve the sensitivity to E^{-2} sources by another factor of two in the first year of operation.

Teresa Montaruli (Adviser)

Abstract

The IceCube Neutrino Observatory is the first 1 km^3 neutrino telescope. Data were collected using the partially-completed IceCube detector in the 40-string configuration recorded between 2008 April 5 and 2009 May 20, totaling 375.5 days livetime. An unbinned maximum likelihood ratio method is used to search for astrophysical signals. The data sample contains 36,900 events: 14,121 from the northern sky, mostly muons induced by atmospheric neutrinos and 22,779 from the southern sky, mostly high energy atmospheric muons. The analysis includes time-integrated searches for individual point sources and targeted searches for specific stacked source classes and spatially extended sources. While this analysis is sensitive to TeV–PeV energy neutrinos in the northern sky, it is primarily sensitive to neutrinos with energy greater than about 1 PeV in the southern sky. No evidence for a signal is found in any of the searches. A number of searches are performed and significances (given as p-values, the chance probability to occur with only background present) calculated: (1) a scan of the entire sky for point sources (p=18%), (2) a predefined list of 39 interesting source candidates (p=62%), (3) stacking 16 sources of TeV gamma rays observed by Milagro and Fermi, along with an unconfirmed hot spot (p=32%), (4) stacking 127 starburst galaxies (p=100%), and (5) stacking five nearby galaxy clusters, testing four different models for the CR distribution (p=78%). Limits are set for neutrino fluxes from astrophysical sources over the entire sky and compared to predictions. The sensitivity is at least a factor of two better than previous searches (depending on declination), with 90% confidence level muon neutrino flux upper limits being between $E^2 dN/dE \sim 2 - 200 \times 10^{-12}$ $\mathrm{TeV\,cm^{-2}\,s^{-1}}$ in the northern sky and between

$3-700\times10^{-12}$ TeV cm^{-2} s^{-1} in the southern sky. The stacked source searches provide the best limits to specific source classes. For the case of supernova remnants, we are just a factor of three from ruling out realistic predictions. The full IceCube detector is expected to improve the sensitivity to E^{-2} sources by another factor of two in the first year of operation.

Acknowledgements

I dedicate this work to my brother, Dennis. He taught me so much, and I'm still trying to figure out how much of it is actually true.

I would first like to thank my parents, Brad and Sue, for working so hard to provide endless opportunities for me. I would also like to thank my wife, Jess, for her love and support through all this work. I am little without her.

I owe a debt of gratitude to my advisor, Teresa Montaruli, not only because of her guidance and support for six years, but also because of her dedication to the field of neutrino astronomy. She is truly inspiring.

Thanks to my early mentors, Juande Zornoza and, in particular, Chad Finley, for introducing me to the world of likelihood analysis and for his immense intellectual curiosity. Also David Boersma, whose expertise in computing and generosity with time have helped so many.

It has been a pleasure working closely with Mike Baker, Juanan Aguilar, and Naoko Kurahashi on the point source analysis. I would like to thank Hagar Landsman for introducing me to DOM testing and preparing me to work on hardware at the South Pole. Thanks to all the others who make Madison such a terrific place to work on IceCube and a terrific place to live.

Finally, it takes many people to make IceCube a reality. I would like to thank all members of the IceCube Collaboration for their dedication over the years.

Contents

Chapter 1

Neutrino Astronomy and the High Energy Universe

This chapter introduces neutrino astronomy and concepts related to the high energy universe. Since neutrinos and cosmic rays (CRs) are likely to share the same origins, this connection is discussed in some detail. Potential CR acceleration sites and underlying acceleration mechanisms are discussed. Neutrino production from CR interactions is described, and recent results of diffuse neutrino searches are shown.

Neutrino astronomy is only just beginning. It has the possibility to open a new window on the universe, expanding what is possible to know about astrophysical phenomena. The role of neutrinos as astrophysical messengers is shown in figure 1.1. In the scenario shown, gamma rays, charged CRs, and neutrinos all share the same origin. CRs are deflected by magnetic fields. Gamma rays can be absorbed by intervening material or pair produce on photon backgrounds prevalent throughout the universe. Neutrinos suffer from neither problem since they are neutral and only interact via the weak force.

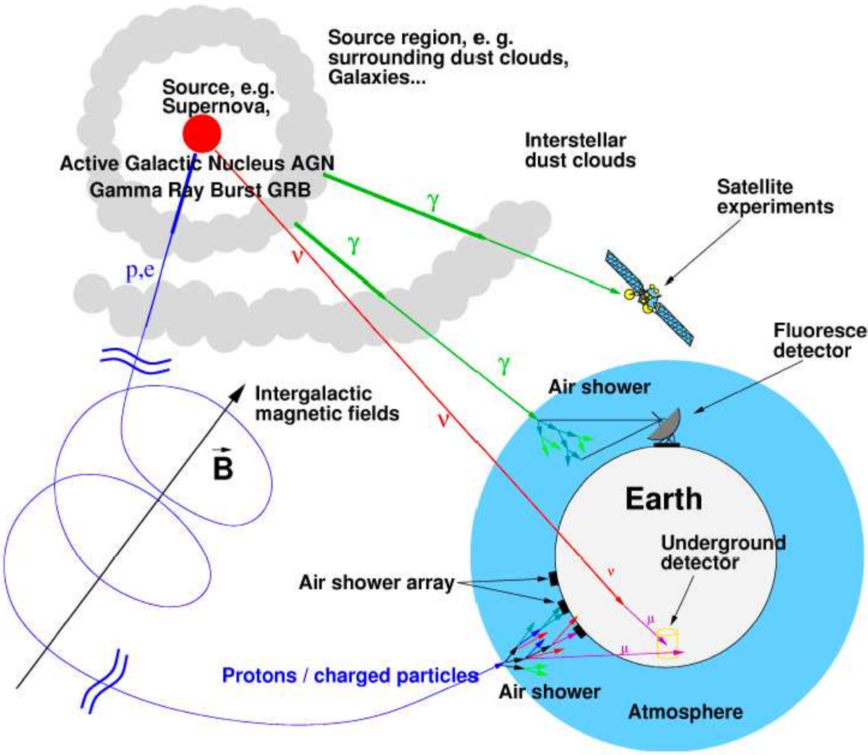

Figure 1.1: The role of neutrinos in high energy multi-messenger astronomy. All messengers share the same possible origin. Cosmic rays are deflected by magnetic fields, and gamma rays are absorbed by matter or photon backgrounds. Neutrinos overcome both of these problems. Whereas neutrinos would be a definitive signature for cosmic ray acceleration, gamma ray emission is potentially leptonic rather than hadronic. Image Credit: Wolfgang Rhode.

1.1 The Neutrino

The neutrino is a neutral particle, the least massive particle in the standard model, and only rarely interacts through the weak force. The invention of the neutrino is due to Wolfgang Pauli, who in 1930 proposed the existence of the neutrino as a solution to the problem of the continuous beta decay spectrum. This spectrum would not be expected from a two-body decay, so he reasoned there must be a third, nearly undetectable, nearly massless particle emitted during the decay process.

The first observation of the neutrino was finally made in 1956 [1]. The experiment made use of the expectation that nuclear reactors would produce large fluxes of antineutrinos ($\sim 10^{13}$ cm^{-2}s^{-1}). These interact with protons to produce neutrons and positrons, which annihilate with electrons to produce two 0.5 MeV gamma rays. The neutrons were also detected as a third gamma ray, following absorption by Cadmium and the subsequent decay of the excited state. Detecting all three gamma rays, the third delayed by 5×10^{-6} s with respect to the first two, was a distinctive signature for neutrino interactions.

Shortly after the discovery of the neutrino, by examining its properties it became clear that the neutrino could be an excellent tool for astronomy. Because neutrinos have such a low probability for interaction, they are not absorbed as easily as gamma rays. And because neutrinos are neutral, they are not deflected as cosmic rays. However, the small cross section also necessitated the construction of large detectors, technically difficult to construct.

1.2 Solar Neutrinos

The nuclear reactions that power the Sun produce an intense flux of electron neutrinos. The Sun is in its stable hydrogen burning phase and the net result of these reactions is

$$4p \rightarrow^4 \mathrm{He} + 2e^+ + 2\nu_e. \tag{1.1}$$

The average energy of the resulting neutrinos is $\sim$ 0.6 MeV. Many other reactions contribute as well and are summarized in figure 1.2.

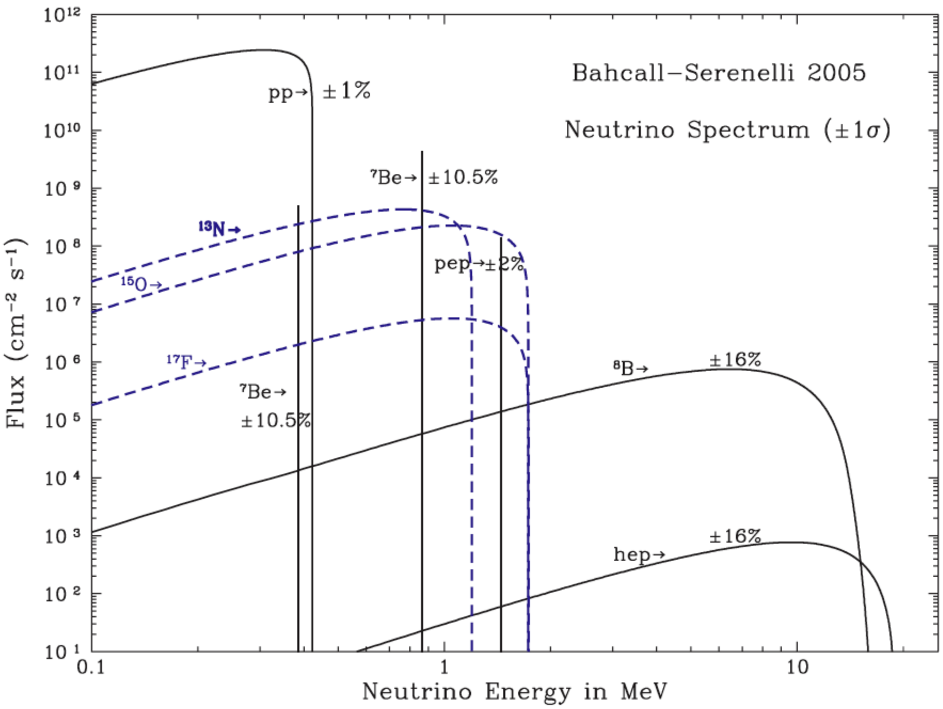

Figure 1.2: The solar neutrino spectrum predicted in the standard solar model [2], figure taken from [3]. Fluxes at one astronomical unit from continuum sources are in units of number cm^{-2} s^{-1} MeV^{-1}, and the line sources are in number cm^{-2} s^{-1}.

Observing solar neutrinos provided the opportunity to directly address the theory of stellar structure and evolution. Predictions of the neutrino flux coming from the Sun originated in the standard theory of stellar evolution. Sophisticated calculations produce predictions for an observable number of neutrino interactions with $\sim 10\%$ uncertainty [2].

In the late 1960s, Davis and collaborators started a pioneering solar neutrino experiment. They looked for neutrino absorption by Chlorine:

$$^{37}\mathrm{Cl} + \nu_e \rightarrow ^{37}\mathrm{Ar} + e^{-}(\mathrm{threshold}\,814\,\mathrm{keV}). \tag{1.2}$$

The Argon is radioactive with a half-life of 34.8 days. The Argon is chemically extracted from the Chlorine after two or three months and radioactivity was detected with proportional counters.

It was recognized from the beginning that the observed flux was significantly smaller than the prediction [4]. The observed fraction was roughly one-third as many as the solar model predicted, and this deficit was called "the solar-neutrino problem." This problem went on unresolved for 30 years.

In 2002, the SNO collaboration reported direct evidence for flavor oscillations by measuring all three neutrino flavors [5]. The sum of all three flavors reproduced the predicted electron neutrino flux. It was suggested originally by Bruno Pontecorvo in the 1950s that if neutrinos have mass, there could be flavor oscillations. However, it required accurate measurements of solar neutrinos to finally determine that this was the case. The fact that neutrinos have mass is still one of the great breakthroughs of the last couple decades in physics.

1.3 Supernova 1987A

The second observation of extraterrestrial neutrinos occurred in 1987, when a blue giant in the Large Magellanic Cloud turned into the brightest supernova observed from Earth in the last several hundred years. Such supernovae occurring within the galaxy are only thought to occur just about 1.9 ± 1.1 times per century, based on observations of radioactive Aluminum-26 synthesized in the explosions [6]. Prior to 1987, the last recorded supernova occurred in 1604. So it was fortunate that the first generation of neutrino detectors were operational in 1987.

Three hours before the first light from the supernova was observed, three detectors simultaneously saw a large excess of neutrinos over background. Kamiokande II detected 11, IMB detected 8, and Baksan detected 5 antineutrino events, all within about a 15 second window. These data provided a historic opportunity for determining the dynamics of how a supernova works (such as the existence of accretion and cooling phases) [7]. The data also provided new information about neutrinos themselves. In particular, the dispersion of the event arrival times allowed the construction of an upper limit on the electron neutrino mass, ranging from 5 eV – 30 eV, depending on interpretation of the events in the tail of the arrival time distribution [8, 9].

1.4 Cosmic Rays

Cosmic rays (CRs) have an important connection to neutrino astronomy, as the origins of each are likely the same. For that reason, we need to understand what we can regarding the CRs.

Charged CRs are high energy particles traveling throughout the universe. The existence of "cosmic radiation" was established nearly 100 years ago. By monitoring the rate of electroscope discharge at various altitudes, Hess demonstrated that the rate of radiation began increasing above 1 km [10]. This established that radiation was coming from extraterrestrial sources, earning him the Nobel Prize in 1936. The precise origins of CRs are still uncertain.

1.4.1 Cosmic Ray Flux and Composition

The flux of CRs observed at earth spans from about 1 GeV up to 10^{11} GeV. Observations have been carried out by a large number of experiments, some using balloons or satellites to measure the CRs directly. At higher energies the CRs must be observed from ground-based instruments that monitor large volumes of atmosphere. The CR flux measurements are summarized in figure 1.3.

The flux is non-thermal, rather following a power law spectrum with

$$d\Phi/dE \propto E^{-\gamma}. \tag{1.3}$$

Two changes to the spectrum are visible, called the "knee" and the "ankle," labeled in figure 1.3. The spectral indices are [11]:

$$\gamma = \begin{cases} 2.67 & \log(E/GeV) < 6.4, \\ 3.10 & 6.4 < \log(E/GeV) < 9.5, \\ 2.75 & 9.5 < \log(E/GeV). \end{cases} \tag{1.4}$$

The region between the knee and ankle is thought to be due to a change in the CR sources. This is motivated by the maximum energy that galactic sources, such as supernova remnants (SNRs), can accelerate CRs [12]. For example, a phenomenological model of a rigidity-dependent cutoff in the CR spectrum represents the flux near the knee well [13]. Interstellar magnetic fields also lose their ability to contain the charged CRs within the galaxy around the energy of the knee. The ankle is thought to be the region where the flux from extragalactic sources dominates over galactic sources. Extragalactic sources such as active galactic nuclei (AGN) and gamma ray bursts (GRBs) are potentially capable of accelerating CRs to the highest observed energies. Finally, the CR flux is highly suppressed above 5×10^{10} GeV by the Greizen-Zatsepin-Kuzmin (GZK) mechanism [14]. Above that energy, cosmic ray protons begin to interact with cosmic microwave background photons to produce pions.

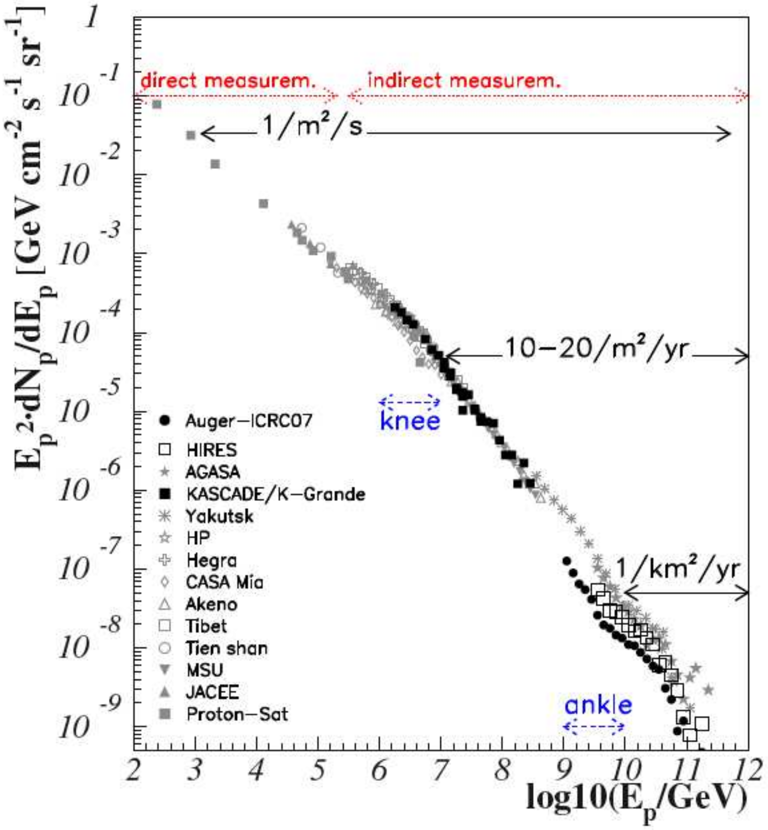

Figure 1.3: All particle cosmic ray flux as measured by a variety of experiments, from [15] and references therein. The flux has been multiplied by E^2 to enhance spectral features noted in the text.

About 79% of the CRs detected at Earth are protons [16]. Helium nuclei are the second-most abundant at 15%, then electrons at 2%. The last 4% are elements heavier than helium. Work is still being done to determine the elemental composition at energies around the knee. Of particular interest are observed excesses in the number of electrons and positrons, that could be signatures for nearby CR sources or potentially dark matter [17, 18]. Recent direct measurements of the CR spectra for protons and helium prove to be somewhat difficult to explain in either the linear or non-linear diffusive shock acceleration models since the protons and helium seem to follow separate power law spectral indices [19].

The flux of charged CRs at Earth is nearly isotropic, since galactic and extragalactic magnetic fields scramble the CR arrival direction. A small anisotropy in arrival directions of TeV CRs has been observed, most likely caused by local magnetic field structure or a nearby CR source [20]. An anisotropy has been reported by the Pierre Auger Observatory at the highest observed energies [21]. Although our limited knowledge of astrophysical magnetic fields limits our ability to make precise predictions, it is possible that CRs at 10^9 GeV should only undergo a small deflection, on the order of a few degrees. Searches for neutrinos in correlation with these ultra high energy CRs (UHECR) have been performed [22], accounting for some deflection from the true origin.

1.4.2 Cosmic Ray Acceleration

There are two broad categories for the possible origins of CRs:

- **Top-down:** Very massive particles with long lifetimes decay to high energy CRs.
- **Bottom-up:** Select low energy particles are accelerated by energetic astrophysical phenomena.

Potential sources of supermassive particles in the top-down scenario could be topological defects created in the early universe [23] or heavy dark matter [24, 25]. The top-down scenario is becoming constrained on many fronts. Existing limits on ultra high energy neutrinos rule out top-down models at cosmological distances [26]. The possibility of the UHECRs being created in the galactic halo is excluded by the observation of the GZK cutoff, since the suppression of the UHECR flux above 5×10^{10} GeV due to interactions with cosmological backgrounds [14] would not be observed if the sources were nearby. Photons would likely also be observed if the decays were nearby, and strict limits now exist at these high energies [27].

The most widely accepted bottom-up acceleration mechanism is one proposed by Fermi [28]. First order Fermi acceleration energizes charged particles through interactions with shock waves. Turbulent magnetic fields can form "magnetic mirrors," confining particles to the shock region. The compression between the shocked and unshocked regions means that the CRs gain energy for reflection across the shock. Linear acceleration models predict a power law flux with spectrum

$$d\Phi/dE \propto E^{-2}, \tag{1.5}$$

with even harder spectra coming from some non-linear acceleration models that allow the CRs to modify their environment while being accelerated [29].

The particle is no longer magnetically confined when the gyroradius exceeds the size of the acceleration region. This sets a limit to the energy particles can be accelerated up to. The gyroradius (or Larmor radius) is given by

$$R = \frac{p}{qB_\perp} = \frac{E/c}{ZeB_\perp}, \tag{1.6}$$

So we can write an expression for the maximum achievable energy in an astrophysical environment:

$$\frac{E_{\mathrm{max}}}{\mathrm{GeV}} \simeq 3 \times 10^{-2} \times Z \times \frac{R}{\mathrm{km}} \times \frac{B}{G}. \tag{1.7}$$

This maximum energy is proportional to the charge of the CR, the size of the acceleration region, and the magnetic field strength. This relation is illustrated in figure 1.4 for potential CR sources.

1.4.3 Candidate Cosmic Ray Accelerators

The two criteria for being a CR candidate accelerator are the presence of compressive shock fronts and magnetic confinement. These are the ingredients that lead to first order Fermi acceleration. From the Hillas diagram in figure 1.4 we can tell there are a large number of potential cosmic ray accelerators. The most promising include:

- **Supernova Remnants (SNR)**: Supernovae are the most powerful explosions in the galaxy, thought to convert about 10^{50} erg into particle acceleration. This conversion can take place in the diffusive shocks that live 10s of thousands of years [31]. The remnants that result from these explosions can be categorized by the presence of a central pulsar with a relativistic wind powering the pulsar wind nebula (PWN) or by their shell-like appearance. Two of the most famous examples of the two types are the Crab PWN and the shell-like Cas A. Many are observed in TeV gamma rays [31, 32, 33, 34].

- **Microquasars**: Powered by the accretion of matter onto a central neutron star or black hole up to a few solar masses, microquasars produce relativistic outflows

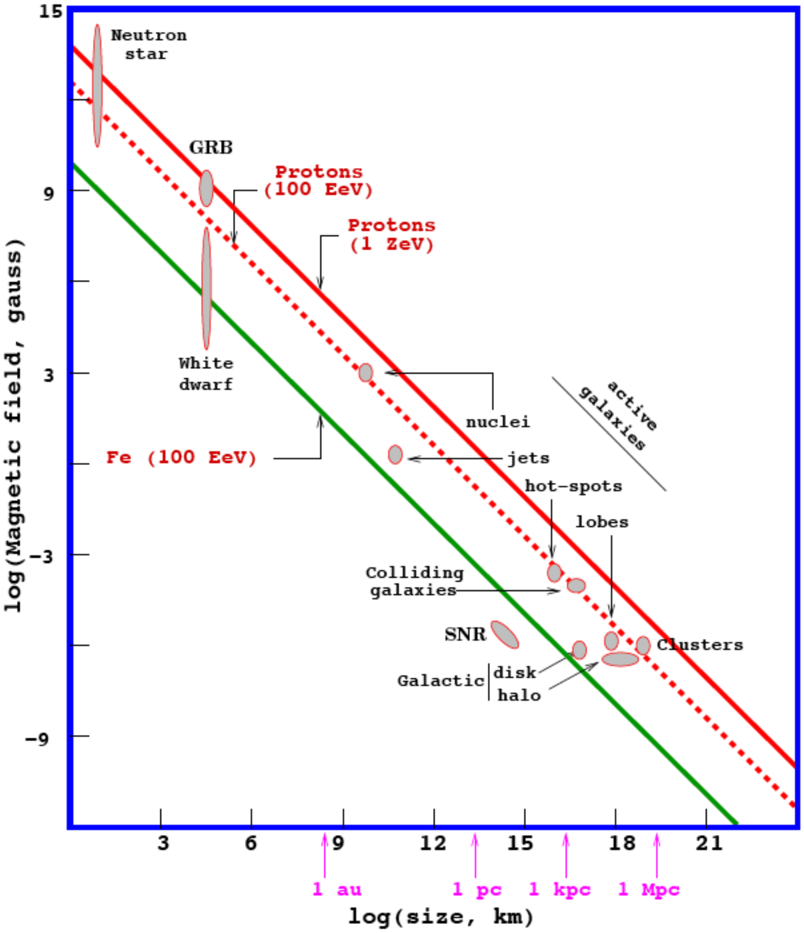

Figure 1.4: An illustration of the magnetic field and source size required to accelerate particles to a maximum energy. Estimates for magnetic field strengths and sizes for several classes of astronomical objects are shown, from [30].

collimated in jets. Several are observed in TeV gamma rays [34].

- **Active Galactic Nuclei (AGN)**: These are similar to microquasars but on a much larger scale. In this case, the central compact object is a supermassive black hole, up to 10^{10} solar masses. AGN are classified based on their appearance to Earth-based telescopes. Examples of the classification criteria are the radio luminosity, the presence of jets, and optical emission lines [35]. Most of these differences are thought to be superficial, only caused by different viewing angles with respect to the rotation axis, as shown in figure 1.5. Many AGN have nonthermal keV x-ray emission from synchrotron radiation of electrons accelerated in the jet. Although TeV photons are often observed from AGN [34], it is unknown whether these are from inverse Compton of the photons on the same electron population (synchrotron self-Compton) or from hadronic processes [36].

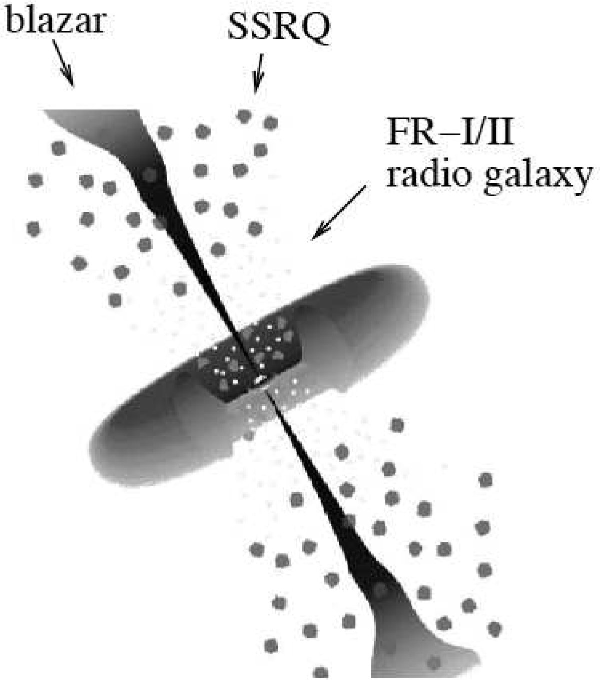

Figure 1.5: Illustration of an AGN with a central black hole, accretion disk, and jets along the rotation axis. The differences in AGN classification are due to the observing angle, with respect to the rotation axis, as well as radio luminosity. Image taken from [35].

- **Gamma Ray Bursts (GRB)**: Gamma ray bursts are the most energetic phenomena in the Universe, outshining all other sources during their brief life. They are bright emitters of keV–MeV photons but only for 10^{-3}–10^{3} s and the emission is highly beamed ($\Gamma = 100$–1000). The progenitors of GRBs are unknown, but could be associated with black hole creation in supernovae and binary system mergers.

1.5 Astrophysical Neutrino Production

Each of the previously mentioned CR sources have the potential of undergoing first order Fermi acceleration. It is likely that the density of matter near the sources is enough to cause many of the CRs to interact near the source instead of escaping. The result of these nucleon-photon or nucleon-nucleon interactions is pions, followed by neutrinos. The dominant channels for nucleon-photon interactions are

$$\begin{aligned} p\gamma \rightarrow & \Delta^{+} \\ & \Delta^{+} \rightarrow p + \pi^{0} \\ & \Delta^{+} \rightarrow n + \pi^{+}, \end{aligned} \tag{1.8}$$

$$\begin{aligned} n\gamma \rightarrow & \Delta^{0} \\ & \Delta^{0} \rightarrow n + \pi^{0} \\ & \Delta^{0} \rightarrow p + \pi^{-}. \end{aligned} \tag{1.9}$$

For nucleon-nucleon interactions, the relevant channels are

$$\begin{aligned} pp \rightarrow & p + p + \pi^0 \\ & p + n + \pi^+, \\ pn \rightarrow & p + n + \pi^0 \\ & p + p + \pi^-. \end{aligned} \tag{1.10}$$

For interactions in astrophysical environments, often the isoscalar assumption is made (equal number of target protons and neutrons). This results in one-half of the pions being neutral and the other half charged. While the neutral pions decay into gamma rays, the charged pions decay to neutrinos, following

$$\pi^0 \rightarrow \gamma\gamma, \tag{1.11}$$

$$\begin{aligned} \pi^+ \rightarrow & \mu^+ + \nu_\mu \\ & \mu^+ \rightarrow e^+ + \nu_e + \bar{\nu}_\mu, \end{aligned} \tag{1.12}$$

$$\begin{aligned} \pi^- \rightarrow & \mu^- + \bar{\nu}_\mu \\ & \mu^- \rightarrow e^- + \bar{\nu}_e + \nu_\mu. \end{aligned} \tag{1.13}$$

Kaons may also be produced in the same interactions and decay similarly. CR interactions with matter and the subsequent decay of charged pions and kaons are the predominant neutrino production mechanism considered throughout the rest of this work, focusing on TeV and above energies.

Counting neutrino (and antineutrino) flavors in the final state results in a flavor ratio at the source of

$$\nu_e : \nu_\mu : \nu_\tau = 1 : 2 : 0. \tag{1.14}$$

After oscillations over a long baseline, the resulting flavor ratio at Earth is [37]

$$\nu_e : \nu_\mu : \nu_\tau = 1 : 1 : 1, \tag{1.15}$$

as discussed in section 2.6. Deviations in the observed flux ratios are potentially interesting, although difficult to measure. Under certain astrophysical scenarios, such as in dense environments, the contribution from muon decay may be suppressed because the mesons or muon have lost energy. This effect leads to an observed flavor ratio of $\nu_e : \nu_\mu : \nu_\tau = 1 : 1.8 : 1.8$ [38]. The contribution of tau neutrinos could also be enhanced by the decay of charmed mesons at very high energy [39].

The important connection between charged CRs and neutrino astronomy is now clear. The acceleration of CRs leads to the production of high energy neutrinos in the presence of target photons or nucleons. Detection of neutrinos would be an unambiguous signature for hadronic CRs, since there is no equivalent leptonic process. The listed candidate CR sources are the same candidate neutrino sources.

1.6 Diffuse Neutrino Astronomy Results

There are a number of standard ways to search for astrophysical neutrinos. This work focuses on searching for point-like sources of neutrinos, or localized excesses over expectations from background, and the latest results will be presented in chapter 9. If there is no single strongest neutrino source but rather a large number of weaker sources, the first detection of neutrinos might be from a diffuse search. In this case, an excess in the total number of neutrinos over the total expectation from atmospheric background simulation would indicate a signal, particularly if the excess events have a harder spectrum.

A number of predictions for diffuse astrophysical neutrinos exist, and these are summarized in [40]. Figure 1.6 shows the results of a diffuse search that was done concurrent to this work, using the 40-string configuration of IceCube. Several model predictions, also shown, are ruled out at greater than 90% CL.

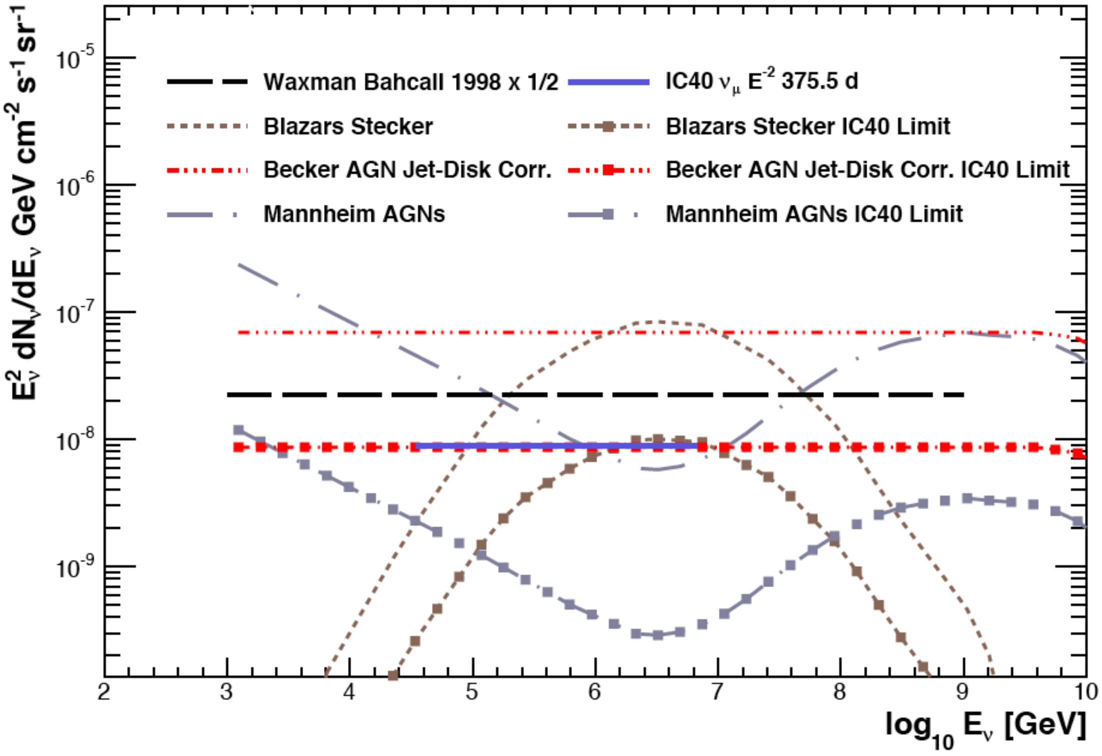

Figure 1.6: The upper limit on an astrophysical muon neutrino flux with an E^{-2} spectrum from [40]. Several theoretical model predictions are also shown, summarized in [40].

w

A number of experiments are capable of measuring a diffuse flux of neutrinos. As of yet, there is no evidence for a diffuse flux of astrophysical neutrinos. The all-flavor 90% upper limits on astrophysical neutrinos for a large number of experiments, including 40-strings of IceCube, are shown in figure 1.7.

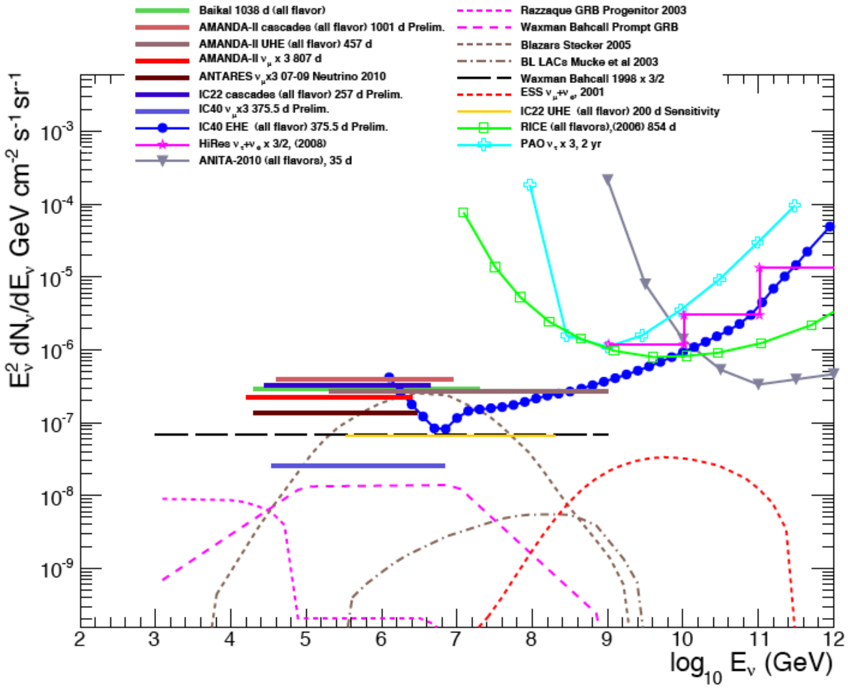

Figure 1.7: Upper limits on an all-flavor astrophysical neutrino flux are shown along with some predictions for diffuse astrophysical neutrinos. The integral upper limits on an astrophysical E^{-2} flux shown are the 5 year AMANDA-II cascade search, [41], the AMANDA-II upper limit on ultra high energy astrophysical neutrinos, [42], the 3-year AMANDA-II ν_μ limit multiplied by 3 [43], the ANTARES 3-year limit on ν_μ multiplied by 3 [44], the IceCube 22-string cascade search [45], the IceCube 22-string ultra high energy sensitivity [46], and based on 40-strings of IceCube [47]. The differential 90% upper limits on an astrophysical neutrino flux have all been normalized to one entry per energy decade. The differential upper limits shown are from the Radio Ice Cherenkov Experiment (RICE) [48], the Pierre Auger Observatory's upper limit on ν_τ multiplied by 3[49], the HiRes experiment [50], the Antarctic Impulsive Transient Antenna (ANITA) [51], and the IceCube 40-string extremely high energy result [52]. Plot taken from [47].

Chapter 2

Principles of Neutrino Detection

This chapter outlines key concepts for understanding how neutrino astronomy is possible. The various interaction modes of the neutrino are described, followed by characteristics of the detectable secondaries. Common backgrounds for neutrino detectors are discussed, followed by the role of the Earth in shielding these backgrounds and serving as a target for neutrino interactions.

The very small interaction probability of neutrinos makes them both a great astrophysical messenger and one that is difficult to detect. Since the neutrino interacts only via the weak force, detection must rely on secondaries produced in neutrino interactions. These secondaries emit electromagnetic radiation that is observable. Very large target volumes are required ($\sim$1 km^3) for the predicted fluxes. The only practical way to construct a neutrino detector of such a size is in a transparent, natural environment, such as the sea, ice sheets, or potentially salt domes.

2.1 Neutrino-nucleon Interactions

Neutrinos only interact via the weak nuclear force. They interact with nucleons by either the charged current (CC) or neutral current (NC) interactions. The CC interaction is mediated by a $W^{\pm}$ boson, while the NC interaction is mediated by the Z^0 boson. These interactions are illustrated with Feynman diagrams in figure 2.1.

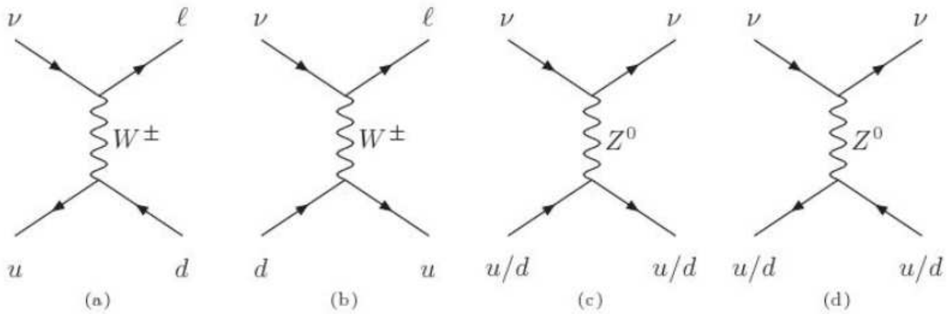

Figure 2.1: Feynman diagrams representing neutrino-quark charged current and neutral current interactions.

The CC interaction [53]

$$\nu_l(\bar{\nu}_l) + N \rightarrow l^{\pm} + X, \tag{2.1}$$

where l is any lepton flavor (e, μ, or τ) and X is the nuclear remnant, has a cross section that is shown in figure 2.2. The NC interaction may be detectable by looking for the shower from the nuclear remnant, but the CC interaction is much more relevant because of the charged lepton in the final state. For this work, we will focus on the muon neutrino CC interactions, since the resulting muon can travel 10s of kilometers, expanding the target volume of the detector many times over the instrumented volume and allowing the possibility to reconstruct the direction well. There is generally no distinction between leptons and anti-leptons in neutrino telescopes. The charge is not observable since the magnetic field of the Earth is too weak to cause any deflection.

The muon moves almost collinear to the direction of the original neutrino at energies of interest, with an average angular deviation of $0.7°/(E/\text{TeV})^{0.7}$ [12].

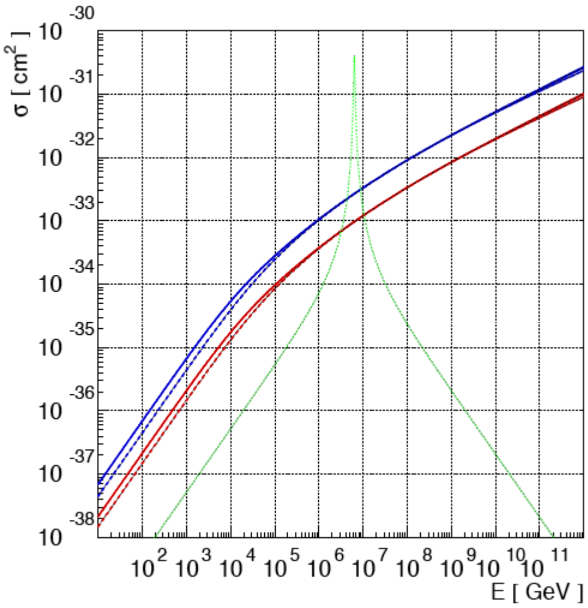

Figure 2.2: Neutrino cross sections for charged current (blue) and neutral current (red). Solid are ν and dashed are $\bar{\nu}$. Image taken from [54]. Included is the Glashow resonance at $E \sim 6.3$ PeV (dotted green) where $\bar{\nu}_e + e^- \rightarrow W^-$.

2.2 Other Neutrino Interactions

Two other neutrino interactions are less relevant for this work, but briefly described here for completeness. The Glashow resonance is an interaction between an antineutrino and electron, where around 6.3 PeV there is a resonant production of the W boson:

$$\bar{\nu}_e + e^- \rightarrow W^-. \tag{2.2}$$

The resulting shower from the W^- decay can be an important contribution for cascade searches. Such resonant production also exists for muon and tau flavors, but these are unstable particles and do not represent a practical means for detecting neutrinos. The cross-section for this process is also shown in fig 2.2.

It is possible for neutrinos and antineutrinos to annihilate with a resonant production of the Z boson. This interaction is of interest for extremely high energy neutrinos (above 10^{21} eV), which may be attenuated as they interact with relic neutrinos from standard big bang cosmology [55]. The decay products from the "Z-burst" could show up at earth as UHECRs above the GZK cutoff [56]. At present, it seems the fluxes are so small that this does not represent a viable way to detect either extremely high energy or low energy relic neutrinos.

2.3 Charged Lepton Propagation

The ability of a neutrino detector to distinguish between the three neutrino flavors relies on the possibility of distinguishing the varied energy deposition patterns from the resulting charged leptons. These will radiate energy from continuous ionization loses as well as stochastic processes: bremsstralung, e^+e^- pair production, photonuclear interactions, and finally decay.

2.3.1 Electrons

Electron energy loss is dominated by catastrophic bremsstralung energy losses above about 1 GeV [54]. The electron loses about 20% of its energy per 0.01 meter water equivalent (mwe). The distance that it remains detectable is generally small compared to the segmentation of neutrino detectors, so the emission is considered almost point-like. The direction cannot be reconstructed well, but since the interaction needs to occur within or very near the detection volume, the energy estimation is relatively good.

2.3.2 Muons

Muons, due to their higher mass, do not suffer such extreme energy losses as electrons. Muons travel significantly farther, emitting radiation along a track as they move. The energy losses for muons are summarized in figure 2.3. Below about 1 TeV, continuous energy losses from ionization dominate. Above that energy, stochastic processes dominate. The total energy loss per distance traveled can be approximated as

$$\frac{dE}{dx} \approx a + bE, \tag{2.3}$$

where a and b are roughly constant. Their values are approximately

$$\begin{aligned} a &= 0.26 \text{ GeV/mwe}, \\ b &= 3.57 \times 10^{-4} \text{ /mwe}. \end{aligned} \tag{2.4}$$

The value for a can be calculated using the Bethe-Block formula accounting for the relativistic case [57], which reduces the energy loss somewhat compared to the non-relativistic case [58].

The approximate expression in eq. 2.3 can be integrated to get an estimate of the average moun range R:

$$R = \frac{1}{b}\ln(1 + \frac{bE_0}{a}). \tag{2.5}$$

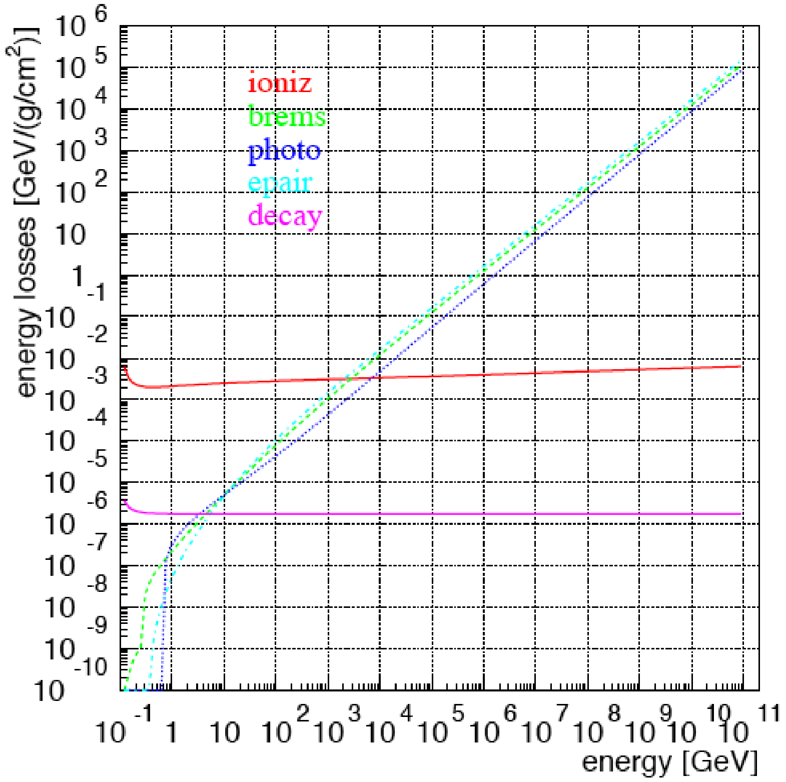

Figure 2.3: Ionization, bremsstrahlung, photonuclear, electron pair production and decay (multiplication of the probability of decay by the energy) losses for a muon in ice.

For example, a 1 TeV (100 TeV) muon will travel approximately 2.2 km (12.6 km) in ice.

2.3.3 Tau Particles

A tau lepton will only move a short distance due to its very short lifetime, $\sim 3 \times 10^{-13}$ s. Because of the high mass of the tau, it is essentially a minimum ionizing particle up to 50 PeV. The tau decays produce cascades via hadronic and electron decay modes, looking similar to an electron in ice. The short track ($\sim$ 100 m at a few PeV) connecting the initial neutrino interaction and the tau decay can be a unique “double bang” signature for these events. Important for any analysis in the muon channel, the tau decays to a muon with a 17.7% branching ratio [3]. Also note that the tau may decay back into a tau neutrino before losing much energy. This regeneration effect keeps the flux of tau neutrinos high even when they might interact at high energies in a target such as the Earth.

2.3.4 Čerenkov Radiation

The energy losses suffered by relativistic muons appear as electromagnetic Čerenkov radiation. When the muon is moving faster than the speed of light in the medium, the radiation forms a coherent wavefront at a specific emission angle [59, 60], illustrated in figure 2.4. The Čerenkov angle θ_c depends on the speed of the particle and the index of refraction of the ice:

$$\cos\theta_c = \frac{1}{\beta n(\lambda)}. \tag{2.6}$$

Relevant to this work, all particles can be assumed to have $\beta = v/c \approx 1$ and a constant index of refraction of the ice $n_{\text{ice}} = 1.32$, giving $\theta_c \approx 41°$. A full treatment considers the difference between the group and phase indices of refraction in a medium, but these have been shown to yield negligible changes for neutrino astronomy [61].

The number of Čerenkov photons per unit length and wavelength is given by the Frank-Tamm formula [62]:

$$\frac{d^2N}{dxd\lambda} = \frac{2\pi\alpha z^2}{\lambda^2}\sin^2(\theta_c(\lambda)), \tag{2.7}$$

where α is the fine-structure constant. The radiation goes as $1/\lambda^2$ and is dominated

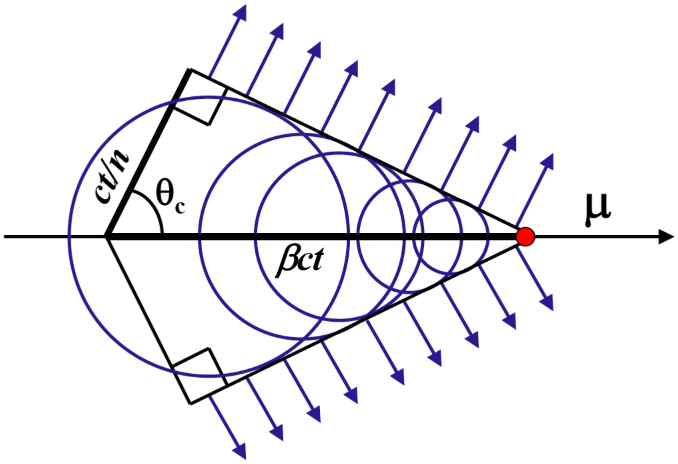

Figure 2.4: Illustration of Čerenkov conical emission from a muon traveling through the ice. The circles represent isotropic emission, which constructively interferes only on the Čerenkov cone.

by shorter wavelengths. Integrating eq. 2.7 from 365 nm to 600 nm gives about 210 photons per centimeter. The low and high wavelength cutoffs of the waveband relevant for IceCube are due to the glass and ice transparency, respectively.

2.4 Cosmic Ray Backgrounds

In order to make neutrino astronomy a reality, we need to understand and cope with the backgrounds that exist. The main backgrounds that can mimic an astrophysical signal originate from CR interactions in Earth's atmosphere. High energy CRs bombard the atmosphere, creating extensive air showers of electrons, positrons, pions, kaons, muons, and neutrinos. These interactions, illustrated in figure 2.5, are analogous to the production of neutrinos in astrophysical sources shown in eqs. 1.10–1.13. The muons from CR showers are the background for neutrino astronomy, and the flux of CR muons versus depth is shown in figure 2.6.

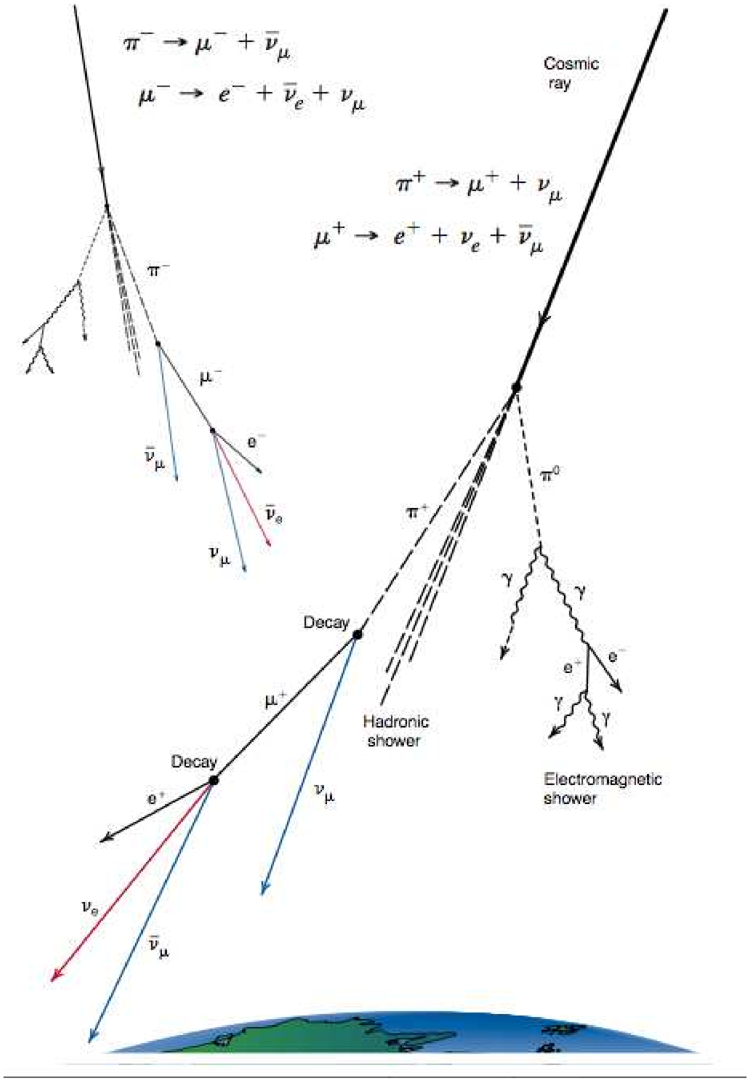

Figure 2.5: Illustration of particle production channels in extensive air showers induced by high energy cosmic rays. The muons and neutrinos produced represent the primary backgrounds in a search for extraterrestrial neutrinos.

The largest difference is that the atmosphere is generally denser than astrophysical environments where shock acceleration takes place. Because of this increased density, the kinematics of interaction and decay play an important role in the flux of

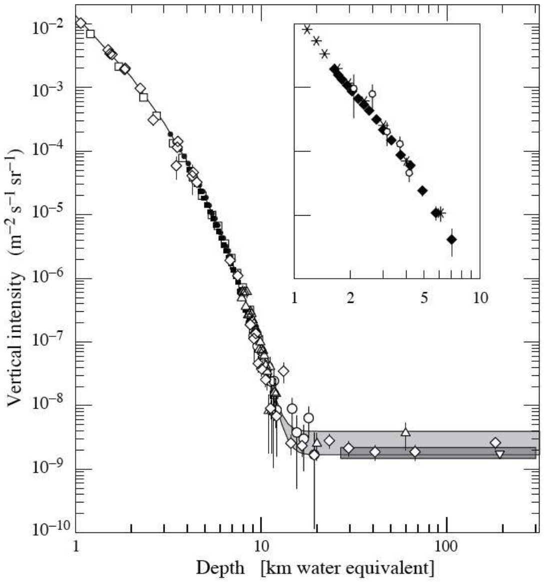

Figure 2.6: Vertical muon intensity versus depth, from [3]. Muons originating from atmospheric neutrinos begin to dominate after about 20 km (water equivalent).

muons and neutrinos from these showers. The role of energy loss can be approximated analytically by defining the critical energy E_{crit} as the energy where a particle has an equal interaction and decay length. In [63], it is defined as

$$E_{\text{crit}} = \frac{mc^2 h_0}{c\tau}. \tag{2.8}$$

Here, τ is the lifetime of the particle and $h_0 = 6.4$ km is the characteristic height of the atmosphere, assumed to be isothermal ($\rho = \rho_0 e^{-h/h_0}$). A summary of the critical energy for particles important to the production of atmospheric neutrinos and muons is given in Table 2.1.

For energies below E_{crit}, the particle most likely decays without losing any energy,

Table 2.1. Critical energy for particles important to atmospheric neutrino and muon production, from [3].

Particle	Constituents	mc^2 (GeV)	$E_{\rm crit}$ (GeV)
$\mu^\pm$	lepton	0.106	1.0
π^+, π^-	$u\bar{d}$, $\bar{u}d$	0.140	115
K^+, K^-	$u\bar{s}$, $\bar{u}s$	1.116	850
D^+, D^-	$c\bar{d}$, $\bar{c}d$	1.87	3.8×10^7
$D^0, \bar{D}^0$	$c\bar{u}$, $\bar{c}u$	1.865	9.6×10^7
D_s^+, D_s^-	$c\bar{s}$, $\bar{c}s$	1.969	8.5×10^7
Λ_c^+	udc	2.285	2.4×10^8

and the spectrum of the decay products follows the primary CR spectrum. For energies higher than $E_{\rm crit}$, the particle most likely interacts, losing energy before it decays. In this case, the spectrum of the secondaries is reduced by one power of the energy. The particles of interest in an experiment like IceCube have energy greater than 1 TeV. So, although the expected CR spectrum at the source is $d\Phi/dE \propto E^{-2}$ from Fermi acceleration, and after propagation to Earth we observe $\sim E^{-2.7}$, the conventional atmospheric muon and neutrino fluxes (from pion and kaon decay) follow a spectrum $\sim E^{-3.7}$. Although they are produced much less frequently and are yet to be measured, the prompt atmospheric fluxes (from the decay of charmed mesons) mostly follow the CR spectrum.

2.5 The Earth as a Neutrino Target

The Earth can be used to block much of the CR air shower-induced background discussed in the previous section. The muon range in ice was calculated from eq. 2.5 to typically be 2–10 km (water equivalent). Therefore, a detector buried deep under-ground still detects many CR-induced muons, created in the atmosphere and moving down-ward through the detector. Defining straight down-going as $\theta = 0$, the muon flux is greatly attenuated as θ increases and the muons must pass through more and more overburden. Near the horizon ($\theta = 90°$), the down-going muon flux becomes completely attenuated, and the only muons observed are induced instead from neutrinos. Neutrinos are the only particles we know about that can pass through the entire Earth and interact near our detector to create an up-ward traveling muon. The rate of down-going muons is about 10^6 times higher than the up-going atmospheric neutrino rate. Using the Earth as a shield for atmospheric muons means that neutrino astronomy is primarily sensitive to the up-going region where the background is least. However, neutrino astronomy in the down-going region is still possible but only with a limited sensitivity. The approach used in this work is to cut away low energy events and only keep very high energy events where a harder signal might peak out above the background.

Attenuation of neutrinos in the Earth is not completely negligible. The absorption probability for neutrinos as a function of incidence angle is shown in figure 2.7. The column depth of the entire diameter of the Earth is sufficient to appreciably attenuate $\gtrsim 100$ TeV neutrinos. Since the cross section is proportional to the energy, even higher energy neutrinos can become completely masked by the Earth. However, near the horizon, the column depth is small enough that $\sim$ EeV neutrinos can penetrate to the sensitive detection volume (which increases with the muon range). For more and more vertically down-going neutrinos, the target material decreases and the CR muon background increases. Note that taus have a regeneration effect that keeps them from being lost due to absorption.

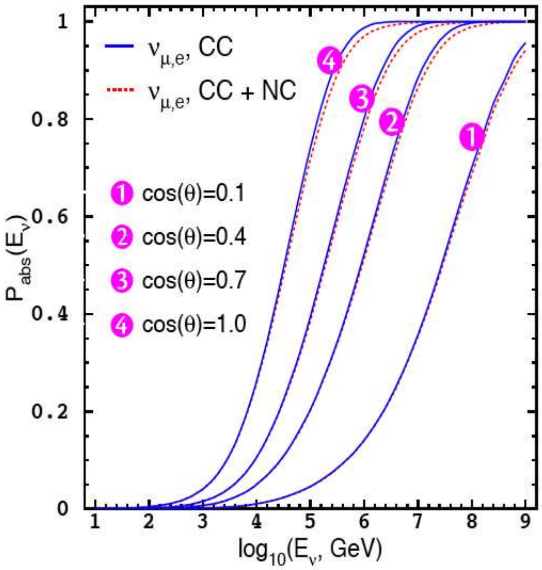

Figure 2.7: Neutrino absorption probability in the Earth for four nadir angles ($\cos\theta = 0.1, 0.4, 0.7, 1.0$). The dashed lines take NC interactions into account and the solid lines do not. Taken from [64].

2.6 Neutrino Oscillations

In the standard model, it is possible for neutrinos to change flavor. This has been convincingly observed experimentally for solar neutrinos, atmospheric neutrinos, and possibly for accelerator neutrinos. Flavor oscillations are a result of the mismatch between the neutrino flavor and mass eigenstates. We can calculate the oscillation probability by following [3].

The relationship between the flavor and mass eigenstates is

$$|\nu_\alpha\rangle = \sum_i U^*_{\alpha i}|\nu_i\rangle, \tag{2.9}$$

where $|\nu_\alpha\rangle$ is a definite flavor state, $\alpha = e$ (electron), μ (muon), or τ (tau), and

$$|\nu_i\rangle = \sum_\alpha U_{i\alpha}|\nu_\alpha\rangle, \tag{2.10}$$

where $|\nu_i\rangle$ is a definite mass state, $i = 1, 2, 3$, and $U_{\alpha i}$ are elements of the Maki-Nakagawa-Sakata (MNS) matrix. The MNS matrix is analogous to the CKM matrix for quark mixing and is given by

$$U = \begin{pmatrix} c_{12}c_{13} & s_{12}c_{13} & s_{13}e^{-i\delta} \\ -s_{12}c_{23} - c_{12}s_{23}s_{13}e^{i\delta} & c_{12}c_{23} - s_{12}s_{23}s_{13}e^{i\delta} & s_{23}c_{13} \\ s_{12}s_{23} - c_{12}c_{23}s_{13}e^{i\delta} & -c_{12}s_{23} - s_{12}c_{23}s_{13}e^{i\delta} & c_{23}c_{13} \end{pmatrix} \begin{pmatrix} e^{i\alpha_1/2} & 0 & 0 \\ 0 & e^{i\alpha_2/2} & 0 \\ 0 & 0 & 1 \end{pmatrix}, \tag{2.11}$$

where $c_{ij} = \cos\theta_{ij}$ and $s_{ij} = \sin\theta_{ij}$. The phase δ is non-zero if the neutrinos violate CP symmetry. The other phases α_1 and α_2 are only non-zero if the neutrino and antineutrino are identical, a Majorana particle.

The neutrino "born" in a certain flavor state propagates in its mass eigenstates. Applying Schrödinger's equation to the ν_i component of ν_α, we can write the state after propagating some distance L as a plane wave in the ultra-relativistic approximation:

$$|\nu_i(L)\rangle = e^{-im_i^2 L/2E}|\nu_i(0)\rangle. \tag{2.12}$$

Because the neutrinos have different masses, the eigenstates propagate at different speeds. As the mass eigenstates are a superposition of the flavor eigenstates, this causes interference between the flavor states, and we can rewrite eq. 2.9 as

$$|\nu_\alpha(L)\rangle = \sum_i U^*_{\alpha i} e^{-im_i^2 L/2E} |\nu_i(0)\rangle. \tag{2.13}$$

We can write the probability of a neutrino of flavor α to oscillate to flavor β as

$$\begin{aligned} P_{\alpha\rightarrow\beta} &= |\langle\nu_\beta|\nu_\alpha\rangle|^2 \\ &= \left|\sum_i U^*_{\alpha i} U_{\beta i} e^{-im_i^2 L/2E}\right|^2 \\ &= \delta_{\alpha\beta} - 4\sum_{i>j} Re(U^*_{\alpha i}U_{\beta i}U_{\alpha j}U^*_{\beta j}) \sin^2(\frac{\Delta m^2_{ij}L}{4E}) + 2\sum_{i>j} Im(U^*_{\alpha i}U_{\beta i}U_{\alpha j}U^*_{\beta j}) \sin(\frac{\Delta m^2_{ij}L}{2E}), \end{aligned} \tag{2.14}$$

where $\Delta m^2_{ij} = m_i^2 - m_j^2$ and δ is the Kronecker delta symbol. The magnitude of the oscillations is calculated from elements of the MNS matrix, and the frequency of the oscillations is given by (restoring previously omitted factors of $\hbar$ and c to go from natural to metric units)

$$\frac{\Delta m^2_{ij}L}{4E} \approx 1.27\Delta m^2_{ij}(\mathrm{eV}^2)\frac{L(\mathrm{km})}{E(\mathrm{GeV})}. \tag{2.15}$$

Cosmological baselines ensure that the neutrino oscillations occur, even at the highest energies available. The result is that an initial flux flavor ratio at the source of $\nu_e : \nu_\mu : \nu_\tau = 1:2:0 \rightarrow 1:1:1$ [37]. As previously mentioned, in certain astrophysical scenarios the contribution from muon decay may be suppressed because the mesons or muon have lost energy before decaying. This effect leads to an observed flavor ratio of $\nu_e : \nu_\mu : \nu_\tau = 1 : 1.8 : 1.8$ [38]. The contribution of tau neutrinos could also be enhanced by the decay of charmed mesons at very high energy [39].

Chapter 3

The IceCube Neutrino Observatory

This chapter describes the design and operation of the IceCube Neutrino Observatory. Optical properties of the South Pole ice and background levels are measured in situ. The digital optical module (DOM) is the fundamental detection element of IceCube. A DOM consists of a photomultiplier tube (PMT) and electronics for readout, digitization, and communications. A trigger condition is used to control data rates.

The IceCube Neutrino Observatory is composed of a deep array of 86 strings holding 5,160 digital optical modules deployed between 1.45 and 2.45 km below the surface of the South Pole ice. It is the world's largest neutrino telescope, encompassing ~ 1 km^3 of ice. The layout of IceCube is shown in figure 3.1. The strings are typically separated by about 125 m with DOMs separated vertically by about 17 m along each string. IceCube construction started with the first string installed in the 2005–2006 austral summer [65] and was completed in December of 2010.

Six of the strings in the final detector will use high quantum efficiency DOMs and a spacing of about 70 m horizontally and 7 m vertically. Two more strings will have standard IceCube DOMs and 7 m vertical spacing but an even smaller horizontal spacing of 42 m. These eight strings along with seven neighboring standard strings make up DeepCore, designed to enhance the physics performance of IceCube below 1 TeV. The physics goals of DeepCore include opening the southern hemisphere to neutrino astronomy at lower energies, searching for dark matter, and studying atmospheric neutrino oscillations [66].

The observatory also includes a surface array, IceTop, for extensive air shower measurements on the composition and spectrum of CRs [67]. IceTop consists of 160 tanks, two placed near the top of each string. This configuration allows for CR muons reaching the in-ice detector to be vetoed if they leave a detectable signal in IceTop. This benefit is limited to a very small fraction of the sky.

At present, all 86 strings of IceCube are ready for data taking. This work is done almost entirely using data taken with forty strings of IceCube, in operation under this configuration from 2008 April 5 to 2009 May 20. The layout of these strings in relation to the final 86-string IceCube configuration is shown in figure 3.2. Over the entire period the detector ran with an uptime of 92%, yielding 375.5 days of total exposure. Down time is mainly due to test runs during and after the construction season dedicated to calibrating the additional strings and upgrading data acquisition systems. Some of this lost time could be recoverable in the case of an exceptional astronomical event, and uptime will continue to increase as detector operations stabilize.

3.1 Digital Optical Modules

The fundamental detection element of the IceCube Neutrino Observatory is the DOM (digital optical module). A DOM contains a 25 cm diameter Hamamatsu R7081-02 PMT [68, 69] to detect blue and near-ultraviolet Čerenkov radiation produced by the charged leptons passing through the ice. The PMT dark rate at $-40°$ C is 500 Hz.

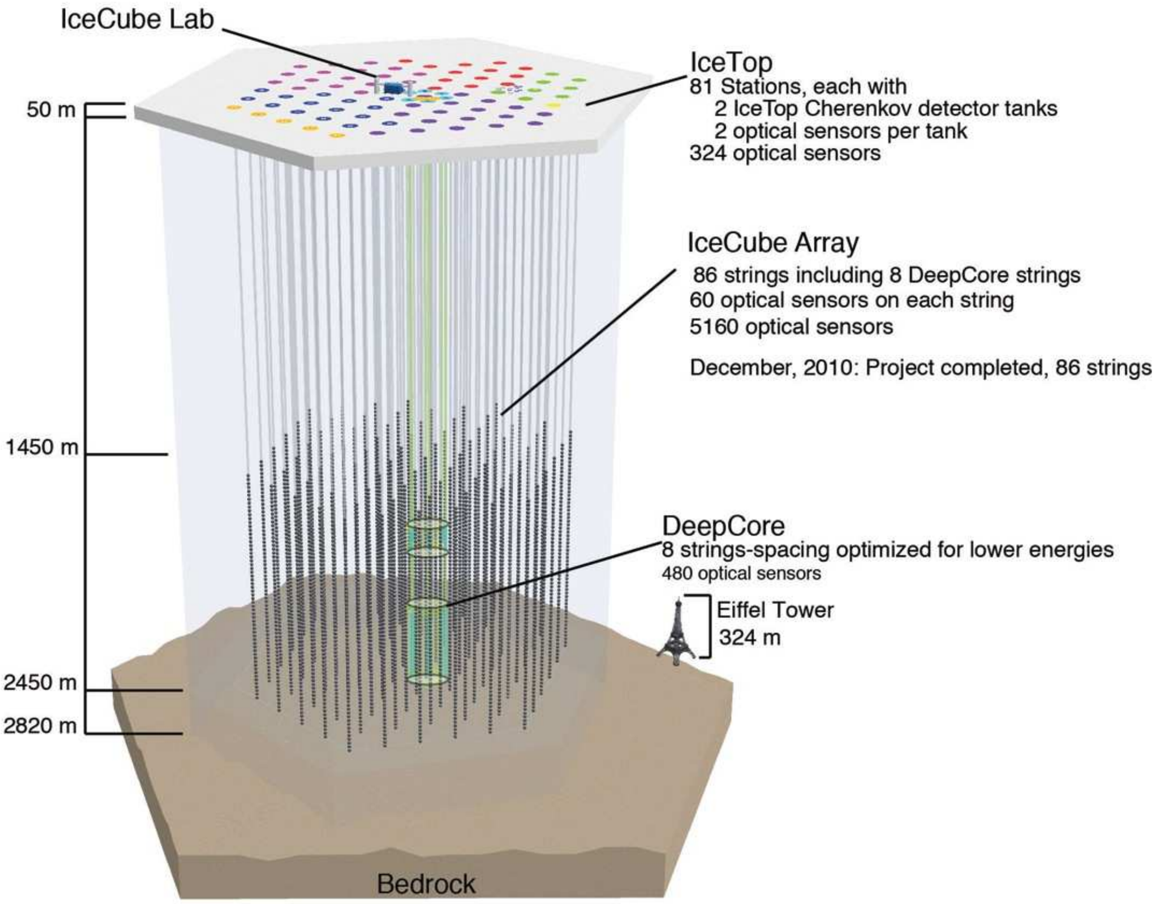

Figure 3.1: Schematic view of the IceCube Neutrino Observatory at the geographic South Pole.

The signal transit time spread is $3.2\,\mu$s. A modular 2 kV high voltage power supply provides between 1200 V and 1400 V to run the PMT at a gain of approximately 10^7. A main board is responsible for processing the analog output of the PMT.

The 13 mm thick glass sphere is able to withstand the immense pressure (up to 70 MPa) exerted during the deployment. There is a gel between the glass and the

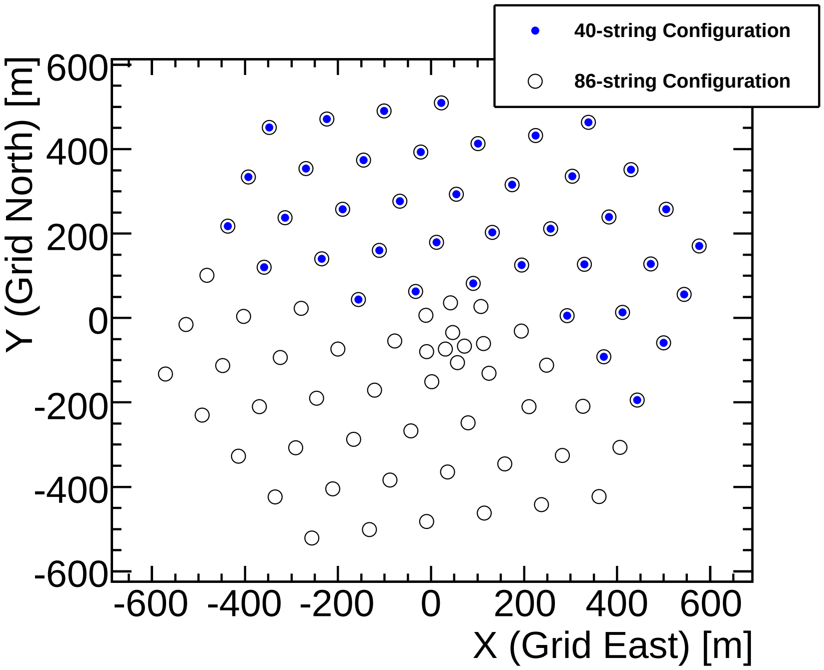

Figure 3.2: Overhead view of the 40-string configuration, along with additional strings that will make up the complete IceCube detector.

PMT to provide support and optical coupling. The resulting short wavelength cutoff of the glass and gel is at ∼350 nm. This matches the spectral response of the PMT well (300–650 nm [69]). The peak quantum efficiency of the PMT is about 25% at 390 nm.

The DOM includes a flasher board, containing twelve light emitting diodes (LEDs). Half of the LEDs point radially out in the horizontal direction, and half point upward at a 48° angle. The flashers provide a way to perform in situ calibrations, such as timing, geometry, energy, and measurements of the optical properties of the ice.

Lastly, the DOM includes a mu-metal cage to shield the Earth's magnetic field so electrons created by a photon in the photocathode travel directly to the anode. All components of a DOM are shown in figure 3.3 [70].

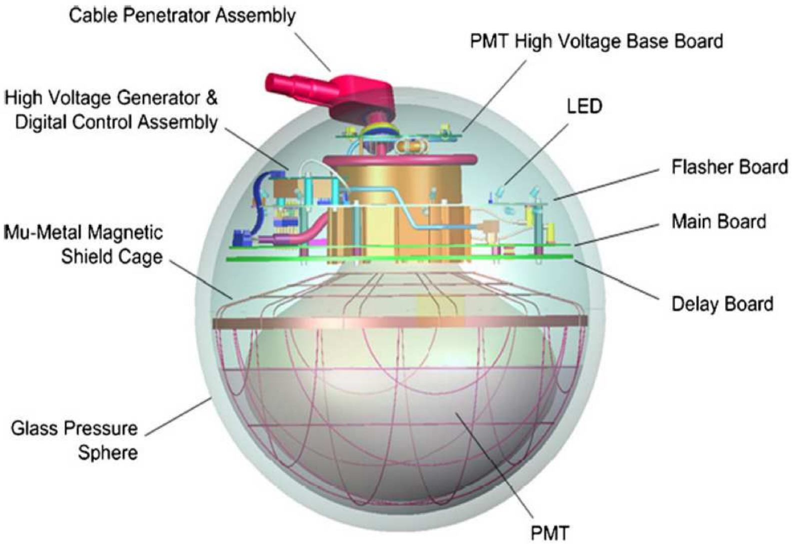

Figure 3.3: Schematic view of the Digital Optical Module (DOM), the fundamental detection element of IceCube, from [68].

3.2 Data Acquisition

IceCube is designed for a broad range of science goals over a wide energy range. The primary goal of the IceCube Data Acquisition (DAQ) is to capture and timestamp the complex and widely varying optical signals with the maximum possible dynamic range. Events within the detector may last mere microseconds or 100s of microseconds, as in the case of slow magnetic monopoles. The location of the DOMs buried in the ice at the South Pole, distributed over a network that spans several kilometers means that reliability and programmability were compulsive in the design.

A single Čerenkov photon arriving at a DOM can produce a photoelectron, which is called a hit if the analog output of the PMT exceeds a threshold equivalent to ~ 0.25 of the average single photoelectron charge. The waveform of the PMT total charge is digitized and sent to the surface if hits are in coincidence with at least one other hit in the nearest or next-to-nearest neighboring DOMs within ±1000 ns. Hits that satisfy this condition are called local coincidence hits.

The signal ranges from one to many thousands photons in each DOM with potentially interesting features on time scales from a few nanoseconds up to several microseconds. Because of this, the digitization of the analog PMT output is accomplished in two distinct ways.

- **Analog Transient Waveform Digitizer (ATWD)**: The ATWD chip samples at 300 MHz (configurable). It has an analog memory that stores 128 samples in a capacitor array. This gives a time resolution (bin size) of 3.3 ns for the first 427 ns of the waveform. The ATWD is normally quiescent, requiring little power, and needs to be triggered by a PMT discriminator. The signal fed into the ATWD first passes through a ~ 70 ns delay line to allow digitization of the front of the waveform.

  Three digitizers operate in parallel in the ATWD, fed through amplifiers of gains $\times 16$, $\times 2$, $\times 0.25$. The highest gain channel gives the best charge resolution, but if near saturation (after 1022 counts) digitization of the next gain channel is triggered. The lowest gain channel saturates only after the PMT ($\sim 31\,$photoelectrons/ns), meaning the full dynamic range of the PMT is able to be digitized.

  After triggering a readout, the ATWD takes $29\,\mu$s to completely digitize and reset. Two ATWD are on each DOM to minimize the impact of this dead time.

- **Fast Analog to Digital Converter (fADC)**: There is an additional PMT signal path since some physics signals last longer than the 427 ns window of the ATWD. A high-speed analog to digital converter continuously samples the PMT output at 40 MHz, giving the coarser bin size of 25 ns. The length of the raw fADC record is chosen to be 6.4 μs. There is a dead time of two clock cycles in between readouts.

The DOM main boards also contain field-programmable gate arrays, which handle the data transport after digitization.

Since the waveforms can contain multiple hits, the total number of photoelectrons and their arrival times are extracted with an iterative Bayesian-based unfolding algorithm. This algorithm uses the template shape representing an average hit.

All 60 DOMs per string run power and communications through a single 3 cm diameter cable of twisted-wire pairs. Two DOMs share a wire-pair to limit the size of the cable. The cable runs to a surface junction box near the top of each hole and finally connects to a central counting house in the IceCube Lab. A custom computer called the DOMHub handles all communication from DOM main boards on one string. Eight DOM Readout cards on each DOMHub are each capable of hosting 8 DOMs.

IceCube uses a simple multiplicity trigger, requiring local coincidence hits in eight DOMs within $5\,\mu$s. Once the trigger condition is met, local coincidence hits within a readout window $\pm10\,\mu$s are recorded, and overlapping readout windows are merged together. IceCube triggers primarily on down-going muons at a rate of about 950 Hz in this (40-string) configuration. Variations in the trigger rate by about ±10%

are due to seasonal changes affecting development of CR showers and muon production in the atmosphere. Higher rates occur during the austral summer when the atmosphere is hotter, less dense, and mesons lose less energy before decaying [71].

3.3 Calibration

Each DOM has an independent 20 MHz crystal oscillator with a certified stability of $\sim 10^{-11}$ over 5 seconds. This local clock is used to timestamp hits. In order to keep all of these clocks synchronized, a procedure known as reciprocal active pulsing calibration (RAPcal) is performed. A precisely timed pulse is sent from a central GPS clock to each DOM. The transition edge of this clock is known to better than 100 ps. The DOM receives this RAPcal signal and records the arrival time according to its local clock. The DOM generates a nearly-identical response and transmits to the surface. There is a reciprocal symmetry between the oppositely-traveling signals that ensures an equal transit time, down to small variations in electronic components. By accounting for transit times and the RAPcal timestamp from the DOM, a single GPS clock is used to transform the hit times to a global time.

The gain calibration is an automated process that happens approximately once a month. This ensures that all DOMs are operating at the proper voltage to achieve a gain of 10^7. Before the waveforms can be unfolded to extract a series of the most likely photon arrival times, a series of calibrations are applied. There can be a DC offset in the waveforms, and this baseline needs to be subtracted. The ATWDs also have a consistent pedestal pattern, non-zero even when no signal is present. This pattern is subtracted off. There is a correction for droop in the waveforms, due to the transformer connecting the PMT to the main board.

3.4 Installation

In order to deploy the DOMs, holes need to be drilled 2.5 km into the Antarctic ice sheet. The first ∼ 50 m of the hole are drilled using a copper heating element, circulating water at ∼ 90° C in a closed loop. This first layer is called the firn and is not ice but compacted snow. Once the ice underneath is reached, a faster drilling process commences, using an open loop hot water drill pulled straight down by gravity. A standing column of melted water remains in the hole. The DOMs are lowered into the holes generally within 6–8 hours after completion of drilling. The hole refreezes from top-down, due to temperature gradients in the ice. The refreezing process takes about 2 weeks. Once the holes are refrozen, the DOMs are permanently inaccessible, making the quality assurance testing before deployment critical. About 2% of the DOMs fail to power up or communicate after the ice refreezes, and these are removed from data acquisition.

3.5 Optical Properties of South Pole Ice

The IceCube Neutrino Observatory is only able to function as a telescope by understanding the behavior of Čerenkov photons emitted by the charged leptons. The ice under the South Pole is up to 2820 m thick and has formed over the past 165000 years. The formation is driven by precipitation with varying amounts of particulate impurities present, including volcanic ash. As a result, the optical properties vary by over an order of magnitude as a function of depth [72].

The optical properties of ice are completely specified by the absorption length

λ_a, scattering length λ_s, and angular scattering function. The scattering function describes the angular distribution of the photon scattering. In Mie scattering [57], the photon wavelength is comparable to the size of a dielectric sphere (particular impurity in ice) and the scattering is highly peaked in the forward direction, $\langle \cos\theta \rangle = 0.94$. The effective scattering length λ_e, defined as

$$\lambda_e = \frac{\lambda_s}{1 - \langle \cos\theta \rangle}, \tag{3.1}$$

is the distance it takes to randomize the original direction of the photon. For the peak Čerenkov wavelength at 400 nm and in the depth range of IceCube, the ice has an average effective scattering length around 20 m but a long absorption length, around 110 m. By contrast, Mediterranean sea water at the site of ANTARES has been measured to have an effective scattering length of 265 m but a shorter absorption length of just 60 m [73]. Shallower than 1400 m, scattering from bubbles within the ice becomes so significant that this region can not be used for Čerenkov detection. Deeper than 1400 m, time and pressure have transformed these bubbles into air hydrate crystals with a index of refraction that matches the ice [74]. This makes the ice far more transparent with varying dust concentrations as the dominant concern.

The in situ measurement of the ice properties using a variety of deployed light sources led to the AHA ice model [72]. The depth range was originally applicable only to the AMANDA depth range and has been extrapolated below 2050 m using ice core measurements. This method seemed to underestimate the clarity of the deep ice, and new direct measurements have been the focus of a renewed effort [75].

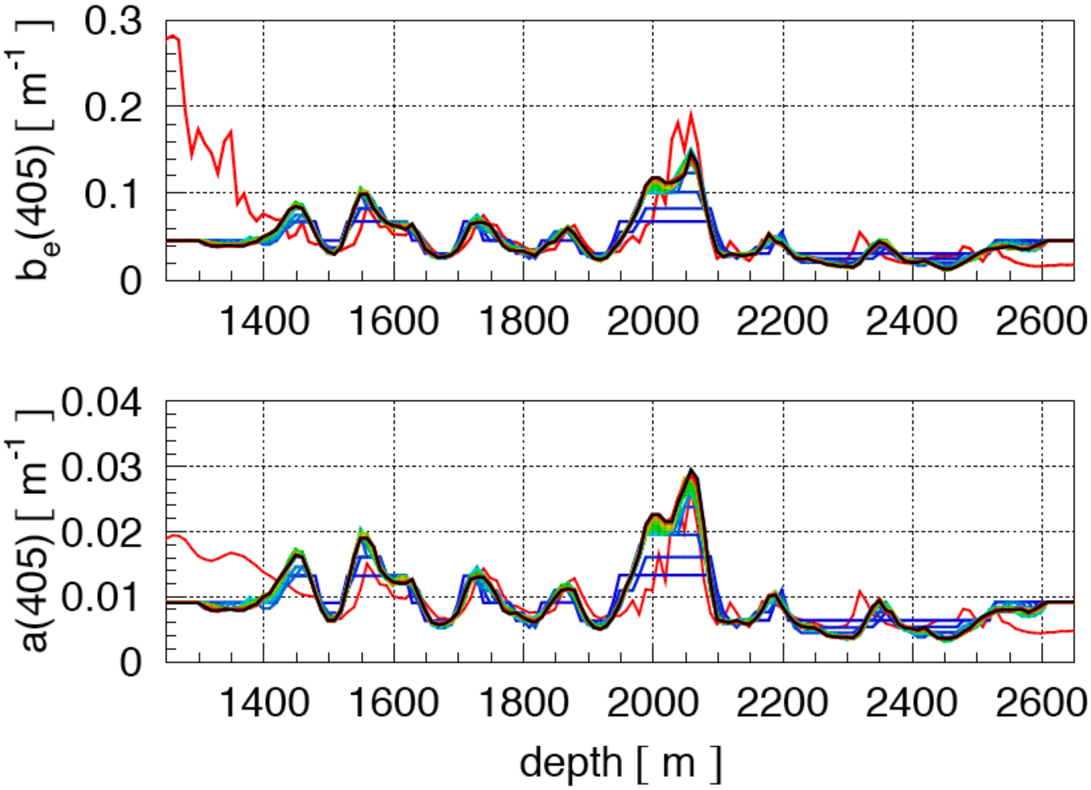

Figure 3.4: Scattering (top) and absorption (bottom) coefficients ($1/\lambda$) as a function of depth for the AHA and South Pole Ice (SPICE) models, from [75]. The AHA model used in this work is in red. The SPICE model is in black, with the global fitting iterations in blue and error range of the fit in green.

3.5.1 Hole Ice

The process of water refreezing within the holes after deployment is a significantly different process than that forming the undisturbed glacial ice. The freezing likely forces air out of the water, leaving bubbles that increase the amount of scattering. Recent observations with a video camera deployed deep in the hole show evidence that as the hole refreezes from the outside inward, bubbles and impurities are forced into the very center. This forms a narrow column of impure ice, 5–10 cm wide. The effective scattering length is hard to measure independently, but could be as low at 50 cm. This extra scattering can be considered to smooth out the angular response of the DOMs.

3.6 Other Neutrino Telescopes

3.6.1 AMANDA

The Antarctic Muon and Neutrino Detector Array (AMANDA) was the largest Čerenkov detector of its time, paving the way for the construction of IceCube. Here we highlight some of the differences with respect to IceCube.

AMANDA was an array of 677 optical modules arranged on 19 vertical strings. The diameter of the detector was 200 m, and, with a few exceptions, the modules were deployed between depths of 1500 m to 2000 m. The first ten strings were deployed by 1997 and the last nine added by early 2000.

The optical modules had PMTs with a diameter of 8 inches, run at a gain of about 10^9. Most strings use analog transmission over coax, twisted pair, and analog-optical channels. One string was designed to support digital communication as a prototype for IceCube. During most of its lifetime, AMANDA ran a 24-fold multiplicity trigger, collecting times of hits, time the PMT waveform spends over some threshold, and the height of the waveform peak.

AMANDA ran independently from 2000 to 2006 before undergoing an upgrade to the data acquisition system and becoming a subsystem of the IceCube detector. AMANDA was decommissioned in December 2009. During its lifetime, it was used set the best limits on astrophysical neutrinos above ~ 1 TeV. It proved that the technique of deploying sensors into the ice to build a Čerenkov telescope was not only possible but one of the most practical ways to build such a detector.

3.6.2 Deep Sea Telescopes

The first attempts to build a ~ 1 km^3 Čerenkov detector were in the deep sea around 1980. Unfortunately, the Deep Underwater Muon and Neutrino Detector (DUMAND) failed after a 15-year long effort off the main island of Hawaii. Even so, DUMAND laid the groundwork for later underwater efforts. The technical challenges are daunting, but many of the detector technologies finally succeeded with the construction of the smaller Lake Baikal telescope.

Current efforts are targeted in the Mediterranean Sea. The NEMO collaboration has realized installation at 2000 m deep and 100 km from the Sicilian coast. They are currently testing down to 3500 m [76]. The concept is to install flexible towers, each 750 m high with 16 floors separated by 40 m. Each floor has a pair of optical modules, one looking downward and the other outward, at the end of each arm.

The NESTOR project is located 15 km from the Greek coast at a depth of 4100 m. NESTOR attempts to make all connections on a floating platform on the surface of the sea, whereas the others use submarines to make the final connections. NESTOR deployed a prototype rigid "tower" (32 m diameter, 12 stories with 30 m spacing, and 144 PMTs) in 2003, but an underwater cable problem prevented operation after just one month.

The ANTARES detector comprises a total of 900 optical modules over 12 flexible lines, fully deployed with some of the test hardware lasting since 2002. The first two full-size lines were connected in 2006. Each line is about 350 m long, reaching a maximum depth of 2.5 km. A line consists of 25 stories, with three optical modules at each story. An acoustic system provides real-time positioning of the lines to within a few centimeters.

All three Mediterranean telescopes are collaborating on KM3NeT, a full km^3-scale detector in the sea. This detector is still in the technical design phase. The location of such a telescope in the northern hemisphere would be quite complementary to IceCube. The optical properties of the sea water (less scattering, but slightly more absorption compared to ice) mean that a much better angular resolution is possible [77].

Chapter 4

Event Reconstruction and Selection

This chapter discusses the flow of IceCube data from the raw trigger level events to the final analysis-ready data sample. In particular, the first-guess and likelihood-based track reconstructions, the event selection for the "level 1" filter that runs online (L1), and the subsequent offline processing are described.

4.1 Hit Preparation

The output of the IceCube DAQ is a series of waveforms with time stamps and locations. Bayesian-based unfolding algorithms are used to extract a series of the most likely arrival times of single photons, or hits. From studies based on flashers, the leading edges of these hits have a timing uncertainty or 2–3 ns.

The first step in processing these hits is to remove known malfunctioning DOMs. DOMs may be considered bad for a number of reasons: they do not power up or communicate, have high current, have a broken local coincidence connection, or have bad or incomplete calibration records. All together, bad DOMs make up about 2% of the total number of DOMs. Many of these DOMs simply produce no hits, but two poorly calibrated DOMs produced data and had to be removed.

The local coincidence condition ensures that the fraction of hits induced by random noise is small. Nevertheless, the DAQ readout window of $\pm 10\,\mu$s is fairly large compared to the muon detector crossing time of $\sim 5\,\mu$s. The DAQ also merges overlapping windows into single events. The rate of muons from independent CR air showers is substantial ($\sim 13\%$ at trigger level). Having hits from multiple muons in the detector can confuse the reconstructions. For this reason, we use a cleaning procedure with a $6\,\mu$s sliding window. Scanning over the whole event, the time window with the maximum number of hits is found. All hits that fall outside of this time window are removed and not used for reconstruction.

This cleaned series of photon arrival times and their respective locations represents the measured quantities from which we would like to reconstruct the parameters of the original muon and neutrino.

4.2 Track Reconstruction

The ability of a Čerenkov telescope to determine the direction of the incoming particle is of primary importance. The parameters $\vec{a}$ used to describe the muon are summarized in figure 4.1. Assuming an infinite muon track, the parameters are

$$\vec{a} = (\vec{r}_0, t_0, \hat{p}, E_0). \tag{4.1}$$

The muon passes through point $\vec{r}_0 = (x_0, y_0, z_0)$ at time t_0 with energy E_0. The direction of the muon is given by the unit vector in the direction of the momentum $\hat{p}$, decomposed into zenith angle θ and azimuthal angle ϕ.

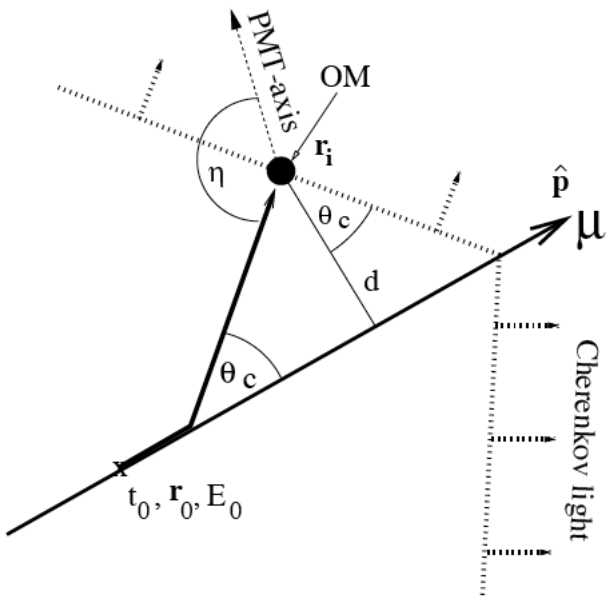

Figure 4.1: Definition of muon track variables shown with the Čerenkov wave front, from [78]. A muon passes through point $\vec{r}_0$ at time t_0 with energy E_0. The direction of the muon is given by the unit vector in the direction of its momentum $\hat{p}$.

4.2.1 Line-Fit First Guess Reconstruction

For now we will only consider the geometry of the muon track, having five parameters. It is often useful to have fast algorithms for determining a first guess for the muon direction. This can be used to overcome computational challenges and the need for a good seed that come along with more sophisticated, maximum likelihood fitting methods.

The line-fit algorithm [79] does not use information about the Čerenkov wavefront or optical properties of the ice but only fits for a plane wave of light moving through the detector with velocity $\vec{v}$. Under this hypothesis, the hits should be connected by a line, taking t_i as the time since t_0:

$$\vec{r_i} = \vec{r}_0 + \vec{v}t_i. \tag{4.2}$$

We can define a χ^2 to minimize:

$$\chi^2 = \sum_{i=1}^{N_{\mathrm{DOMs}}} (\vec{r}_i - \vec{r}_0 - \vec{v}t_i)^2, \tag{4.3}$$

where N_{DOMs} is the number of hit DOMs. We can minimize the χ^2 by differentiating with respect to the free parameters r_0 and $\vec{v}$. This results in the analytically solutions expressed in terms of the average hit times and locations

$$\vec{r_0} = \langle \vec{r_i} \rangle - \vec{v}\langle t_i \rangle \tag{4.4}$$

and

$$\vec{v} = \frac{\langle \vec{r}_i t_i - \langle \vec{r}_i \rangle \langle t_i \rangle}{\langle t_i^2 \rangle - \langle t_i \rangle^2}. \tag{4.5}$$

The direction of the velocity vector serves as a first guess for the direction of the original neutrino [78]. The angular resolution of this first guess technique can be improved substantially with a more sophisticated but more computationally time-consuming maximum likelihood procedure, described next.

4.2.2 Likelihood Reconstruction

The method of maximum likelihood is a well-known technique for estimating a set of unknown parameters $\vec{a}$ (describing the muon) from a set of observed values $\vec{x}_i$

(photon arrival times and locations). The most likely parameters $\vec{a}$ are determined by maximizing the likelihood $\mathcal{L}(\vec{x}_i|\vec{a})$, which is defined as a product over the observed hits:

$$\mathcal{L} = \prod_i p(\vec{x}_i|\vec{a}), \tag{4.6}$$

where $p(\vec{x}_i|a)$ in the probability density function (PDF) of observing a hit $\vec{x}_i$ for the given muon parameters $\vec{a}$. DOMs with no hits are currently ignored. In general, there is rarely an analytic solution and in practice we numerically minimize $-\log\mathcal{L}$ with respect to $\vec{a}$ using the `MINUIT` package [80]. Finding the global minimum is non-trivial and requires substantial investment of computing time. By repeating the `MINUIT` SIMPLEX minimization routine for a broad range of muon track seeds we gain reasonable assurance that the minimizer is not trapped in a local minimum. This iterative minimization is repeated from 1 to 32 times, depending on the processing stage, using pseudo-random (but reproducible) locations on the sky drawn from the Sobol sequence.

For unscattered light, it can be shown that the photons in a Čerenkov cone are expected to arrive at DOM i located at r_i at time

$$t_{\mathrm{geo}} = t_0 + \frac{\vec{p}\cdot(\vec{r}_i - \vec{r}_0) + d\tan\theta_c}{c}, \tag{4.7}$$

where d is the distance of closest approach between the muon and the DOM. In practice it is convenient to transform to a time residual:

$$t_{\mathrm{res}} = t_{\mathrm{hit}} - t_{\mathrm{geo}}, \tag{4.8}$$

which is the difference between the observed hit time and the hit time expected for an unscattered photon, or a "direct hit."

The five free parameters to describe the muon geometry can lead to difficulties in implementation, but with the assumption that the time residuals only depend on the distance d between the muon track and DOM and the inclination angle of the arriving light with respect to the PMT axis η, the PDF becomes a simpler function of three variables:

$$p(\vec{x}_i|\vec{a}) \rightarrow p(t_{\mathrm{res},i}|\vec{a} = d_i, \eta_i). \tag{4.9}$$

In eq. 4.6, the likelihood is formed as the product is over all observed hits, sometimes including more than one hit per DOM. This turns out to be computational challenging, and for that reason the following simplifications are made in this work.

- A single-photo-electron (SPE) likelihood only considers the first photon in each DOM. Technically, the PDFs used to describe the photon arrival times are for a random photon, and in the case of many arriving photons the first is scattered much less than the average case. But the time of the first hit is a robust quantity that changes very little with respect to DOM calibration and the procedure for unfolding the waveform. This robustness makes the SPE reconstruction desirable for online reconstructions, where a decision to write data to disk or tape is made and is not easily undone. The SPE reconstruction also makes for a more accurate seed than line-fit for the multiple-photo-electron (MPE) reconstruction.

- The final MPE reconstruction used for analysis takes advantage of the fact that the first photon is scattered less than the average. The MPE PDF for the first of N photons can be constructed as

$$p_N^1(t_{\text{res}}) = N p_1(t_{\text{res}}) \Big(\int_{t_{\text{res}}}^{\infty} p_1(t) dt \Big)^{N-1}. \tag{4.10}$$

Note the MPE PDF reduces to the SPE PDF when only one photon is observed ($N = 1$). For large N, the MPE PDF is much more sharply peaked compared to SPE. In Monte Carlo simulation studies, the MPE reconstruction performed best with an accurate seed, provided by the SPE result.

4.2.2.1 Pandel Function

If there were no scattering and a perfect detector, $p(t_{\text{res}})$ would be a delta function at $t_{\text{res}} = 0$, the earliest possible physical hit time. With realistic media and detector responses, the distribution is broadened and distorted. The primary factor is scattering in the ice. The Pandel function [78] is an analytic estimate for the arrival time distribution of Čerenkov photons from a monochromatic, isotropic point source. It is a gamma distribution with several free parameters:

$$p(t_{\text{res}}) = \frac{1}{N(d)} \frac{\tau^{-(d/\lambda)} t_{\text{res}}^{(d/\lambda - 1)}}{\Gamma(d/\lambda)} e^{-\big(t_{\text{res}}(\frac{1}{\tau} + \frac{c_{\text{medium}}}{\lambda_a}) + \frac{d}{\lambda_a}\big)}, \tag{4.11}$$

$$N(d) = e^{-d/\lambda_a} \big(1 + \frac{\tau c_{\text{medium}}}{\lambda_a}\big)^{-d/\lambda}. \tag{4.12}$$

Here, $c_{\text{medium}} = c_{\text{vac}}/n$ is the speed of light in ice, λ_a is the absorption length, $\Gamma(d/\lambda)$ is the Gamma function, and $N(d)$ is a normalization factor. Both λ and τ are free parameters, which, although unspecified, are functions of the distance d. These parameters were determined using a Monte Carlo method.

The benefits of the Pandel function are that it is easy to compute and it can be integrated analytically, important for constructing PDFs considering multiple photoelectrons, as in eq. 4.10. The Pandel function is shown in figure 4.2. As d increases, later photon arrival times become much more likely. The function is not defined for $t_{\mathrm{res}} < 0$, and has a pole at $t_{\mathrm{res}} = 0$ for small d, representing the high likelihood of receiving unscattered light. In practice, the function is convoluted with a Gaussian distribution of width 4 ns, a conservative estimate of the time jitter of our detector response (mostly in the PMT transit time). A small constant term is also added to the PDF, representing the random probability of seeing a noise hit. These two steps take care of the pole and the function is left with a small but non-zero probability for $t_{\mathrm{res}} < 0$.

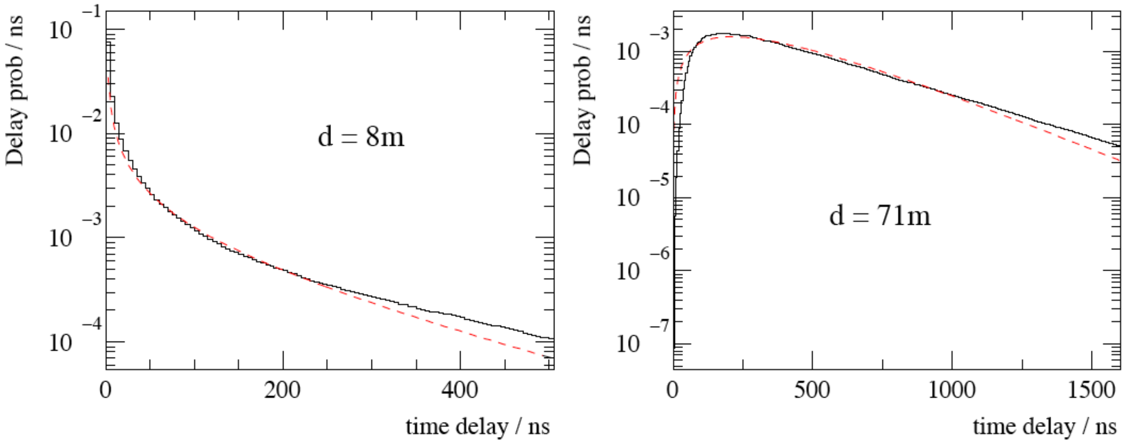

Figure 4.2: Comparison of the Pandel function (red dashed) with detailed simulation (black) at two distances between muon track and DOM. For larger distances, the timing is expected to be delayed with respect to unscattered light.

4.3 Event Selection

This work is done almost entirely using data taken with forty strings of IceCube, in operation under this configuration from 2008 April 5 to 2009 May 20. Although the specifics of selecting events for the final sample will change moderately for future years of IceCube data taking, the principles will remain the same.

Traditional astrophysical neutrino point-source searches have used the Earth to block all upward traveling (up-going) particles except muons induced by neutrinos, as in [81]. There remains a background of up-going muons from neutrinos, which are created in CR air showers and can penetrate the entire Earth. These atmospheric neutrinos have a softer energy spectrum than many expectations for astrophysical neutrinos. The measurement of the atmospheric neutrino spectrum for the 40-string detector is discussed in [82]. A large number of muons produced in CR showers in the atmosphere and moving downward through the detector (down-going) are initially mis-reconstructed as up-going. These mask the neutrino events until quality selections are made, leaving only a small residual of mis-reconstructed events.

The down-going region is dominated by atmospheric muons that also have a softer spectrum compared to muons induced by astrophysical neutrinos. At present, this large background reduces the IceCube sensitivity to neutrino sources in the southern sky in the sub-PeV energy region. While veto techniques are in development which will enable larger detector configurations to isolate neutrino-induced events starting within the detector, point-source searches can meanwhile be extended to the down-going region if the softer-spectrum atmospheric muon background is reduced by an energy selection. This was done for the first time using the previous 22-string config-

Table 4.1. Number of events at each processing level for the 375.5 d of livetime.

Triggered events	3.3×10^{10}
L1 filtered events	8.0×10^{8}
Events in final sample	36,900

uration of IceCube [83], extending IceCube's field of view to −50° declination. In this work we extend the field of view to −85° declination (the exclusion between −85° and −90° is due to the use of scrambled data for background estimation in the analysis, described in chapter 6). Down-going muons can also be created in showers caused by gamma rays, which point back to their source like neutrinos. The possibility for IceCube to detect PeV gamma ray sources in the southern sky is discussed in [84], which concludes that a realistic source could be detected using muons in the ice only after 10 years of observing. Gamma ray sources will not be considered further in this work.

4.3.1 Filtering Levels

Two processing levels are used to reduce the approximately 3.3×10^{10} triggered events first down to a level that can be sent over satellite (35 GB/day), then down to a suitable sample for analysis (see Table 4.1).

4.3.1.1 Online (Level 1) Filter

The Processing and Filtering (PnF) system runs on a computing cluster at the South Pole (L1 filter). This system receives events directly from the DAQ. First, the waveforms are calibrated and a simple extraction of hits from the waveform is performed. At L1, a simplified process is used that only extracts the first photon arrival time and the total number of photons in each DOM. The line-fit track reconstruction is used to seed the first likelihood fit (SPE1). The likelihood fit is performed using the SPE likelihood that uses the time of the leading edge of the first photon arriving in each DOM. A second likelihood fit (SPE2) is performed using the opposite direction of the line-fit as a seed, with the intention of reducing the number of events where the fitter is trapped in a local minimum. These reconstructions yield robust results used for the first level of background rejection.

About 5% of down-going muons which trigger the detector are initially misreconstructed as up-going by the first stages of event processing. A persistent background that grows with the size of the detector is CR muons (or bundles of muons) from different showers which arrive in coincidence. At trigger level they make up about 13% of the events. These coincident muon bundles can mimic the hit pattern of good up-going events, confusing a single-muon fit.

A variety of physics filters run online for selecting potentially interesting events. This work uses only data passing the muon filter or the extremely high energy (EHE) filter. The EHE filter simply requires $\log N_{\mathrm{photons}} \geq 3.5$ in order to keep all high energy events, regardless of the quality or where they came from. The muon filter has two branches.

Branch 1 of the muon filter attempts to keep the highest possible signal efficiency for up-going neutrinos over a wide energy range. Branch 1 extends into the down-going region, but only with increasing energy cuts. A threshold of $N_{\mathrm{DOMs}} \geq 10$ (number of hit DOMs) is applied to all events with both SPE1 and SPE2 zenith angles $\geq 80°$.

Table 4.2. Summary of the online muon filter for the 40-string configuration of IceCube.

Branch	Selection Criteria
Branch 1	$(\theta_{\mathrm{SPE1}}$ AND $\theta_{\mathrm{SPE2}} \geq 80^\circ$ AND $N_{\mathrm{DOMs}} \geq 10)$ OR $(\theta_{\mathrm{SPE1}}$ AND $\theta_{\mathrm{SPE2}} \geq 70^\circ$ AND $N_{\mathrm{DOMs}} \geq 16)$
Branch 2	$N_{\mathrm{pulse}}/N_{\mathrm{DOM}} \geq 5$ AND $\Big((\theta_{\mathrm{SPE1}}$ OR $\theta_{\mathrm{SPE2}} \geq 70^\circ$ AND $N_{\mathrm{DOMs}} \geq 10)$ OR $(\theta_{\mathrm{SPE1}}$ OR $\theta_{\mathrm{SPE2}} \geq 70^\circ$ AND $N_{\mathrm{DOMs}} \geq 10)\Big)$

If both zenith angles only exceed 70°, the number of DOMs hit must be 16 or more. Branch 2 extends the reach of the muon filter, but only for events with the number of pulses per hit DOM is equal or greater than 5. In this case, either SPE1 or SPE2 must reconstruct with zenith angle $\geq 70^\circ$ and $N_{\mathrm{DOMs}} \geq 10$ or either zenith angle $\geq 50^\circ$ and $N_{\mathrm{DOMs}} \geq 20$. The selection logic is summarized in Table 4.2. Events pass this L1 filter at an average rate of about 22 Hz and are buffered before transmission via a communications satellite using the South Pole Archival and Data Exchange (SPADE) system. The efficiency of the L1 filter is shown is figure 4.3 and figure 4.4.

4.3.1.2 Offline (Level 2) Filter

All events transmitted over satellite arrive in a data center for further processing. This offline processing includes a broader base of reconstructions compared to what is done at the South Pole.

Rather than just the simple SPE fit, the multiple photoelectron (MPE) fit uses the number of observed photons to describe the expected arrival time of the first photon. This first photon is scattered less than an average photon when many arrive at the same DOM. The MPE likelihood description uses more available information than

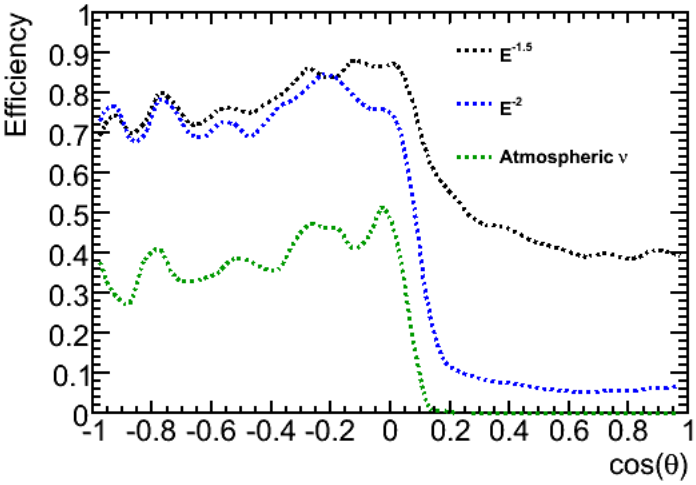

Figure 4.3: L1 filter efficiency versus cosine of the zenith angle (MPE) for three simulated neutrino spectra. Efficiency is calculated with respect to trigger level. Filter efficiency is substantially worse in the down-going range ($\cos\theta > 0$) where strict energy cuts must be applied.

SPE and improves the tracking resolution as energy increases, and this reconstruction is used for the final analysis. The offline processing also provides parameters useful for background rejection, reconstructs the muon energy, and estimates the angular resolution on an event-by-event basis. The Level 2 filtering produces the following cut parameters, used in the final event selection of this work.

- **Zenith angle**, θ_{MPE}: The log-likelihood fit is run using the MPE PDF (eq. 4.11), seeded with 32-iterations of the SPE PDF. Some event selection will depend on the zenith angle from this fit.

- **Reduced log-likelihood**, $\log \mathcal{L}_{\mathrm{MPE}}/(N_{\mathrm{DOMs}} - 5)$: The log-likelihood from the muon track fit divided by the number of degrees of freedom, given by the number of DOMs with hits minus five, the number of free parameters used to describe

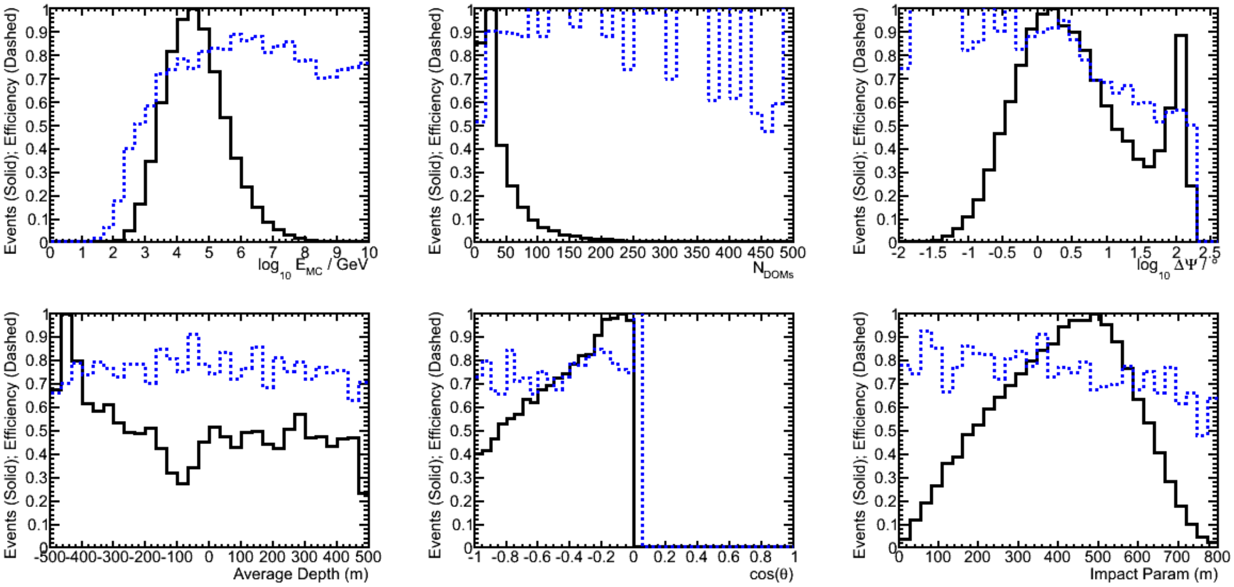

Figure 4.4: L1 filter efficiency (dashed) for up-going simulated E^{-2} neutrinos versus several important quantities (reading order): The true neutrino energy from Monte Carlo, the number of DOMs hit in the event, the angular error of the MPE reconstruction, the average depth of the hits, the cosine of the zenith angle, and the closest approach to the middle of the detector. The average efficiency is 75.6%. The distribution of each quantity at L1 is also shown (solid, arbitrary scaling).

the muon. This parameter is in analogy to the reduced χ^2, which should give an unbiased assessment of the track fit quality (in the case of Gaussian PDFs this corresponds to the reduced χ^2 exactly). This parameter did not perform well on low energy signal events.

- **Modified reduced log-likelihood**, $\log \mathcal{L}_{\mathrm{MPE}}/(N_{\mathrm{DOMs}} - 2.5)$: In studies using both simulation and a mathematical analysis accounting for non-Gaussianity of our reconstruction PDFs, it was determined that changing the number of effective degrees of freedom would provide a track quality parameter that did not have a dependence on energy. In this case, the effective number of degrees of freedom was set to 2.5 instead of 5. Usage of this parameter kept the signal efficiency higher at lower energies.

- **Angular uncertainty**, σ_{MPE}: An estimate of the uncertainty in the muon track direction. The directional likelihood space around the best track solution is sampled and fit to a paraboloid. The contour of the paraboloid traces an error ellipse indicating how well the muon direction is localized [85]. The RMS of the major and minor axes of the error ellipse is used to define a circular error. This parameter is effective both for removing mis-reconstructed events and as an event-by-event angular uncertainty estimator. The error given by the error ellipse does not perform uniformly across all energy ranges. It requires a rescaling correction versus the reconstructed energy, calculated using simulation. Although the cause of this rescaling is not understood, it is likely due to a mismatch between the Pandel function and the real arrival time distributions of photons.

- **Muon energy proxy**, MuE: The average photon density along the muon track, used as a proxy for the muon energy. It is calculated accounting for the distance to DOMs, their angular acceptance, and average scattering and absorption properties of photons in the ice. The energy loss of a muon moving through the detector scales with the muon energy above about 1 TeV when stochastic energy losses due to bremsstrahlung, pair production, and photonuclear interactions dominate over ionization losses. The energy resolution obtained is of the order of 0.3 in the $\log_{10}$ of the muon energy (at closest approach to the average hit location) for energies between about 10 TeV and 100 PeV. Since the interaction vertex is often an unknown distance from the detector, the muon in the detection volume has already lost an unknown amount of energy. Figure 4.5 shows the distribution of this energy parameter versus the true neutrino energy for a simulated spectrum $d\Phi/dE \propto E^{-2}$. Despite the uncertainty on the neutrino energy, for a statistical sample of events this energy estimator is a powerful analysis tool because of the wide range over which energies are measured.

- **Zenith-weighted log-likelihood ratio,** $\log(\mathcal{L}_{\mathrm{SPE}}/\mathcal{L}_{\mathrm{Bayes}})$**:** We can apply Bayes' theorem to our track fits:

$$P(\vec{a}|\vec{x}) = \frac{P(\vec{x}|\vec{a})P(\vec{a})}{P(\vec{x})}. \tag{4.13}$$

The probability (or likelihood) of there being a muon track with parameters $\vec{a}$ given a set of hits $\vec{x}$ is $P(\vec{a}|\vec{x})$, which is proportional to two other probabilities ($P(\vec{x})$ is a constant in the fit and is ignored). The term $P(\vec{x}|\vec{a})$ is the probability for the same muon to produce the set of hits (the same used in our likelihood reconstructions, eq. 4.9). And $P(\vec{a})$ is the prior probability of getting a muon track with parameters $\vec{a}$. In other words, the likelihood fit considers prior information, namely the known zenith distribution of the down-going CR muons. The rate of down-going muons is $O(10^6)$ times higher than up-going muons, so in the absence of convincing evidence, one might guess that any given event is much more likely to be a CR muon. Following that argument, a high likelihood ratio between an unbiased SPE muon track fit and a fit with the zenith-angle weighted according to the known down-going muon zenith distribution as a Bayesian prior establishes strong evidence that the event is actually up-going and not a mis-reconstructed down-going event. For each fit, 32 seed iterations are performed.

- **Number of Direct Hits**, $NDir$: The number of DOMs with direct photons, defined as arriving within -15 ns to $+75$ ns of the expectation from an unscattered photon emitted from the reconstructed muon track at the Čerenkov angle. Scattering of photons in the ice causes a loss of directional information and will delay them with respect to the unscattered expectation.

- **Length of Direct Hits**, $LDir$: The maximum length between direct photons, projected along the best muon track solution.

- **Minimum zenith of split events**, $\theta_{\mathrm{split,min}}$: The zenith angles resulting from splitting of an event into two parts and reconstructing each part separately. This is done in two ways: temporally, by using the mean photon arrival time as the split criterion; and geometrically, by using the plane both perpendicular to the track and containing the average hit location as the split criterion. This technique is effective against coincident muon bundles mis-reconstructed as single up-going tracks if the minimum zenith angles of all split fits $\theta_{\mathrm{split,min}}$ is required to be nearly up-going.

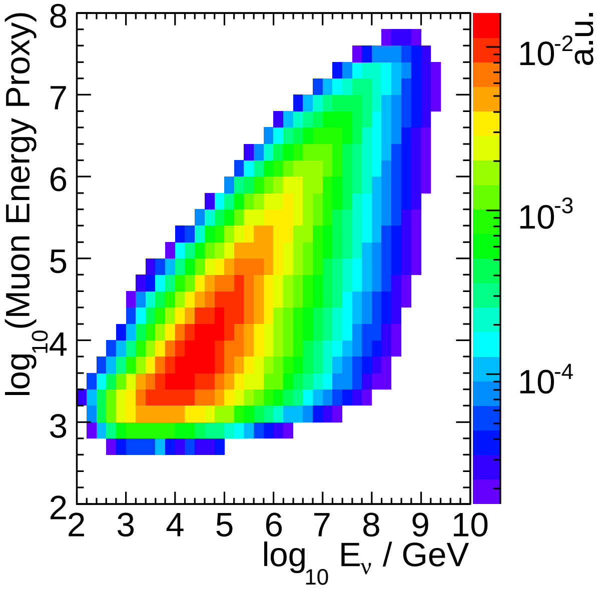

Figure 4.5: Distribution of the muon energy proxy (energy loss observed in the detector) versus the true neutrino energy for a flux $d\Phi/dE \propto E^{-2}$.

4.3.1.3 Final Event Selection

The event selection used to obtain the final sample is:

$$\begin{aligned}
&\Big[\sigma_{\mathrm{MPE}} < 3^\circ \text{ AND} && (4.14)\\
&\ \log\mathcal{L}_{\mathrm{MPE}}/(N_{\mathrm{DOMs}} - 5) < 8.3 \text{ AND}\\
&\ \big(\log\mathcal{L}_{\mathrm{MPE}}/(N_{\mathrm{DOMs}} - 5) < 8.0 \text{ OR } \log\mathcal{L}_{\mathrm{MPE}}/(N_{\mathrm{DOMs}} - 2.5) < 7.1\big) \text{ AND}\\
&\ \theta_{\mathrm{split,min}} > 80^\circ \text{ AND}\\
&\ (\log(\mathcal{L}_{\mathrm{SPE}}/\mathcal{L}_{\mathrm{Bayes}}) > 30 \text{ OR } \theta_{\mathrm{MPE}} < 90^\circ) \text{ AND}\\
&\ NDir \geq 5 \text{ AND}\\
&\ LDir > 200\,\mathrm{m}\Big] \text{ OR}\\
&\Big[\sigma_{\mathrm{MPE}} < 1.5^\circ \text{ AND}\\
&\ \log\mathcal{L}_{\mathrm{MPE}}/(N_{\mathrm{DOMs}} - 5) < 7.5 \text{ AND}\\
&\ \log MuE > f_{MuE}(\theta_{\mathrm{MPE}})\Big],
\end{aligned}$$

where $f_{MuE}(\theta_{\mathrm{MPE}})$ is an energy threshold that increases as the down-going muon background increases. The threshold is determined by performing a fit in order to keep a fixed number of events per solid angle. The fitting function is a polynomial:

$$f_{MuE}(\theta_{\mathrm{MPE}}) = \begin{cases} 0 & \cos\theta_{\mathrm{MPE}} \leq 0.05 \\ f_0 + f_1\cos\theta_{\mathrm{MPE}} + f_2\cos^2\theta_{\mathrm{MPE}} + \ldots & \cos\theta_{\mathrm{MPE}} > 0.05. \end{cases} \tag{4.15}$$

The coefficients $f_0, f_1, \ldots$ are given in Table 4.3 and the function is shown in figure 4.6. For nearly up-going muons, the threshold of 0 means there is effectively no threshold.

Table 4.3. Polynomial coefficients for eq. 4.15.

Parameter	Value
f_0	4.8×10^{-1}
f_1	6.9×10^{1}
f_2	-5.0×10^{2}
f_3	2.3×10^{3}
f_4	-6.7×10^{3}
f_5	1.3×10^{4}
f_6	-1.7×10^{4}
f_7	1.4×10^{4}
f_8	-6.2×10^{3}
f_9	1.2×10^{3}

The first set of square brackets in eq. 4.14 targets the up-going region. The zenith-weighted likelihood ratio and event splitting are specifically designed to remove down-going atmospheric muon backgrounds that have been mis-reconstructed as up-going while the other parameters focus on achieving at least a moderate track quality.

The second set of square brackets in eq. 4.14 targets the down-going region. Without a veto or earth filter, muons from CR showers overwhelm neutrino-induced muons, except possibly at high energies if the neutrino source spectra are harder than the CR spectrum. The aim of the analysis in this region is therefore to select high energy, well-reconstructed events. We require a much higher track quality than in the up-going range. Energy cuts were introduced in the down-going region to reduce the number of events to a suitable size, cutting to achieve a constant number of events per solid angle (which also simplifies the background estimation in the analysis). This technique keeps the high energy events which are most important for discovery. The efficiency of the final event selection is shown is figure 4.3 and figure 4.4.

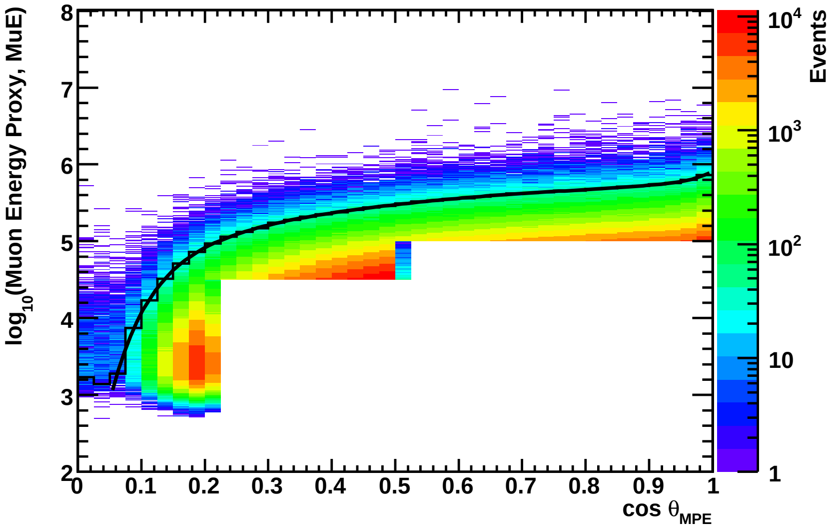

Figure 4.6: Energy estimator threshold versus the zenith angle $f_{MuE}(\theta_{\mathrm{MPE}})$ (black continuous). The fit is performed on the black histogram, constructed to give a fixed number of events per 0.05 in $\cos\theta_{\mathrm{MPE}}$. The color scale shows the data distribution. Some rectangular pre-cuts are visible, applied to speed up the fitting procedure. These cuts are above the L1 filter cuts, but still safely below the final cut level.

Cuts were optimized for the best sensitivity using a simulated signal of muon neutrinos with spectrum $d\Phi/dE \propto E^{-2}$. We checked that the same cuts resulted in a nearly optimal sensitivity for a softer spectrum $d\Phi/dE \propto E^{-3}$ in the up-going region where low energy sensitivity is possible and for a harder spectrum $d\Phi/dE \propto E^{-1.5}$ in the down-going region.

Boosted decision trees (BDTs), as implemented by [86], were also investigated as an alternative to straight cuts. No improvement for E^{-2} sources was observed, although BDTs are used for the atmospheric neutrino spectral analysis because of the higher atmospheric neutrino efficiency [82]. Some improvement in the point-source

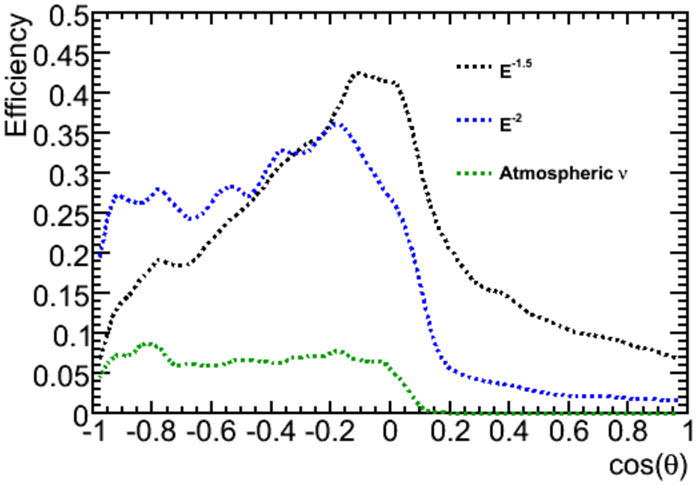

Figure 4.7: Final selection efficiency versus cosine of the zenith angle (MPE) for three simulated neutrino spectra. Efficiency is calculated with respect to trigger level. Only for very hard spectra, such as $E^{-1.5}$, do up- and down-going efficiencies become comparable to each other.

sensitivity was possible for softer spectra ($\sim$ 15% improved sensitivity for E^{-3}), but the transparency of straight cuts was still deemed advantageous.

Of the 36,900 events passing all selection criteria, 14,121 are up-going events from the northern sky, mostly muons induced by atmospheric neutrinos. Simulations of CR air showers with CORSIKA [87] show a 2.4±0.8% contamination due to mis-reconstructed down-going atmospheric muons. The other 22,779 are down-going events from the southern sky, mostly high energy atmospheric muons. An equatorial sky map of these events is given in figure 4.9.

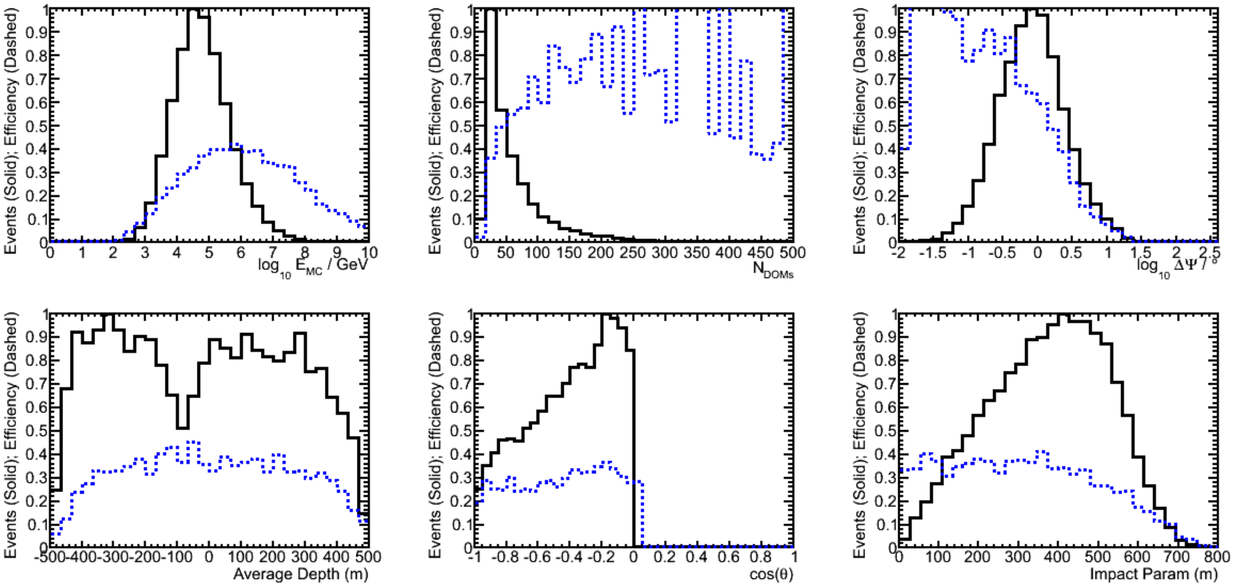

Figure 4.8: Final selection efficiency for up-going simulated E^{-2} neutrinos versus several important quantities (reading order): The true neutrino energy from Monte Carlo, the number of DOMs hit in the event, the angular error of the MPE reconstruction, the average depth of the hits, the cosine of the zenith angle, and the closest approach to the middle of the detector. The average efficiency is 29.5%. The distribution of each quantity at final cut level is also shown (solid, arbitrary scaling).

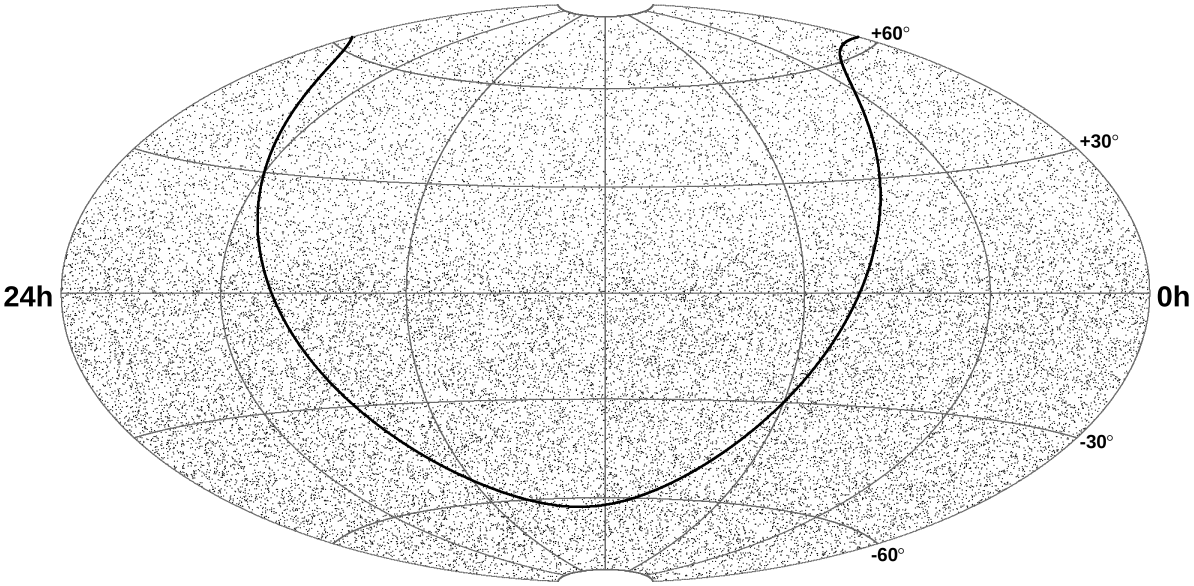

Figure 4.9: Equatorial skymap (J2000) of the 36,900 events in the final sample. The galactic plane is shown as the solid black curve. The northern sky (positive declinations) is dominated by up-going atmospheric neutrino-induced muons, and the southern sky (negative declinations) is dominated by muons produced in cosmic ray showers in the atmosphere above the South Pole.

Chapter 5

Simulation and Comparison to Data

This chapter describes the simulation of signal and background, including a detailed detector response. `CORSIKA` [87] is used to generate cosmic ray (CR) air showers. Neutrino generation is based on `ANIS` [88]. The charged leptons and other secondaries are propagated through the ice, photons tracked to DOMs, and the DOM response simulated. The simulation output then matches the output of the real IceCube DAQ and both are processed identically. In order to demonstrate the validity of the simulation, we show comparisons between the data and Monte Carlo (MC) samples at many cut levels. Impact from the uncertainty in the CR composition is discussed. Within the uncertainties from the models, our background simulation agress well with our data in important parameters. Finally, the simulation is used to characterize the detector performance for a point-source search.

Physics interpretation of the IceCube data requires an accurate Monte Carlo (MC) simulation. Calculating upper limits, understanding background contamination, parameterizing the detector response to build likelihood analyses: all these depend on a reliable simulation. Such a simulation for the IceCube detector happens in three stages:

- **Event generation**: Primary particles are created at the surface of the atmosphere based on physical models. These models interpolate data from direct and indirect CR measurements or hypothesized astrophysical signals.

- **Propagation**: The primary particles are tracked through various media, such as the atmosphere, rock in earth, or ice near the detector. Secondary particles produced in interactions during propagation are tracked, including charged leptons and Čerenkov photons.

- **Detector Response**: The response of the IceCube detector to the Čerenkov photons is simulated with substantial detail, including the PMT response, electronics within the DOM, and the trigger logic.

5.1 Event Generation

5.1.1 Neutrino Simulation

Simulation of neutrinos is used for determining event selection and calculating upper limits. The simulation of neutrinos is based on `ANIS` (All Neutrino Interaction Simulation) [88]. Deep inelastic neutrino-nucleon cross sections use CTEQ5 parton distribution functions [89]. Neutrinos are first created at random positions on the Earth's surface with an energy between 100 GeV and 10^{10} GeV and directed toward the IceCube detector. They are propagated through the Earth, taking into account neutrino absorption from CC and reprocessing from NC interactions (see figure 2.7). The density of the Earth used by `ANIS` comes from the Preliminary Reference Earth Model [90]. In order to reduce computation time, neutrinos that are not absorbed *en route* are forced to interact within the detection volume, which scales with the maximum muon range for a given energy. A weight representing the actual probability of interaction is assigned to each event. We generate an E^{-1} spectrum of neutrinos, which can be used to model backgrounds but gives better event statistics for high energy signals.

Neutrino simulation can be weighted for different fluxes, accounting for the probability of each event to occur. In this way, the same simulation sample can be used to represent atmospheric neutrino models such as Bartol [91] and Honda [92] neutrino fluxes from pion and kaon decays (conventional flux). Neutrinos from charmed meson decays (prompt flux) have been simulated according to a variety of models [93, 94, 95]. Seasonal variations in atmospheric neutrino rates are expected to be a maximum of ±4% for neutrinos originating near the polar regions. Near the equator, atmospheric variations are much smaller, and the variation in the number of events is expected to be less than ±0.5% [96].

5.1.2 Atmospheric Muon Simulation

Atmospheric muon background is simulated mostly to guide and verify the event selection. Muons from CR air showers were simulated with `CORSIKA` (COsmic Ray Simulations for KAscade) [87] with the SIBYLL hadronic interaction model [97]. We perform simulations with a “natural” weighting ($\sim E^{-2.7}$) as well as with the power in energy increased by one in order to gain higher event statistics and reduce statistical uncertainties at the important higher energies. The simulation is then weighted to represent our expectations from nature.

An October polar atmosphere, an average case over the year, is used for the

`CORSIKA` simulation, ignoring the seasonal variations of ±10% in event rates [71].

5.2 Propagation

5.2.1 Charged leptons

Once the generator produces potentially detectable secondary particles, these are passed off to the propagator. We use `Muon Monte Carlo` (`MMC`) [54] to propagate these secondaries through rock and ice. Energy losses due to continuous ionization and stochastic processes, discussed in section 2.3, are taken into account. Any Čerenkov photons are passed to the photon transport simulation.

5.2.2 Čerenkov Photons

A software package called `Photonics` [98] is used to propagate Čerenkov photons from creation to the arrival at a DOM or absorption in ice. This code uses the measured properties of the ice discussed in section 3.5. A simulation is used to make look-up tables for the arrival time probability distribution function of photons versus depth and covering all distances from parent particle to DOM. Although creating the tables is computationally time consuming, photon simulations can then be accomplished much faster compared to direct tracking. The binning of the tables does introduce some smearing of the ice structure compared to direct photon tracking methods.

5.3 Detector Simulation

If any photon intercepts the glass sphere of a DOM, that photon is handed to the detector response simulation. Simulation specific to the IceCube Neutrino Observatory is contained in the `IceSim` package. The PMT simulator accounts for the transparency of the glass and gel, as well as the quantum efficiency of the PMT before creating a PMT waveform. Next, the DOM simulator simulates the functionality of the DOM main board, including the PMT base transformer, the PMT discriminator, the waveform digitization, and the local coincidence condition. Lastly, the trigger simulation checks to see if the event satisfies the trigger condition required for reading out the detector. After the trigger condition is satisfied, experimental and simulated data are processed and filtered in the same way. Of course, the simulation records extra information about the simulated parent and secondaries, such as their energy and direction, that is not available in the experimental data stream.

5.4 Data and MC Comparisons

In figure 5.1 we show the cosine of zenith and in figure 5.2 the muon energy proxy, reduced log-likelihood, and angular uncertainty estimator distributions of all events at trigger level, L1 filter level, and after final analysis cuts for data and Monte Carlo (MC). In these figures, the simulation uses a slightly modified version of the *poly-gonato* model of the galactic CR flux and composition [13]. Above the galactic model cutoff at $Z \times 4 \times 10^{15}$ eV, a flux of pure iron is used with an E^{-3} spectrum. This is done because currently CORSIKA cannot propagate elements in the *poly-gonato* model that are heavier than iron. Moreover, the *poly-gonato* model only accounts for galactic CRs and does not fully account for the average measured flux above 10^{17} eV, even when all nuclei are considered (see figure 11 in [13]). These corrections then reproduce the measured CR spectrum at these energies. There is a 23% difference in normalization of data and CR muon events at trigger level. This normalization offset largely disappears after quality cuts are made. Generally good agreement is achieved at later cut levels.

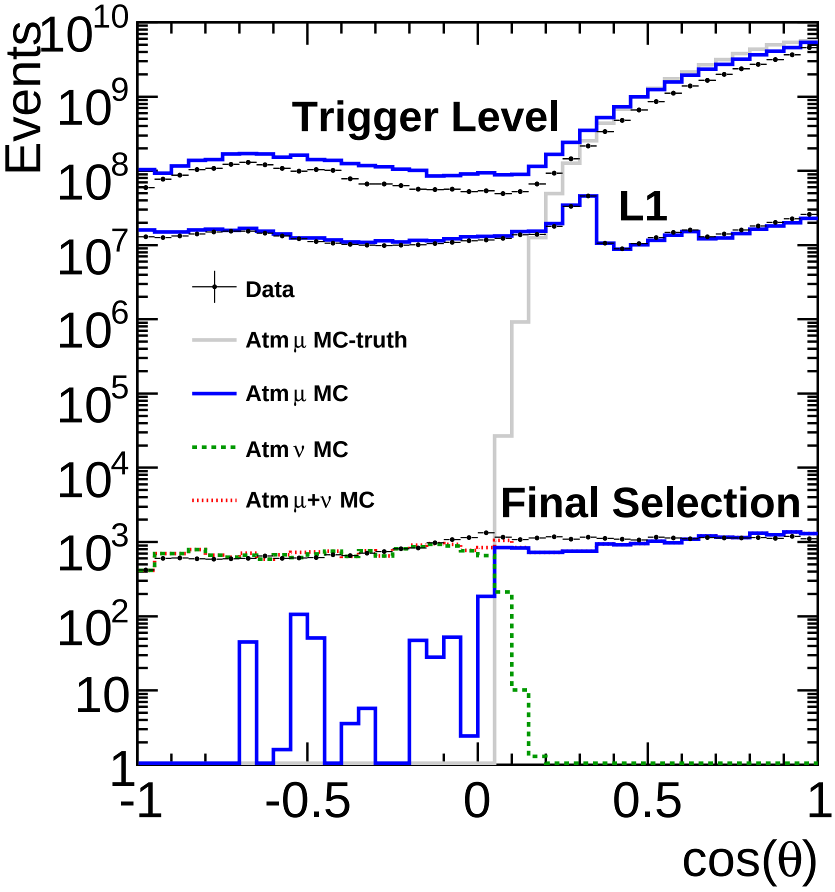

Figure 5.1: Distribution of reconstructed cosine zenith at trigger level, L1, and final cut level for data and simulation of atmospheric muons [13] and neutrinos [91, 95]. The true cosine zenith distribution of the muons at trigger level is also shown.

Figure 5.1 shows some disagreement between data and simulation for zenith angles around 80°. Muons created in CR showers in the atmosphere near this zenith angle must travel about 15–20 km to reach the bottom of IceCube. Only very high energy muons can travel such distances. For the simulation to produce the correct

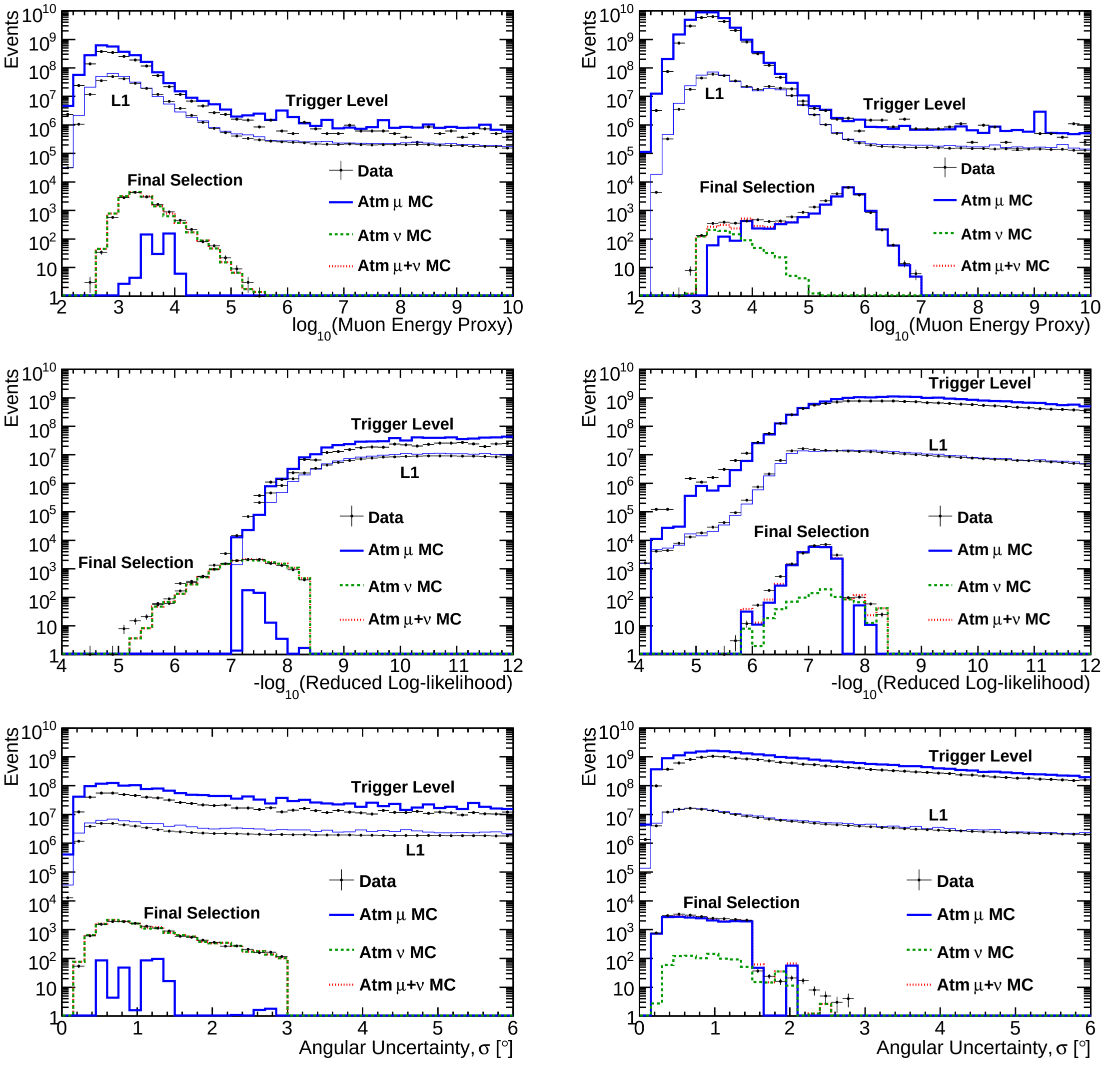

Figure 5.2: Distributions of muon energy proxy (top row), reduced log-likelihood (middle row), and angular uncertainty estimator (bottom row) for the up-going sample (left column) and the down-going sample (right column). Each is shown at trigger level, L1, and final cut level for data and simulation of atmospheric muons and neutrinos. In the up-going sample (left column), all atmospheric muons are mis-reconstructed, and at final level their remaining estimated contribution is about 2.4±0.8%.

zenith distribution for these nearly horizontal events, CR composition can be important since protons can produce higher energy muons than iron nuclei with the same energy.

In addition to the slightly modified version of the *poly-gonato* model, discussed above, a simpler pure proton and iron two-component model with a much higher contribution of protons is used for comparison [99]. The final zenith distribution with each of these models is shown in figure 5.3. The atmospheric muon simulation is not only affected by the primary composition uncertainties at high energy; it is also affected by the hadronic model, affecting the production rate of muons at the level of 15% in the region of interest for IceCube, greater than about 1 TeV, as discussed in the SIBYLL model paper [97] and in the comparison between different hadronic models used in CORSIKA presented in [100].

For the up-going region, several models of atmospheric neutrino fluxes, both conventional fluxes from pion and kaon decay and prompt fluxes from charmed meson decay, are shown in figure 5.3. To represent the low and high predictions, conventional and prompt models are used in pairs: Honda [92] for the conventional flux paired with Sarcevic [94] for the prompt flux represent the low prediction, and Bartol [91] for the conventional flux paired with Naumov [95] for the prompt flux represent the high prediction. Additional uncertainty in the predicted atmospheric neutrino rate is estimated to be about 40% at 1 TeV [101]. We conclude that our data agree with background simulation at the final level, within the range of uncertainties allowable by existing CR composition and atmospheric neutrino models.

5.5 Atmospheric Neutrino Spectrum

Detailed studies have been performed using IceCube data to reconstruct the atmospheric neutrino spectrum [47, 40, 82]. Although these studies are based on some-

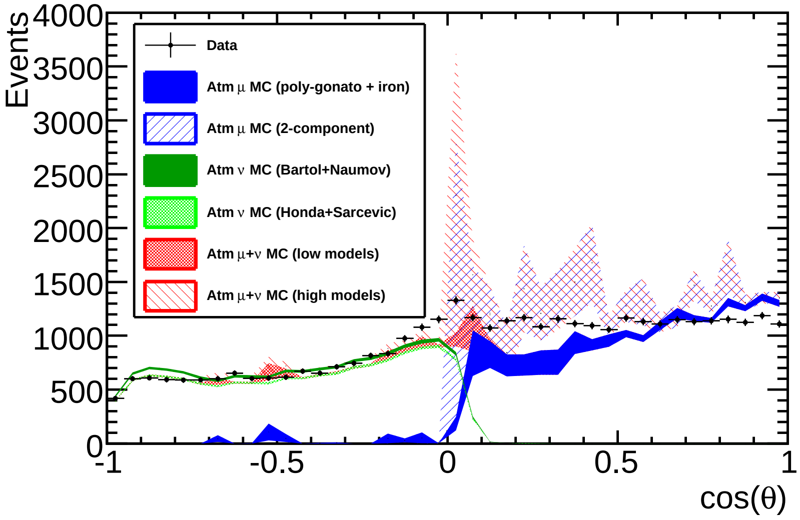

Figure 5.3: Distribution of reconstructed cosine zenith for the final event sample compared to the models discussed in the text. Honda and Sarcevic are summed with *poly-gonato* to represent the set of low predictions, and Bartol and Naumov are summed with the 2-component model for the high predictions. Only statistical errors are shown. The two-component model has limited statistics, causing the peaks and valleys. Systematic uncertainties of neutrino production in CR showers are estimated to be about 40% at 1 TeV [101] and 15% in the muon rate greater than about 1 TeV [97, 100].

what different event selection, their ability to match the predicted spectrum demonstrates a high degree of validity of the simulation. The results of these studies are summarized in figure 5.4.

5.6 Detector Performance

The performance of the detector for a point-source analysis can be characterized using the signal simulation. For a spectrum of neutrinos $d\Phi/dE \propto E^{-2}$, the median angular difference between the neutrino and the reconstructed direction of the muon in the northern (southern) sky is 0.8° (0.6°). Along with more severe quality selection

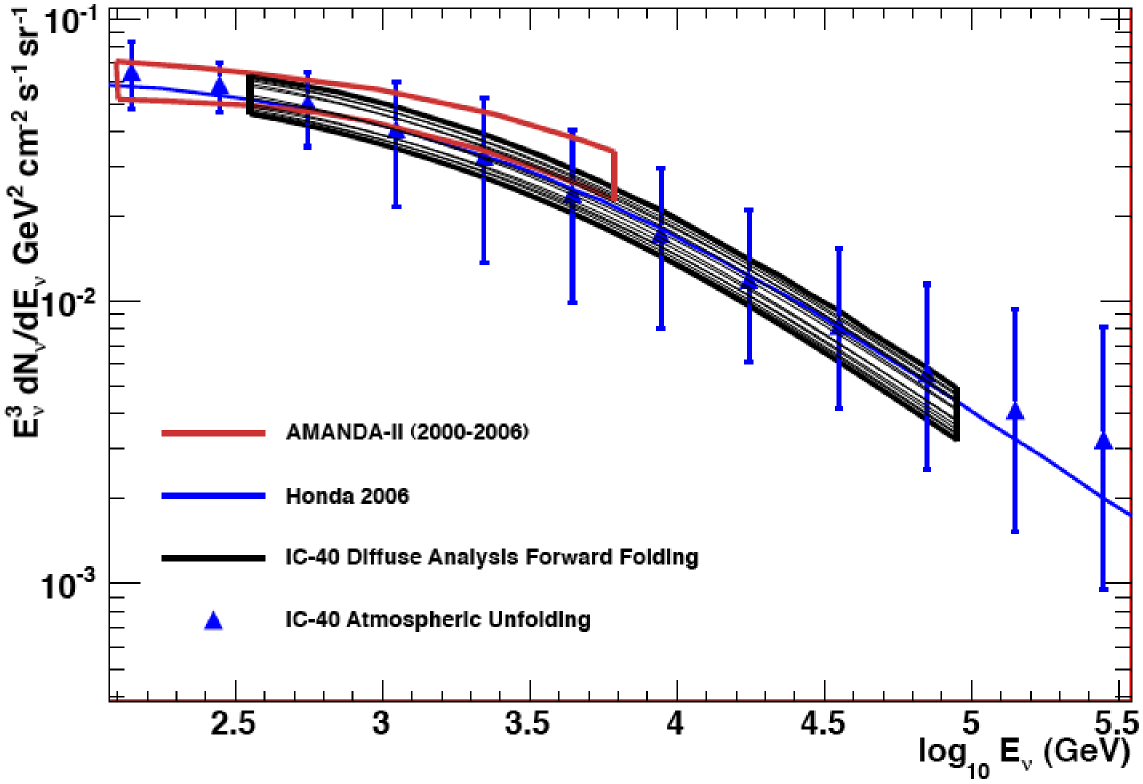

Figure 5.4: Measurements of the atmospheric neutrino flux and the model prediction from Honda [92]. The set of black curves, representing the statistical and systematic error band comes from a forward folding of IceCube 40-string data [47, 40]. The blue triangles are from an unfolding analysis of IceCube 40-string data [82]. The red area is a forward folding result using AMANDA-II data [102].

in the southern sky, the different energy distributions in each hemisphere, shown in figure 5.5, cause the difference in these two values. This is because the reconstruction performs better at higher energy due to the larger amount of light and longer muon tracks. The cumulative point spread function (PSF) is shown in figure 5.6 for two energy ranges and compared with simulation of the complete IceCube detector using the same quality selection, as well as the median PSF versus energy for the two hemispheres.

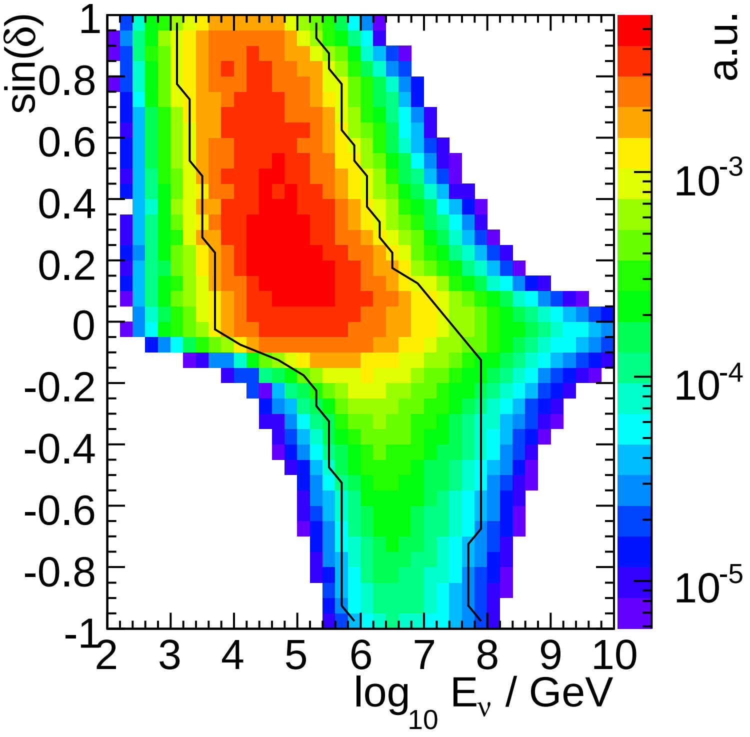

Figure 5.5: Energy distribution for a flux $d\Phi/dE \propto E^{-2}$ of neutrinos as a function of declination for the final event selection. The black contours indicate the 90% central containment interval for each declination.

The neutrino effective area A_ν^{eff} is a useful parameter to determine event rates and the performance of a detector for different analyses and fluxes. The expected event rate for a given differential flux $d\Phi/dE$ is

$$N_{\mathrm{events}}(\delta_\nu) = \int dE_\nu A_\nu^{\mathrm{eff}}(E_\nu, \delta_\nu) \frac{d\Phi_\nu(E_\nu, \delta_\nu)}{dE_\nu}\,, \tag{5.1}$$

and is calculable using simulation. The A_ν^{eff} represents the size of an equivalent detector if it were 100% efficient. Figure 5.7 shows the A_ν^{eff} for fluxes of $\nu_\mu + \bar{\nu}_\mu$ and $\nu_\tau + \bar{\nu}_\tau$, for

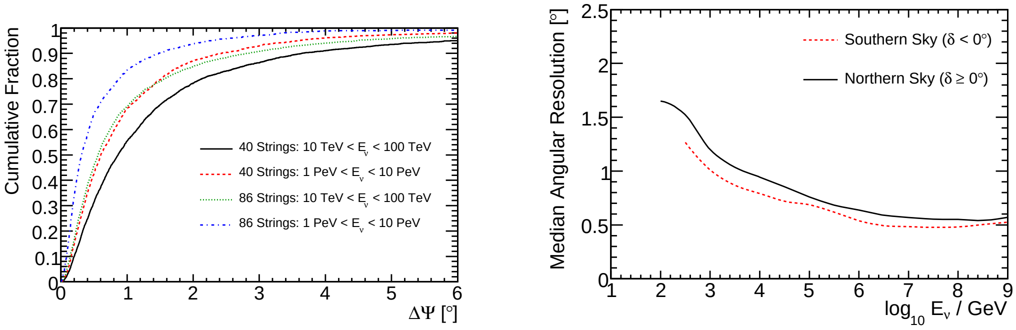

Figure 5.6: Cumulative point spread function (angle between neutrino and reconstructed muon track) for simulated neutrino signal events following a spectrum $d\Phi/dE \propto E^{-2}$ at the final cut level in the up-going region (left). Also shown is the same distribution for the final IceCube configuration. The median of the PSF versus energy is shown separately for the northern and southern skies (right). The improvement in the southern sky is because of the more restrictive quality cuts.

events at final selection level. Neutrinos arriving from the highest declinations must travel through the largest column depth and can be absorbed: this accounts for the turnover at high energies for nearly vertical up-going muon neutrinos. Tau neutrinos have the advantage that the tau secondary can decay back into a tau neutrino before losing much energy.

Although tau (and electron) neutrino secondaries usually produce nearly spherical showers rather than tracks, tau leptons will decay to muons with a 17.7% branching ratio [103]. At very high energy (above about 1 PeV), a tau will travel far enough before decaying that the direction can be reconstructed well, contributing to any extraterrestrial signal in the muon channel. For the upper limits quoted in chapter 9, we must make an assumption on the flavor ratios at Earth, after oscillations. It is common to assume $\Phi_{\nu_e} : \Phi_{\nu_\mu} : \Phi_{\nu_\tau} = 1 : 1 : 1$. This is physically motivated

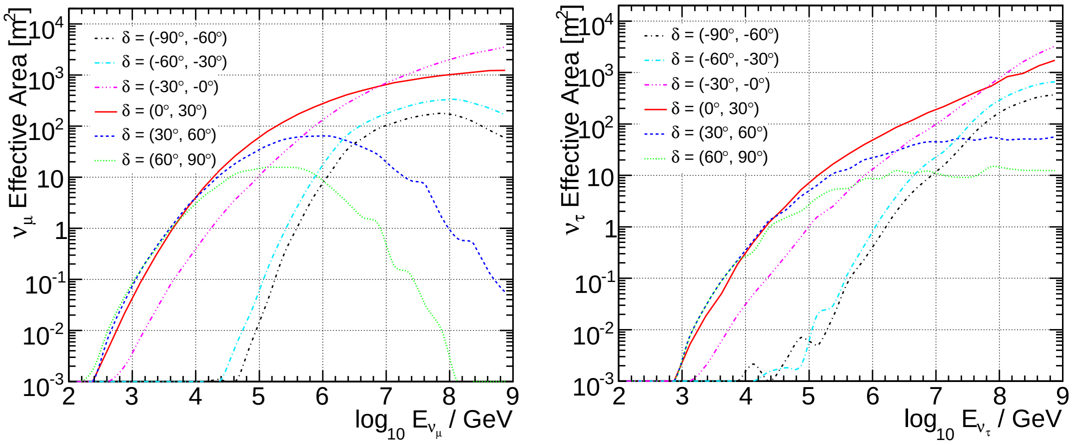

Figure 5.7: Solid-angle-averaged effective areas at final cut level for astrophysical neutrino fluxes in six declination bands for $\nu_\mu + \bar{\nu}_\mu$ (left) and $\nu_\tau + \bar{\nu}_\tau$ (right), assuming an equal flux of neutrinos and anti-neutrinos.

by neutrino production from pion decay and the subsequent muon decay, yielding $\Phi_{\nu_e} : \Phi_{\nu_\mu} : \Phi_{\nu_\tau} = 1 : 2 : 0$. After standard oscillations over astrophysical baselines, this gives an equal flux of each flavor at Earth [37]. For a spectrum $d\Phi/dE \propto E^{-2}$ and equal muon and tau neutrino fluxes, the fraction of tau neutrino-induced events is about 17% for vertically down-going, 10% for horizontal, and 13% for vertically up-going. Because the contribution from tau neutrinos is relatively small, assuming only a flux of muon neutrinos can be used for convenience and to compare to other published limits. We have tabulated limits on both Φ_{ν_μ} and the sum $\Phi_{\nu_\mu} + \Phi_{\nu_\tau}$, assuming an equal flux of each, while in the figures we have specified that we only consider a flux of muon neutrinos. Limits are always reported for the flux at the surface of the Earth.

Chapter 6

Search Method

An unbinned maximum likelihood method to search for point sources of neutrinos is discussed in detail. This method allows full use of spatial and spectral information from the data. The data are hypothesized to be a mixture of events from signal and background. The best mixture (maximum likelihood) is found and used to compute a p-value (chance probability under the null-hypothesis) and flux upper limits. Modifications to the point-source method are made in order to stack many sources in a fully general way and to search for spatially extended sources.

6.1 Maximum Likelihood Method

An unbinned maximum likelihood ratio method is used to look for a localized, statistically significant excess of events above the background. We also use energy information to help separate possible signal from the known backgrounds.

The method follows that of [104]. The data are modeled as a two component mixture of signal and background. A maximum likelihood fit to the data is used to determine the relative contribution of each component. Given N events in the data set, the probability density of the ith event is

$$\frac{n_s}{N}\mathcal{S}_i + (1 - \frac{n_s}{N})\mathcal{B}_i, \tag{6.1}$$

where $\mathcal{S}_i$ and $\mathcal{B}_i$ are the signal and background probability density functions (PDFs), respectively. The parameter n_s is the unknown contribution of signal events.

6.1.1 Signal PDF

For an event with reconstructed direction $\vec{x}_i = (\alpha_i, \delta_i)$, we model the probability of originating from the source at $\vec{x}_s$ as a circular two-dimensional Gaussian,

$$\mathcal{N}(\vec{x}_i) = \frac{1}{2\pi\sigma_i^2} e^{-\frac{|\vec{x}_i - \vec{x}_s|^2}{2\sigma_i^2}}, \tag{6.2}$$

where σ_i is the angular uncertainty reconstructed for each event individually [85] and $|\vec{x}_i - \vec{x}_s|$ is the space angle difference between the source and reconstructed event. The PSF for different ranges of σ_i are in figure 6.1, showing the correlation between the estimated angular uncertainty and track reconstruction error.

The energy PDF $\mathcal{E}(E_i|\gamma, \delta_i)$ describes the probability of obtaining a reconstructed muon energy E_i for an event produced by a source of a given neutrino energy spectrum $E^{-\gamma}$ at declination δ_i. We describe the energy distribution using 22 declination bands. Twenty bands, spaced evenly by solid angle, cover the down-going range where the energy distributions are changing the most due to the energy cuts in the event selection, while two are needed to sufficiently describe the up-going events, with the separation at $\delta = 15°$. We fit the source spectrum with a power law $E^{-\gamma}$; γ is a free parameter. The probability of obtaining a reconstructed muon energy E_i for

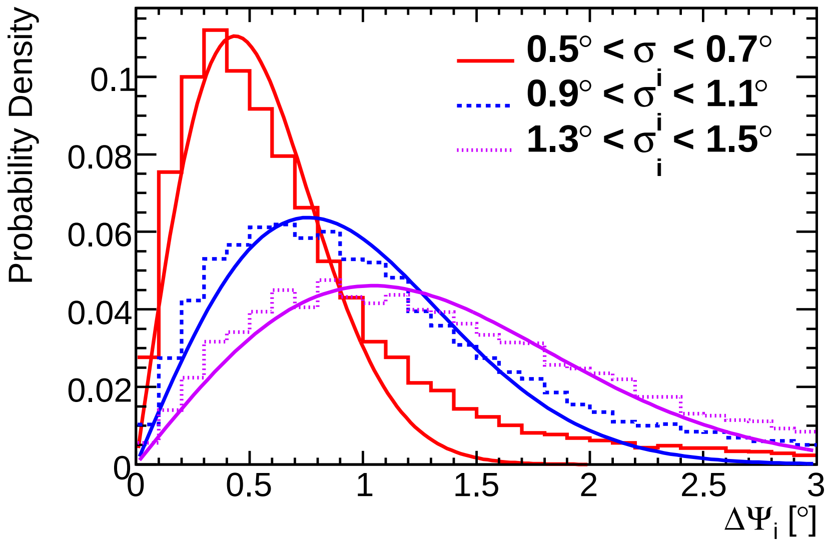

Figure 6.1: Angular deviation between neutrino and reconstructed muon direction $\Delta\Psi$ for ranges in σ_i, the reconstructed angular uncertainty estimator. Fits of these distributions to two-dimensional Gaussians projected into $\Delta\Psi$ are also shown. The value of σ_i is correlated to the track reconstruction error. A small fraction of events are not well-represented by the Gaussian distribution, but these are the least well-reconstructed events and contribute the least to signal detection.

an event produced by a source with spectral index γ, for spectral indices $1.0 < \gamma < 4.0$, is determined using simulation. Two examples of these energy PDFs are shown in figure 6.2.

The full signal PDF is given by the product of the spatial and energy PDFs:

$$\mathcal{S}_i = \mathcal{N}(\vec{x}_i) \cdot \mathcal{E}(E_i|\gamma, \delta_i). \tag{6.3}$$

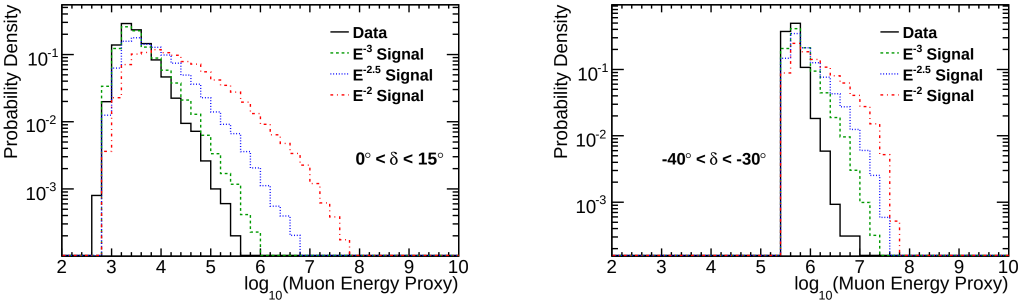

Figure 6.2: Probability densities for the muon energy proxy for data as well as simulated power-law neutrino spectra. Two declination bands are shown: $0° < \delta < 15°$ (left) and $-40° < \delta < -30°$ (right), representing two of the declination-dependent energy PDFs used in the likelihood analysis. There is an energy cut applied for negative declinations.

6.1.2 Background PDF

The background PDF $\mathcal{B}_i$ contains the same terms, describing the angular and energy distributions of background events:

$$\mathcal{B}_i = \mathcal{N}_{Atm}(\vec{x}_i) \cdot \mathcal{E}(E_i|Atm, \delta_i), \tag{6.4}$$

where $\mathcal{N}_{Atm}(\vec{x}_i)$ is the spatial PDF of atmospheric background and $\mathcal{E}(E_i|Atm, \delta_i)$ is the probability of obtaining E_i from atmospheric backgrounds (neutrinos and muons) at the declination of the event. These PDFs are constructed using data and, for the energy term, in the same 22 declinations bands as the signal PDF. All non-uniformities in atmospheric background event rates caused by the detector acceptance or seasonal variation average out in the time-integrated analysis. Therefore $\mathcal{N}_{Atm}(\vec{x}_i)$ has a flat expectation in right ascension and is only dependent on declination. Because the data are used in this way for background estimation, the analysis is restricted from $-85°$

to 85° declination, so that any point source signal will still be a small contribution to the total number of events in the same declination region.

6.1.3 Test Statistic

The likelihood of the data is the product of all event probability densities:

$$\mathcal{L}(n_s,\gamma) = \prod_{i=1}^{N} \Big[\frac{n_s}{N}\mathcal{S}_i + (1 - \frac{n_s}{N})\mathcal{B}_i \Big]. \tag{6.5}$$

The likelihood is then maximized with respect to n_s and γ, giving the best fit values $\hat{n}_s$ and $\hat{\gamma}$. The null hypothesis is given by $n_s = 0$ (γ has no meaning when no signal is present). Negative values of n_s are assigned a $TS = 0$. The likelihood ratio test statistic is

$$TS = \begin{cases} -2\log\dfrac{\mathcal{L}(n_s=0)}{\mathcal{L}(\hat{n}_s,\hat{\gamma}_s)} & n_s \geq 0, \\ 0 & n_s < 0. \end{cases} \tag{6.6}$$

6.2 Hypothesis Testing

This likelihood ratio test statistic is used to perform statistical tests. The results of these tests can be clearly defined in the context of testing between two hypotheses. One is called H_0, the null hypothesis, or the default accepted hypothesis. The other is called the alternative hypothesis H_1. In our case, H_0 is often represented by the case of background only ($n_s = 0$), and H_1 is the case where some signal events are present. The value of TS can be used to establish criteria for accepting one hypothesis and rejecting the other.

The usefulness of a statistical test is given by the rate of of type-I and type-II errors. Type-I errors occur when H_0 is rejected but true (i.e., a false discovery is claimed). Type-II errors are when H_0 is not rejected and false (i.e., a real signal is present but not claimed). The confidence level (CL) is the fraction of the time that type-I errors are avoided. The power of a test is the fraction of time that type-II errors are avoided.

There is inherently a tradeoff between CL and power. Reducing the false discovery rate also reduces rate that a real signal is not claimed. For a given CL, the power increases with the strength of the signal. Typically, a CL and power are chosen and the flux required to achieve them is an important characteristic of the analysis. A common value of the CL is a false discovery probability of 2.87×10^{-7} (i.e. 5σ if expressed as the one-sided tail of a Gaussian distribution), which is a stringent requirement in order to claim a discovery. A CL of 90% is often used for placing limits, or bounds, on physics parameters.

6.3 Calculating Significance and Discovery Potential

The significance of the analysis is defined in a purely frequentist manner (counting outcomes of simulated trials). In our case, we compare the TS from the real data with the distribution of TS from trials with events scrambled in R.A. (analogous to the null hypothesis). Since a higher TS indicates a larger deviation from the background-only expectation, we define the p-value as the fraction of randomized data sets with equal or higher test statistic values than the real data. The distributions of TS and the corresponding p-value (integral distribution) for 10 million trials are shown in figure 6.3 for a fixed point source at $\delta = 25°$. Also shown are distributions with simulated signal events injected following a spectrum $d\Phi/dE \propto E^{-2}$.

Note that, since we do not allow negative values of n_s, all under-fluctuations result in $TS = 0$, the lowest possible value. This yields a p-value of 100%, which happens in approximately half of the searches.

We calculate the discovery potential as the flux required for 50% of trials with simulated signal to yield a p-value less than 2.87×10^{-7} (i.e. 5σ significance if expressed as the one-sided tail of a Gaussian distribution). This flux is calculated by running random trials where fake signal events have been injected into the data set. The simulated events are selected from a neutrino simulation by a weighted random selection. An algorithm that efficiently samples over a large range of injected signal events was designed to find the Poisson mean number of events that results in the desired CL and power, and simulation is again used to translate this mean into a flux.

As seen in figure 6.3, a χ^2 distribution with 2 degrees of freedom can be used to estimate the TS and calculate the p-value. Wilks' theorem states that for very large data sets, TS will be asymptotically distributed as a χ^2 with degrees of freedom equal to the number of free parameters in the likelihood. In our case, we have two free parameters, the number of signal events and the spectrum. This approximation is convenient when running 10^7 or more simulation trials is computationally difficult. Our event statistics at high energy are quite low, reducing the effective degrees of freedom and making the approximation imperfect but usually conservative.

6.4 Calculating Upper Limits and Sensitivity

We follow the arguments of [105] in order to explain some of the benefits and short-comings of existing choices for calculating upper limits. For an experiment that measures some parameter x (such as our TS) with actual observed value x_0, we would

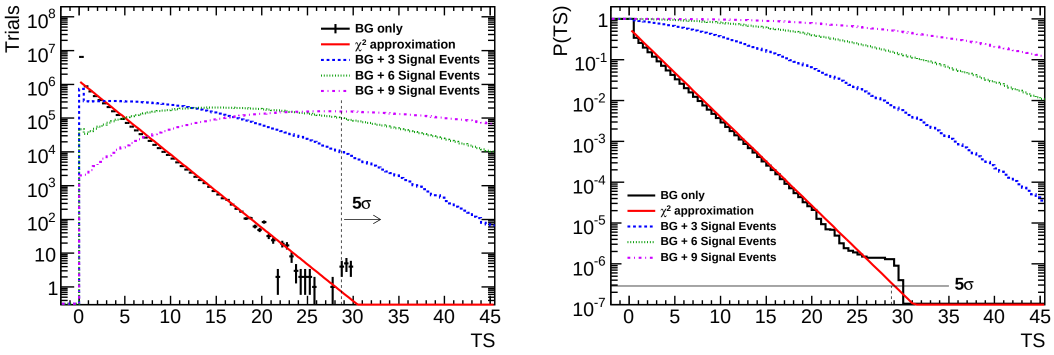

Figure 6.3: Distributions of the test statistic TS for a fixed point source at $\delta = 25°$ for 10 million scrambled data sets (left) and the p-value, or the probability to obtain TS or higher (right). A χ^2 distribution with 2 degrees of freedom times one-half (because we only search for excesses) can be used as an approximation. Also shown are the distributions when simulated signal events are injected following a spectrum $d\Phi/dE \propto E^{-2}$. About nine events are needed for a discovery in 50% of trials at this declination since the median TS in this case is 29.1.

like to infer information about a physical parameter ϕ (such as a flux) with true value ϕ_t. From simulations, we can determine $P(x|\phi)$. And from Bayes' theorem we could use that probability in order to infer something about our true parameter of interest:

$$P(\phi_t|x_0) = \frac{P(x_0|\phi_t)P(\phi_t)}{P(x_0)}. \tag{6.7}$$

A Bayesian interval at confidence level α could be constructed by requiring

$$\int_{\phi_1}^{\phi_2} P(\phi_t|x_0) d\phi_t = \alpha. \tag{6.8}$$

Unfortunately, this method requires us to know $P(\phi_t)$, the "prior" probability of ϕ_t, which is most often not known. As physicists, we always apply our own prior experience regarding how likely or unlikely a result is to decide how to interpret an experimental result. But this subjectivity is not desirable for reporting results. Attempts to remove this subjectivity by choosing a uniform prior did not yield mathematically consistent results. For more details, see [105].

Instead, we use a classical (or frequentist) confidence interval construction first proposed by Neyman [106] with the Feldman and Cousins (or likelihood ratio) ordering principle [105]. The goal is, for some parameter of interest ϕ, to create an interval $[\phi_1, \phi_2]$ such that

$$P(\phi \in [\phi_1, \phi_2]) = \alpha, \tag{6.9}$$

where α is equal to the CL, which we take to be 90%, and ϕ_1 and ϕ_2 are functions of some observable parameter x. Equation 6.9 refers to an ensemble of experiments with a fixed ϕ where each experiment results in its own observation of x and confidence intervals $[\phi_1, \phi_2]$. When eq. 6.9 is satisfied, the confidence intervals are said to have proper coverage. That is, ϕ will be contained within those confidence intervals in 90% of experiments. This is not equivalent to the Bayesian statement (eq. 6.8) that there is a 90% probability that ϕ_t is in the interval $[\phi_1,\phi_2]$.

To construct confidence intervals, we use a method called “confidence belts.” For each value of ϕ along a vertical axis, we use simulation to construct $P(x|\phi)$ along a horizontal axis. Then we select an interval $[x_1,\, x_2]$ such that

$$P(x \in [x_1, x_2]|\phi) = \alpha. \tag{6.10}$$

A range of values for x_1, x_2 pairs can satisfy eq. 6.10, and Neyman did not specify which to choose. The most common choice is to set a strict upper limit:

$$P(x < x_1|\phi) = 1 - \alpha. \tag{6.11}$$

Sometimes these are referred to as "Neyman upper limits," although any choice for x_1 and x_2 that satisfies eq. 6.10 should be considered a Neyman construction [105]. Another common choice is to calculate a central confidence interval:

$$P(x < x_1|\phi) = P(x > x_2|\phi) = (1 - \alpha)/2. \tag{6.12}$$

A problem with using eqs. 6.11 and 6.12 occurs when a decision of which to use is made after performing the experiment. It seems natural to publish only a strict upper limit when the null hypothesis is accepted, and only after a reasonable certainty of a signal to publish the central confidence interval that provides upper and lower bounds on the signal. But this course of action leads to substantial overcoverage.

We evaluate limits at 90% CL using the likelihood ratio ordering of Feldman and Cousins [105], which naturally maintains proper 90% coverage while producing upper limits for null results and two-sided confidence intervals for non-null results. To be more specific, we are interested in a Poisson mean number of events μ, which translates directly to a neutrino flux and can be associated with ϕ in the previous discussions. Our observable is TS, which is represented by x in the previous discussions. Precomputed confidence bands of Feldman and Cousins [105] are only for Poisson statistics, where the test statistic is from an integer number of events. In our case, the test statistic TS is continuous and we must construct our own confidence bands using a large amount of simulation.

To make the numerical limit calculation easier, we compress our test statistic to a new observable $D = \sqrt{TS}$ ($D = \mathrm{sign}(TS)\sqrt{|TS|}$ should be used if negative values are allowed). We simulate 10,000 trials of every integer number of signal events from 0 to 50, forming the vertical axis of a two-dimensional histogram with D on the horizontal axis. Simulation events from a weighted random selection of neutrino simulation, usually with $d\Phi/dE \propto E^{-2}$, are injected into data that have been scrambled in R.A. For a given mean signal strength, we calculate the probability of obtaining D as

$$P(D|\mu) = \sum_{i=0}^{50} \Big(P(D|i) \times P(i|\mu) \Big), \tag{6.13}$$

where $P(D|i)$ is the probability of obtaining D given i signal events, and $P(i|\mu)$ is the Poisson probability of getting i signal events for a Poisson mean μ. Note, we could directly construct a histogram of the μ versus D by injecting signal events according to a Poisson distribution, but the method of simulating a fixed number of events and reweighting the table is much more efficient. An example of the resulting histogram is shown in figure 6.4.

According to the Feldman and Cousins ordering principle, we rank each bin in the two-dimensional histogram by the ratio

$$R = \frac{P(D|\mu)}{P(D|\mu_{\mathrm{best}})}, \tag{6.14}$$

where $P(D|\mu_{\mathrm{best}})$ is the maximum value of $P(D|\mu)$ for bins with the same observable value D (vertical slices). For each collection of bins with the same μ (horizontal

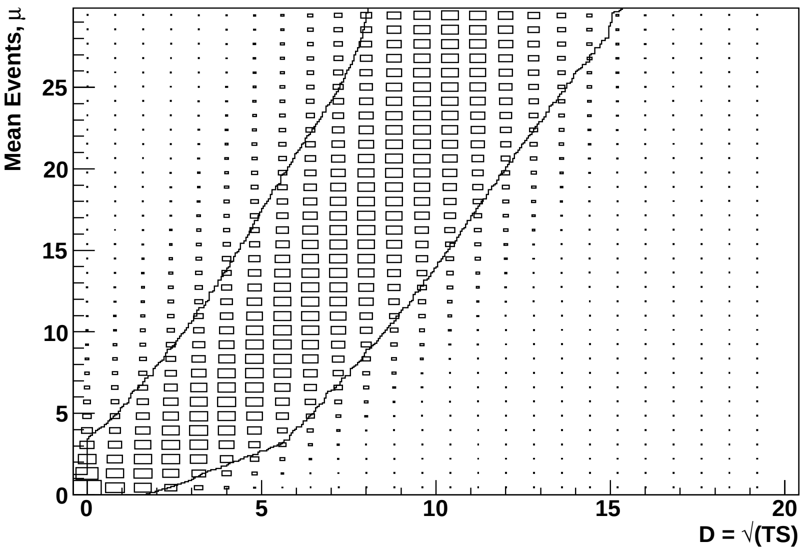

Figure 6.4: Feldman and Cousins 90% CL band for $\delta = 25°$. The boxes represent $P(D|\mu)$ and the solid black lines represent the upper and lower limits as a function of the observed value of D. For demonstration, the two-dimensional histogram has been binned much courser than that used to calculate the limits. From figure 6.3, the fixed source discovery threshold is $D = \sqrt{TS} \approx \sqrt{29.1} \approx 5.4$. With a Poisson mean of 9 events for discovery, the 90% CL limits are approximately 3 to 19 events.

slices), the acceptance interval starts with the highest-ranked bin. Bins are accepted from highest to lowest rank until the integral of $P(D|\mu)$ over the acceptance region in D reaches the desired CL, in our case 90%. As the original authors of the method suggest, the band coverage is increased until the coverage is monotonic in D. Now, the table of acceptance regions can be used to construct limits for any observed value D. The locations where a vertical line drawn at this value intersect the acceptance region form the 90% CL on μ. The highest and lowest values of μ are the 90% upper and lower limits, respectively, at 90% CL and can be translated to a flux using simulation. An example of these confidence bands is shown in figure 6.4.

We calculate the sensitivity of the analysis as the median upper limit with no signal events added. The median TS is determined using 10000 background-only trials, and is almost always 0 in our case (again, because under-fluctuations are assigned $TS = 0$). Although the sensitivity is the median upper limit, it is also almost always the best (lowest) upper limit under this construction.

6.4.1 Including Systematic Errors in Upper Limits

Specific systematic errors for IceCube are discussed later in chapter 8. These systematic uncertainties are incorporated into the upper limit and sensitivity calculations using the method of [107] with a modification by [108]. This method follows a hybrid Bayesian-frequentist prescription to construct confidence intervals. That is, the method follows the frequentist limit calculation of the previous section to find limits on μ (and hence the flux), but the unknown experimental signal efficiency ϵ_s is incorporated by integrating over a prior probability distribution $P(\epsilon_\mathrm{s}|\hat{\epsilon}_s, \sigma_{\epsilon_s})$, which describes our knowledge of the nuisance parameter ϵ_s. The prior probability is assumed to be described by a Gaussian of mean $\hat{\epsilon}_s$ and width σ_{ϵ_s}. In the case of our two-dimensional probability tables for calculating confidence belts, changing the efficiency is effectively the same as changing μ. Our PDFs become functions of the nuisance parameters:

$$P(D|\mu, P(\epsilon_\mathrm{s}|\hat{\epsilon}_s, \sigma_{\epsilon_s})) = \int_{\epsilon'_s} P(D|\mu, \epsilon'_s) P(\epsilon'_s|\hat{\epsilon}_s, \sigma_{\epsilon_s}) d\epsilon'_s. \tag{6.15}$$

Additionally, for the ordering principle, we need a modified likelihood ratio

$$R = \frac{\displaystyle\int_{\epsilon'_s} P(D|\mu, \epsilon'_s) P(\epsilon'_s|\hat{\epsilon}_s, \sigma_{\epsilon_s}) d\epsilon'_s}{P(D|\mu_\mathrm{best}, \hat{\epsilon}_s)}, \tag{6.16}$$

which was shown by [108] to give intuitive confidence intervals that increase in size with increasing systematic error. Equations 6.15 and 6.16 can then be used to construct classical confidence intervals, already described. Since the absolute efficiency is not relevant, we can use our simulation to represent the best guess for the case of $\hat{\epsilon}_s = 1$, and σ_{ϵ_s} is determined in chapter 8 using modified simulations. The integration is performed numerically.

Sometimes, a naive assumption is made that upper limits should scale linearly with the systematic error in an attempt to be conservative. However, the method presented here preserves proper coverage in the face of systematic errors, which may increase or decrease your signal.

6.5 Measuring Spectral Index and Cutoff Spectra

The likelihood analysis is not only more sensitive than binned methods, but it can also help extract astrophysical information. Figure 6.5 shows our ability to reconstruct the spectral index for power law neutrino sources at a declination of 6°. The effective area is high for a broad range of energies here, and the spectral resolution is best. For each spectrum shown, the statistical uncertainty (1σ CL) in the spectral index will be about ± 0.3 when enough events are present to claim a discovery. Spectral resolution worsens for sources farther from the horizon, to ± 0.4 at both $\delta = -45°$ and $\delta = 45°$ when enough events are present for a discovery in each case.

Although E^{-2} sensitivities and limits have become a useful benchmark for comparing performance, cutoffs in the energy spectrum over a wide range of energy are possible. To understand the ability of the method to detect sources with cutoff spectra, figure 6.6 shows the discovery potentials for a wide range of exponential cutoffs. Typ-

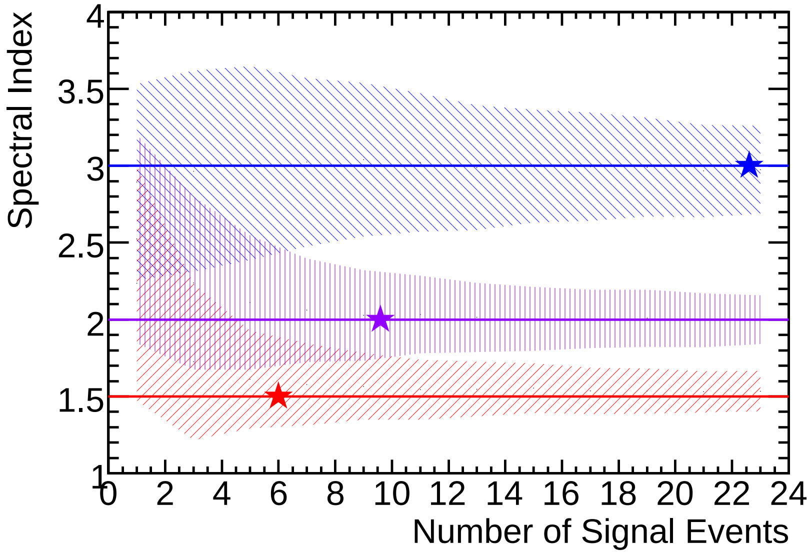

Figure 6.5: Reconstructed spectral index (1σ shaded area) versus the number of signal events injected for three source spectra: $E^{-1.5}$, E^{-2}, and E^{-3}. The sources are pure power-laws at a declination of 6°. The stars mark the number of events required on average for a 5σ discovery for each spectrum. Systematic errors are not included.

ically, cutoffs observed in gamma rays are in the range 1–10 TeV for galactic sources. The likelihood fit is still performed using a pure power law. The method could be modified to include the cutoff energy as an additional free parameter. This is likely unimportant for discovery since meaningful constraints on additional free parameters will only come with larger numbers of signal events.

6.6 Modification for Stacking Sources

Stacking multiple sources in neutrino astronomy has been an effective way to enhance discovery potential and further constrain astrophysical models [35, 109]. We can consider the accumulated signal from a collection of sources using a method similar

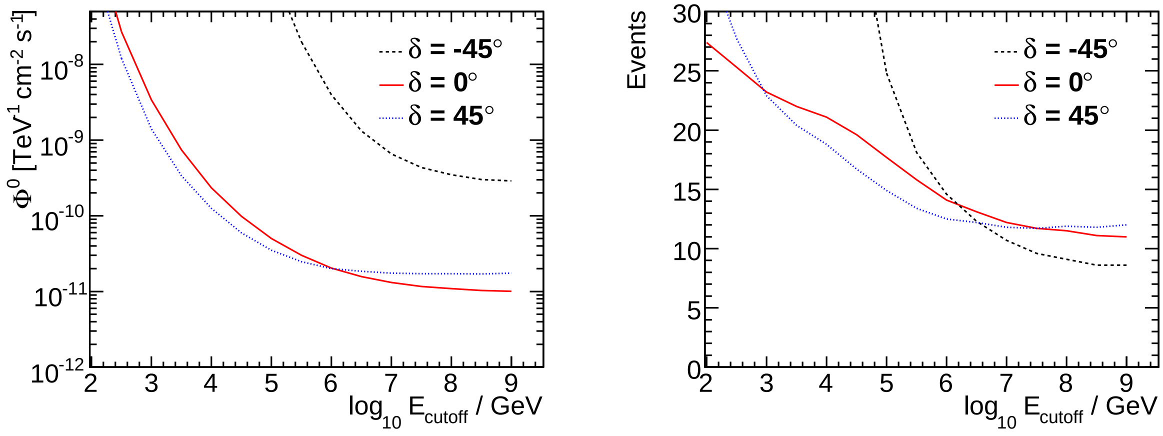

Figure 6.6: The discovery potential versus an exponential cutoff is shown for a flux parameterized as $dN/dE = \Phi^0 \cdot (E/\mathrm{TeV})^{-2}\exp(-E/E_{\mathrm{cutoff}})$. The discovery potential is given as the flux normalization Φ^0 (left) and the number of events at the final level (right). Curves are shown at three representative declinations. The likelihood fit is still performed using a pure power law.

to [110]. Only a modification to the signal likelihood is necessary in order to stack sources, breaking the signal hypothesis into the sum over M sources:

$$\mathcal{S}_i \Rightarrow \mathcal{S}_i^{tot} = \frac{\sum_{j=1}^{M} W^j R^j(\gamma) \mathcal{S}_i^j}{\sum_{j=1}^{M} W^j R^j(\gamma)}, \tag{6.17}$$

where W^j is the relative theoretical weight, $R^j(\gamma)$ is the relative detector acceptance for a source with spectral index γ (assumed to be the same for all stacked sources), and $\mathcal{S}_i^j$ is the signal probability density for the ith event, all for the jth source. As before, the total signal events n_s and collective spectral index γ are fit parameters. The W^j coefficients depend on our prior theoretical assumptions about the expected neutrino luminosity. They are higher for sources that are, on theoretical grounds, expected to be brighter. Tables for $R^j(\gamma)$, given as the mean number of events from a source with $dN/dE \propto E^{-\gamma}$, are calculated using simulation. The flexibility built into the method by the relative detector acceptance and theoretical weights allows us to use source catalogs covering the whole sky and with large variations in source strengths, as well as to directly test model predictions. The improvement in discovery potential from stacking sources is illustrated in figure 6.7, showing the discovery potential flux versus the number of sources stacked. All sources are at the same declination in this example. The sensitivity is expected to scale with the square-root of the number of sources for high statistics. The improvement shown here is better because we have a relatively low number of events. In the limit of a zero background experiment, sensitivity scales linearly.

6.7 Modification for Extended Sources

We would also like to consider sources that are spatially extended (with respect to the PSF). For an example of how important this can be, the significance observed by the Milagro experiment in the location of the Fermi source J0634.0+1745 (associated with the Geminga pulsar) rises from 3.5σ to 6.3σ by fitting for an extended source [33].

Since our source hypothesis is no longer a delta function but has a spread of its own, we only need one modification to again create a PDF for how our events distribute spatially. We now convolve the source distribution with the point spread function of the detector. Since we model our point spread function as a circular two-dimensional Gaussian distribution, it is easy to also model a source as a circular two-dimensional Gaussian of width σ_s. The convolution results in a broader two-dimensional Gaussian

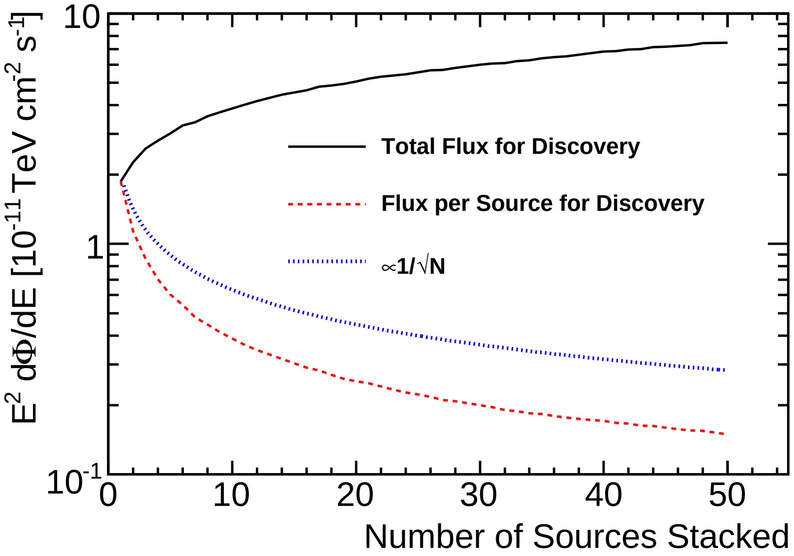

Figure 6.7: Discovery potential flux versus the number of stacked sources, all with an equal E^{-2} flux and (for example purposes) at a fixed declination of 45°. Although the total flux required increases as more sources are added, owing to a higher effective background, the flux per source required can be substantially reduced.

of width $\sqrt{\sigma_i^2 + \sigma_\mathrm{s}^2}$ and the likelihood uses this distribution for the signal spatial term. The discovery potential flux for a range of source extensions is shown in figure 6.8 and compared to the (incorrect) hypothesis of a point source. For a source with true extent $\sigma_s = 2°$, the point-source hypothesis requires nearly a factor of 2 times more flux for discovery compared to the correct extended-source hypothesis.

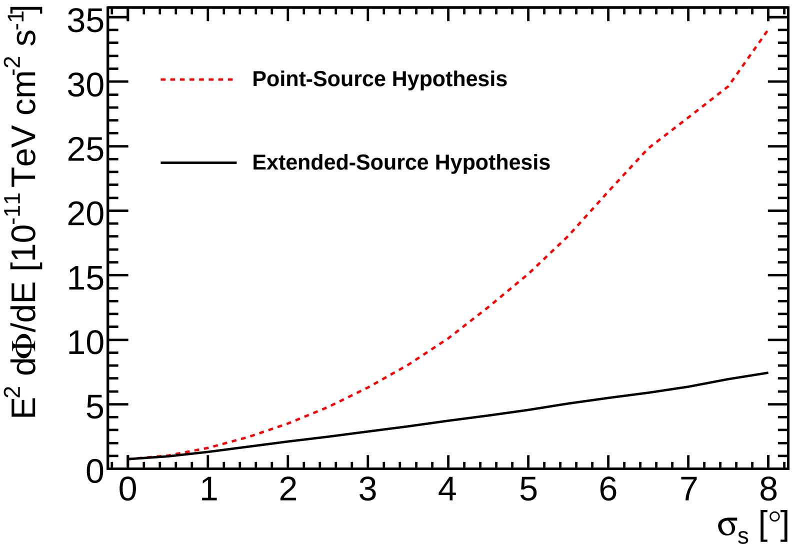

Figure 6.8: Discovery potential flux versus the σ_s of an extended source (distributed as a two-dimensional Gaussian) with an E^{-2} spectrum at a declination of 25°. The case of a point-source hypothesis is compared against the correct extended-source hypothesis matching what was used to simulate the signal.

Chapter 7

Searches for Neutrino Sources

Five different searches are proposed, based on the maximum likelihood anlaysis technique. They are listed and the scientific motivation for each explained in this chapter.

We perform five searches:

1. a scan for the most significant point source in the entire sky;
2. a search over an a priori defined list of 39 interesting astrophysical objects;
3. a stacking search for 16 Milagro TeV gamma ray sources, some seen only in coincidence with the Fermi-LAT, and one unconfirmed hot spot (17 total sources);
4. a stacking search for 127 local starburst galaxies [111];
5. a stacking search for five nearby clusters of galaxies (CGs), testing four different models for the CR spatial distribution [112].

The analyses and event selection procedure were determined before unblinding the R.A. of the data. We require a 5σ significance for discovery. The current policy of the IceCube Collaboration is to calculate final p-values are calculated for each search individually. Although there are several trials, the high threshold for significance keeps the false discovery rate well controlled for the time being.

7.1 All-sky Scan

The first search is a scan for the single most significant point source of neutrinos over the declination range -85° to $+85^\circ$. The maximum likelihood ratio is defined continuously over the sky, and we sample it on a grid of 0.1° in R.A. and 0.1° in decl. The size of the grid is not important as long as it is small compared to the angular resolution of the detector. Using a finer grid increases the computation time with no added benefit. A grid size that is comparable to or larger than the angular resolution could miss the location of the peaks in the significance map, yielding sub-optimal performance.

7.2 A Priori Source List

In order to avoid the large number of effective trials associated with scanning the entire sky, we also perform a search for the most significant of 39 a priori selected source candidates, given in Table 9.1. These sources have been selected on the basis of observations in gamma rays or astrophysical modeling that predicts neutrino emission. We also added the most significant location observed in the 22-string IceCube configuration (a post-trial p-value of 1.3%; [81]).

7.3 Milagro TeV Source Stacking

The Milagro Collaboration has reported 16 sources of TeV gamma rays [32], several only after correlating with GeV gamma rays from the Fermi Gamma-ray Space

Telescope source list [33]. These sources are promising candidates for detection by neutrino telescopes. Particularly interesting are sources in the complex Cygnus region [113] and six SNR associations [31, 114], including MGRO J1852+01, a hot spot that falls below the significance threshold of the Milagro Collaboration to be claimed as a source. If confirmed as a source, MGRO J1852+01 could contribute a large fraction (about 42%) of the total neutrino flux from the SNR sources [31]. For the 40-string configuration of IceCube, the model of [31] predicts 3.0 neutrino events in 375.5 days, following a spectrum $d\Phi/dE \propto E^{-2.1}$ with an exponential cutoff at about 600 TeV.

We performed a stacking search for 17 sources observed in TeV gamma rays by Milagro (adding MGRO J1852+01 to the 16 sources which were found significant by the Milagro Collaboration) using an equal weight for each source in the likelihood. Assuming that neutrino and gamma ray fluxes correlate and using these as weights in the likelihood did not appreciably improve the sensitivity in this case. Spatial extensions were used in the search for three of the sources where measurements were given (also used in the source simulation for limit calculations). The largest source was MGRO J2031+41, reported to have a diameter of $3.0° \pm 0.9°$ [32].

7.4 Starburst Galaxy Stacking

Starburst galaxies have a dense interstellar medium and high star formation rates. This leads to both high supernova rates and heating of ambient dust. The model of [111] associates the far-infrared (FIR) emission with this hot dust and the radio emission with synchrotron losses of CR electrons, presumably accelerated along with hadronic CRs in the elevated number of SNRs. The observed strong correlation between the FIR and radio emission points to the high star formation rate as the single underlying cause, and should also correlate with the neutrino flux. The increased production of CRs and high density of target material are ideal conditions for neutrino production. The starburst galaxies M82 and NGC 253 have been observed in gamma rays at GeV–TeV energies [115, 116, 117] and are the only observed steady extragalactic TeV gamma ray sources not associated with AGNs.

We performed a stacking search for 127 starburst galaxies, weighting the sources by their observed FIR flux at 60 μm, as compiled in Table A.1 in [111].

7.5 Galaxy Cluster Stacking

CGs are another potential source of high energy protons and, through interactions with intracluster material (ICM), neutrinos. CGs are the largest gravitationally bound objects in the universe and continue to grow through merging and accretion of dark matter and baryonic gas, generating shock fronts on megaparsec scales. The possibility for CGs to be sources of ultra high energy CRs above 3×10^{18} eV is described in, e.g., [118] and [119]. [112] discuss the possibility of CGs being a significant contribution to the CR spectrum between the second knee at about 3×10^{17} eV and the ankle at about 3×10^{18} eV. They give predictions for neutrinos from five nearby ($z < 0.03$) CGs: Virgo, Centaurus, Perseus, Coma, and Ophiuchus. Information on location, distance, and size of CGs (virial radii) was taken from [120]. These nearby CGs appear to us as spatially extended objects with virial radii subtending 1.3°–6.9°, so an extended spatial distribution of neutrinos is possible. Whereas the distribution of the ICM is well known from X-ray observations [121], the distribution of CRs is highly uncertain. The distribution of neutrinos is given by the product of the CR and ICM distributions. Four CR models have been considered for neutrino production, discussed in [112] and references therein (e.g., [122, 123]):

- **Model A:** CRs are uniformly distributed within the cluster shock radius, taken to be 0.56 of the virial radius for the dynamical parameters considered.
- **Model B:** CRs are uniformly distributed within the virial radius, yielding the most conservative neutrino flux distributed over the largest area.
- **Isobaric:** CRs follow the distribution of thermal gas.
- **Central AGN:** In a two-step acceleration scenario CRs are accelerated in the central AGN up to a maximum energy before diffusing throughout the cluster and possibly undergoing further acceleration. For the purposes of IceCube searches, this model can be treated as a point source. This model is discussed in detail by [124].

Signal neutrinos were simulated according to each of the four models. We modeled the source extensions in the likelihood as two-dimensional Gaussian distributions with the width for each source and each model determined by optimizing for the best discovery potential. Although the modeling of the source extension as a Gaussian in the likelihood is not ideal, it is straightforward and computationally fast. The exact shape of the sources is not important for small signals; we may be able to analyze the shape with more detail depending on the intensity of any signal.

We performed a stacking search for five nearby CGs mentioned above following the model predictions of [112] as weights in the likelihood. The size of the clusters in the likelihood fit was allowed to vary discretely between the optimal widths for each CR distribution model. The optimal width and ν_μ differential flux for each source and

Table 7.1. Galaxy cluster parameters.

Source	R.A. (°)	Decl. (°)	Model	σ_s (°)	A (TeV^{-1} cm^{-2} s^{-1})	γ_1	γ_2	E_{break} (TeV)
Virgo	186.63	12.72	Model A	2.0	1.42×10^{-12}	-2.14	-4.03	2.16×10^{6}
			Model B	4.0	1.18×10^{-12}	-2.14	-4.03	2.16×10^{6}
			Isobaric	3.0	7.57×10^{-13}	-2.14	-4.03	2.16×10^{6}
			Central AGN	0.0	6.47×10^{-12}	-2.42	-4.24	2.13×10^{6}
Centaurus	192.20	-41.31	Model A	0.25	2.78×10^{-13}	-2.14	-4.03	2.15×10^{6}
			Model B	0.5	2.20×10^{-13}	-2.14	-4.03	2.15×10^{6}
			Isobaric	0.25	1.09×10^{-13}	-2.15	-4.07	2.33×10^{6}
			Central AGN	0.0	5.10×10^{-13}	-2.45	-4.28	2.39×10^{6}
Perseus	49.95	41.52	Model A	0.0	5.83×10^{-14}	-2.15	-4.07	2.32×10^{6}
			Model B	0.5	4.60×10^{-14}	-2.15	-4.07	2.32×10^{6}
			Isobaric	0.0	6.17×10^{-13}	-2.15	-4.07	2.32×10^{6}
			Central AGN	0.0	5.97×10^{-13}	-2.40	-4.20	1.88×10^{6}
Coma	194.95	27.94	Model A	0.25	2.14×10^{-14}	-2.14	-4.03	2.12×10^{6}
			Model B	0.25	1.34×10^{-14}	-2.14	-4.03	2.12×10^{6}
			Isobaric	0.25	1.83×10^{-13}	-2.15	-4.07	2.30×10^{6}
			Central AGN	0.0	2.13×10^{-13}	-2.41	-4.20	1.89×10^{6}
Ophiuchus	258.11	-23.36	Model A	0.0	4.87×10^{-14}	-2.15	-4.07	2.29×10^{6}
			Model B	0.5	1.50×10^{-14}	-2.15	-4.07	2.29×10^{6}
			Isobaric	0.0	5.50×10^{-13}	-2.15	-4.11	2.49×10^{6}
			Central AGN	0.0	2.55×10^{-13}	-2.43	-4.24	2.12×10^{6}

Note. — σ_s is the optimized sigma of a two-dimensional Gaussian distribution used in the likelihood. Numerical calculations of the differential fluxes [125] for each model described in [112] are fit well to broken power laws, parameterized in Eq. 7.1.

each model are given in Table 7.1. The differential fluxes are parametrized as broken power laws:

$$\frac{d\Phi}{dE}\ (\text{TeV}^{-1}\text{cm}^{-2}\text{s}^{-1}) = \begin{cases} A \cdot (E/\text{TeV})^{-\gamma_1} & E \leq E_{\text{break}}, \\ B \cdot (E/\text{TeV})^{-\gamma_2} & E > E_{\text{break}}. \end{cases} \tag{7.1}$$

The parameter $B = A \cdot E_{\text{break}}^{\gamma_2 - \gamma_1}$ after enforcing continuity at the break energy.

Chapter 8

Systematic Errors

This chapter outlines the main sources of systematic uncertainties in the search for point sources of neutrinos. The predominant factors are our understanding of the optical properties in the ice, the absolute calibration of the digital optical modules, and uncertainties in the physics of the muon energy losses in ice and the neutrino cross section.

The analyses described in chapter 7 give reliable statistical results (p-values) due to the ability to generate background-only data sets by scrambling the data in R.A. This is similar to the technique of using an on-source and an off-source region. By using the data to estimate background, the systematic errors come only from signal and detector simulation used to calculate flux upper limits. The main systematic uncertainties on the flux limits come from photon propagation in ice, absolute DOM sensitivity, and uncertainties in the Earth density profile as well as muon energy loss. All numbers considered in this section are for a spectrum $d\Phi/dE \propto E^{-2}$ of muon neutrinos.

- **Ice properties**: We evaluate the systematic uncertainty due to photon propagation by performing dedicated signal simulations with scattering and absorption coefficients varied within their fit uncertainties of ±10% [72]. The maximum difference was between the case where both scattering and absorption were increased by 10% and the case where both were decreased by 10%. The deviation in the observed number of events between these two cases was 11%.

- **DOM sensitivity**: The range of uncertainty in the DOM sensitivity is taken as ±8%, based on the measured uncertainty in the PMT sensitivity [68]. Although the measurements are only on the bare PMT without the DOM casing and mu metal shielding, these are thought to be a negligible contribution to the error. Another dedicated simulation was performed where we varied the DOM sensitivity inside this uncertainty. The deviation in the observed number of events between the extreme cases was 9%. These first two sources of uncertainty on the flux varied by only about 2% between the northern and southern sky, so only averages over the whole sky are reported.
- **Neutrino-nucleon cross-section and muon energy loss**: Uncertainties in muon energy losses, the neutrino-nucleon cross-section, and the rock density near the detector introduce an 8% systematic uncertainty for vertically up-going events [126]. Vertically up-going events are the most affected, and this uncertainty is applied to all zeniths to be conservative.

These main sources of error are summarized in Table 8.1. A sum in quadrature of the systematic uncertainties on the signal efficiency gives a total of 16% systematic uncertainty in the signal simulation. These systematic uncertainties are incorporated into the upper limit and sensitivity calculations using the method of [107] with a modification by [108] and discussed in section 6.4.1. The value of σ_{ϵ_s}, the width of a

Table 8.1. Summary of systematic errors for E^{-2} neutrino sources.

Error source	Source error	Resulting error in signal efficiency
Ice properties	10%	11%
DOM sensitivity	8%	9%
Cross sections, E-loss	8%	8%
Sum in quadrature		16%

Gaussian describing the prior probability of the signal efficiency in eq. 6.15, is taken to be 16%. Since our flux upper limits typically correspond to only a few signal events (3–4), the statistical uncertainty on the signal is generally much larger than this systematic uncertainty. Indeed, the limits only increase by about 3% on average after including these systematic errors.

Chapter 9

Results

This chapter covers the results of the five searches proposed in chapter 7. These results come in the form of p-values and upper limits (since no significant deviations from background are observed).

9.1 All-sky Scan

The results of the all-sky scan are shown in the map of the pre-trial p-values in figure 9.1. The most significant deviation from background is located at 113.75° R.A., 15.15° dec. The best-fit parameters are $n_s = 11.0$ signal events above background, with spectral index $\gamma = 2.1$. Since the best fit spectral index is substantially less than the expectation from background, much of the significance comes from the higher energies of the associated events. The pre-trial estimated p-value of the maximum log likelihood ratio at this location is 5.2×10^{-6}. In trials using data sets scrambled in R.A., 1,817 out of 10,000 have an equal or higher significance somewhere in the sky, resulting in the post-trial p-value of 18%. Upper limits for a flux $d\Phi/dE \propto E^{-2}$ of $\nu_\mu + \bar{\nu}_\mu$ are presented in figure 9.2. In all cases, an equal flux of neutrinos and anti-neutrinos is assumed.

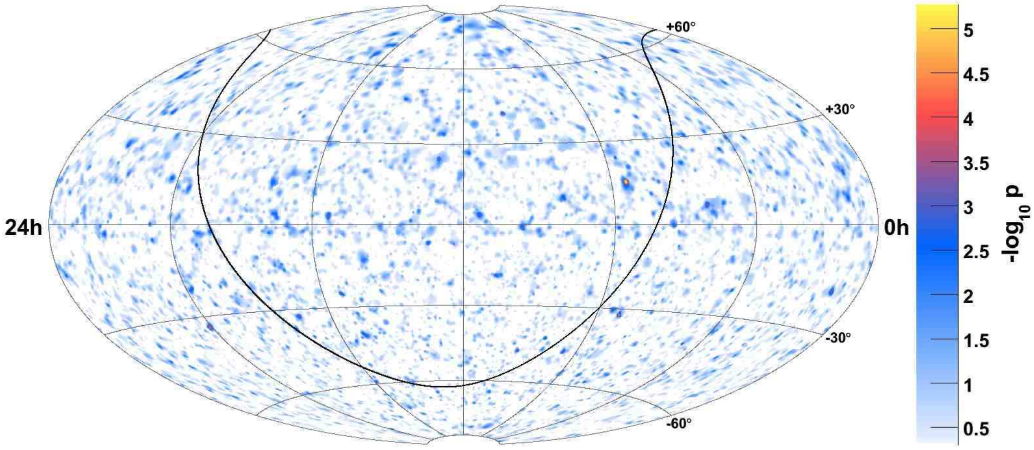

Figure 9.1: Equatorial skymap (J2000) of pre-trial significances (p-value) of the all-sky point source scan. The galactic plane is shown as the solid black curve.

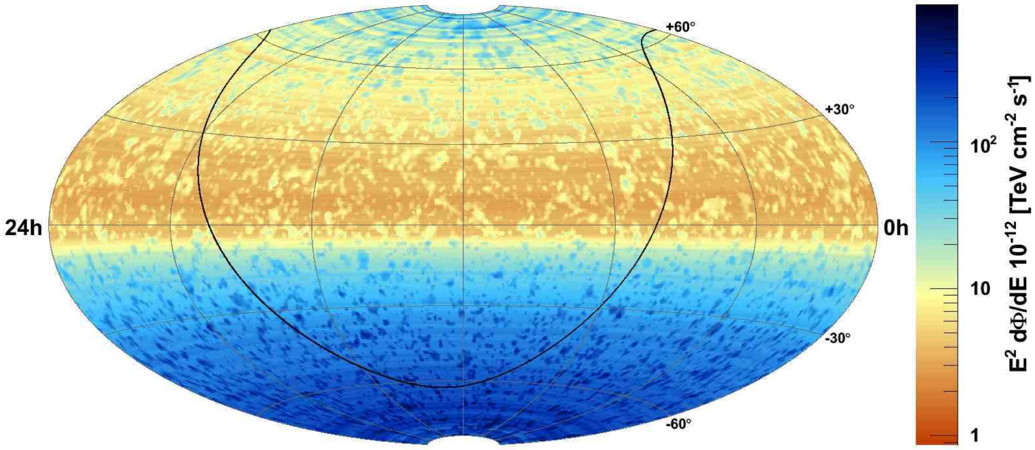

Figure 9.2: Equatorial skymap (J2000) of upper limits of Feldman-Cousins 90% confidence intervals for a flux $\Phi/dE \propto E^{-2}$ of $\nu_\mu + \bar{\nu}_\mu$. The galactic plane is shown as the solid black curve.

9.2 A Priori Source List

The results of the point-source search in the direction of 39 source candidates selected a priori are given in Table 9.1 and also shown in figure 9.3 with the IceCube median sensitivity. Since the fit was restricted to physical signal values $n_s \geq 0$, approximately half of the results have $n_s = 0$ exactly, corresponding to p-values equal to 100% and upper limits equal to the median upper limit (i.e. the sensitivity). The most significant source on the list was PKS 1622-297 with a pre-trial estimated p-value of 5%. The post-trial p-value of 62% was again determined as the fraction of scrambled data sets with at least one source with an equal or higher significance. The mean number of events at the final cut level required for the discovery of a point source is also shown in figure 9.4, along with the average background in a circular bin with 1° radius. Included in figure 9.3 is a preliminary comparison to the ANTARES experiment [127]. ANTARES is primarily sensitive to GeV–TeV energy neutrinos in the southern sky, so the coverage in energy is quite complementary to this IceCube analysis.

Table 9.1. Results for the *a priori* source candidate list.

Object	R.A. [°]	dec. [°]	$\Phi^{90}_{\nu_\mu}$	$\Phi^{90}_{\nu_\mu+\nu_\tau}$	p-value	n$_s$	γ	N_{1°	B_{1°
Cyg OB2	308.08	41.51	6.04	10.54	1.00	0.0	–	2	1.8
MGRO J2019+37	305.22	36.83	7.50	13.3	0.44	1.0	2.8	2	1.9
MGRO J1908+06	286.98	6.27	3.73	6.82	0.43	1.5	3.9	4	3.1
Cas A	350.85	58.81	9.04	15.92	1.00	0.0	–	1	1.8
IC443	94.18	22.53	3.80	6.62	1.00	0.0	–	1	2.0
Geminga	98.48	17.77	3.91	6.66	0.48	0.7	2.1	1	2.3
Crab Nebula	83.63	22.01	3.70	6.58	1.00	0.0	–	1	2.0
1ES 1959+650	300.00	65.15	10.74	19.18	1.00	0.0	–	0	2.0
1ES 2344+514	356.77	51.70	7.24	12.96	1.00	0.0	–	0	1.8
3C66A	35.67	43.04	10.89	19.70	0.24	3.4	3.9	3	1.9
H 1426+428	217.14	42.67	6.14	10.94	1.00	0.0	–	3	1.8
BL Lac	330.68	42.28	10.80	18.70	0.25	2.6	3.9	3	1.8
Mrk 501	253.47	39.76	8.11	14.14	0.41	1.3	3.9	3	2.0
Mrk 421	166.11	38.21	11.71	20.14	0.15	2.6	1.9	2	2.0
W Comae	185.38	28.23	4.46	8.06	1.00	0.0	–	0	1.9
1ES 0229+200	38.20	20.29	6.89	12.06	0.19	4.0	2.8	4	2.1

Table 9.1 (cont'd)

Object	R.A. [°]	dec. [°]	$\Phi^{90}_{\nu_\mu}$	$\Phi^{90}_{\nu_\mu+\nu_\tau}$	p-value	n$_s$	γ	N_{1°	B_{1°
M87	187.71	12.39	3.42	5.98	1.00	0.0	–	2	2.5
S5 0716+71	110.47	71.34	13.28	23.56	1.00	0.0	–	0	1.6
M82	148.97	69.68	19.14	32.84	0.40	2.0	3.9	4	1.8
3C 123.0	69.27	29.67	5.59	10.66	0.44	1.3	2.7	1	1.9
3C 454.3	343.49	16.15	3.42	5.92	1.00	0.0	–	1	2.3
4C 38.41	248.81	38.13	6.77	11.86	0.48	0.9	3.9	2	2.0
PKS 0235+164	39.66	16.62	6.77	11.62	0.15	5.3	3.0	5	2.3
PKS 0528+134	82.73	13.53	3.63	6.72	1.00	0.0	–	2	2.4
PKS 1502+106	226.10	10.49	3.26	5.78	1.00	0.0	–	0	2.5
3C 273	187.28	2.05	3.61	6.54	1.00	0.0	–	3	3.4
NGC 1275	49.95	41.51	6.04	10.54	1.00	0.0	–	2	1.8
Cyg A	299.87	40.73	7.84	13.44	0.46	1.0	3.5	3	1.9
IC-22 maximum	153.38	11.38	3.26	5.86	1.00	0.0	–	1	2.5
Sgr A*	266.42	-29.01	80.56	139.26	0.41	1.1	2.7	4	3.3
PKS 0537-441	84.71	-44.09	113.90	201.82	1.00	0.0	–	3	3.5
Cen A	201.37	-43.02	109.51	191.56	1.00	0.0	–	4	3.5

Table 9.1 (cont'd)

Object	R.A. [°]	dec. [°]	$\Phi^{90}_{\nu_\mu}$	$\Phi^{90}_{\nu_\mu+\nu_\tau}$	p-value	n$_s$	γ	N_{1°	B_{1°
PKS 1454-354	224.36	-35.65	92.56	156.74	1.00	0.0	–	4	3.5
PKS 2155-304	329.72	-30.23	105.41	182.90	0.28	1.7	3.9	3	3.4
PKS 1622-297	246.53	-29.86	152.28	263.86	0.048	3.0	2.6	4	3.3
QSO 1730-130	263.26	-13.08	24.83	43.30	1.00	0.0	–	4	3.5
PKS 1406-076	212.24	-7.87	16.04	28.72	0.42	1.3	2.3	4	3.3
QSO 2022-077	306.42	-7.64	12.18	21.78	1.00	0.0	–	2	3.3
3C279	194.05	-5.79	11.94	21.36	0.33	3.6	3.0	7	3.5

Note. — $\Phi^{90}_{\nu_\mu}$ and $\Phi^{90}_{\nu_\mu+\nu_\tau}$ are the upper limits of the Feldman-Cousins 90% confidence intervals for a $d\Phi/dE \propto E^{-2}$ flux normalization of ν_μ and $\nu_\mu + \nu_\tau$, respectively, in units of 10^{-12} TeV^{-1}cm^{-2}s^{-1} (i.e. $d\Phi/dE \leq \Phi^{90} \cdot (E/\mathrm{TeV})^{-2}$). n_s is the best-fit number of signal events. The (pre-trial) p-value is given. The spectral index γ is given when $n_s > 0$. N_{1° is the actual number of events observed in a bin of radius 1°. The background event density at the source declination is indicated by the mean number of background events B_{1° expected in a bin of radius 1°.

9.3 Stacking Searches

The Milagro TeV source stacking search resulted in a final p-value of 32% with best fit $n_s = 7.6$ (total number of signal events above background) and spectral index $\gamma = 2.6$. The starburst galaxy stacking search resulted in an under-fluctuation with best fit $n_s = 0$ and a final p-value of 100%, since we do not allow negative values of n_s. Finally, the CGs stacking search yielded a final p-value of 78% with $n_s = 1.8$. These results, along with sensitivities and upper limits, are summarized in Table 9.2.

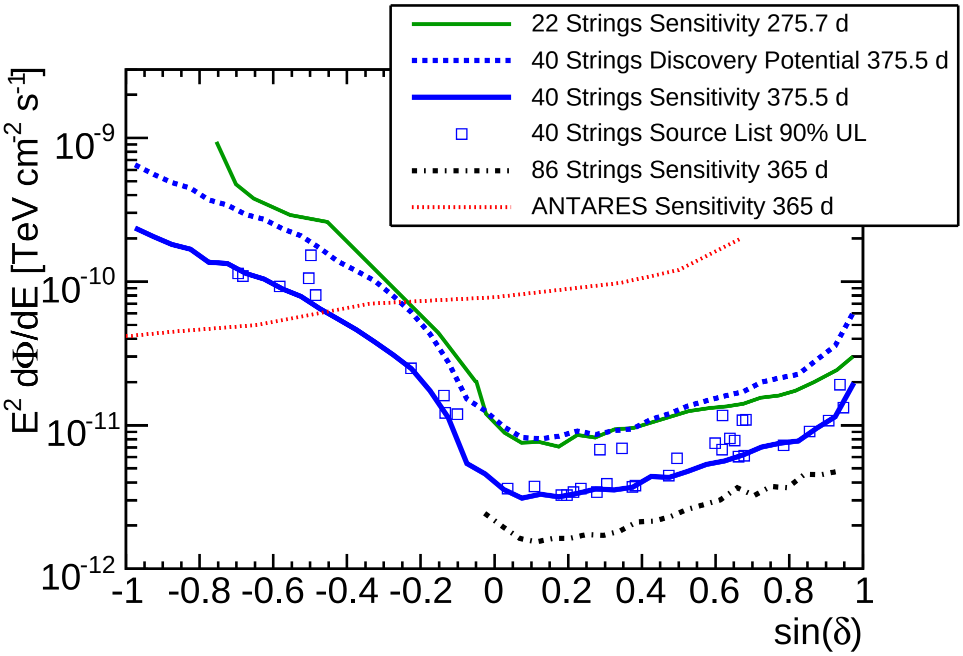

Figure 9.3: Median sensitivity to a point-source flux $d\Phi/dE \propto E^{-2}$ of $\nu_\mu + \bar{\nu}_\mu$ as a function of declination, shown for the 22-string IceCube southern and northern sky analyses [83, 81], this 40-string analysis, and preliminary estimated sensitivities for 1 year for the ANTARES experiment, primarily sensitive in the GeV–TeV energy range, [127] and the final IceCube configuration (using the event selection based on this work for the up-going region). For the a priori source list, upper limits of Feldman-Cousins 90% confidence intervals for a flux $d\Phi/dE \propto E^{-2}$ of $\nu_\mu + \bar{\nu}_\mu$ are shown. In addition, we show the discovery potential for this work.

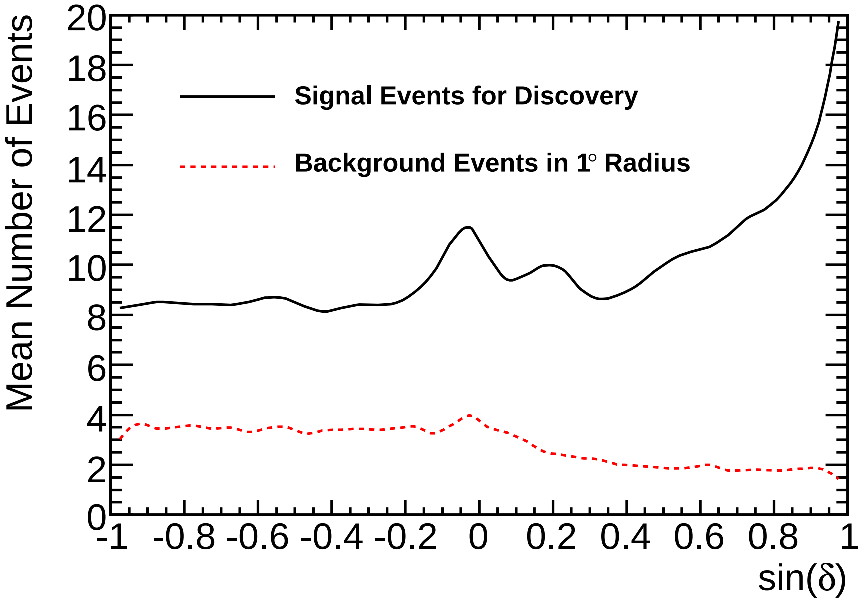

Figure 9.4: Mean number of $d\Phi/dE \propto E^{-2}$ signal events at the final cut level required for a discovery at 5σ in 50% of trials and the mean number of background events in a circular bin with a radius of 1° versus sine of the declination.

Table 9.2. Results for the stacked source searches.

Catalog	N Sources	Model	p-value	ν_μ Sensitivity	ν_μ Upper Limit	$\nu_\mu + \nu_\tau$ Sensitivity	$\nu_\mu + \nu_\tau$ Upper Limit
Milagro Sources	17	E^{-2}, Uniform	0.32	$\Phi^{90} = 9.0$	$\Phi^{90} = 12.3$	$\Phi^{90} = 15.8$	$\Phi^{90} = 24.5$
	6	6 SNR Assoc.[a]	[c]			SF = 2.9	SF = 7.2
Starburst Galaxies	127	$E^{-2}, \propto$ FIR Flux	1.0	$\Phi^{90} = 33.1$	$\Phi^{90} = 33.1$	$\Phi^{90} = 58.6$	$\Phi^{90} = 58.6$
Clusters of Galaxies	5	Model A[b]	0.78			SF = 8.4	SF = 7.8
		Model B[b]				SF = 14.4	SF = 12.0
		Isobaric[b]				SF = 13.2	SF = 13.2
		Central AGN[b]				SF = 6.0	SF = 6.0

Note. — Median sensitivities and upper limits at 90% CL for ν_μ and $\nu_\mu + \nu_\tau$ fluxes are given in two ways: as Φ^{90} for a spectrum $d\Phi/dE \propto E^{-2}$, i.e. the total flux from all sources $d\Phi/dE \leq \Phi^{90}\, 10^{-12}$ $\text{TeV}^{-1}\text{cm}^{-2}\text{s}^{-1}(E/\text{TeV})^{-2}$, or as a scaling factor (SF) relative to the models given in the footnotes. For example, if the Central AGN model flux normalization were 6.0 times higher, we would rule it out at 90% CL. All models predict equal fluxes of tau and muon neutrinos.

[a] [31]

[b] [112], see Table 7.1

[c] We did not calculate an a priori p-value for just the six SNR associations discussed in [31], since they are included in the search over all Milagro sources. However, some of these sources were the most significant on the list. Analyzed as a single subgroup, an a posteriori p-value of 0.02 was found with best fit parameters $n_s = 15.2$ and $\gamma = 2.9$. The true trial factor is incalculable since this was done after unblinding, but these remain sources of interest for future searches.

Chapter 10

Implications for Models of Astrophysical Neutrino Emission

This chapter surveys the existing literature for models of astrophysical neutrino emission. Upper limits are calculated for these models. In the case of the Crab Nebula, some of the most optimistic predictions are ruled out at more than 90% CL.

The IceCube Neutrino Observatory aims to further our understanding of astrophysical phenomena, constraining models even in the absence of a detection. Figure 10.1 shows our sensitivity to some specific predictions.

10.1 SNR RX J1713.7-3946

The model of [128] is for SNR RX J1713.7-3946. This analysis is not very sensitive to spectra which cut off below 100 TeV in the southern sky, where RX J1713.7-3946 is located. Applying this emission model at the location of the Crab Nebula ($\delta = 22.01°$), we obtain an upper limit that rules out a flux 3.2 times higher than the prediction and discovery would require 13.0 times more flux.

10.2 SNR MGRO J1852+01

The Milagro hot spot MGRO J1852+01 is the brightest source of six SNR associations considered in [31]. The stacking results were already shown in Table 9.2. Our upper limit for just this one brightest source is a factor of 7.9 away from excluding this model at 90% CL and a factor of 12.3 from discovery. The best fit for MGRO J1852+01 is to 7.0 events with $\gamma = 2.9$, which increases the upper limit compared to the average background-only case.

10.3 AGN Centaurus A

The nearest AGN, Centaurus A (Cen A), has been discussed as a potential source of ultra high energy CRs in the context of results from the Pierre Auger Observatory (PAO). The point source likelihood fit at the location of Cen A resulted in zero signal events in this analysis, setting an upper limit that is 5.3 times higher than the ν_μ prediction by [129] for the most optimistic case where the protons have a spectral index $\alpha_p = 3$.

10.4 PWN Crab Nebula

The Crab SNR originated from a stellar explosion just 2 kpc away, recorded in 1054 AD. The system now consists of a central pulsar, a synchrotron nebula, and a surrounding cloud of expanding thermal ejecta. Because of its relative brightness and steady emission, it is often referred to as the standard candle of high energy gamma ray astronomy. The pulsar continuously emits a wind of magnetized plasma, terminating in a standing shock front.

Figure 10.2 summarizes three different predicted fluxes and their respective 90%

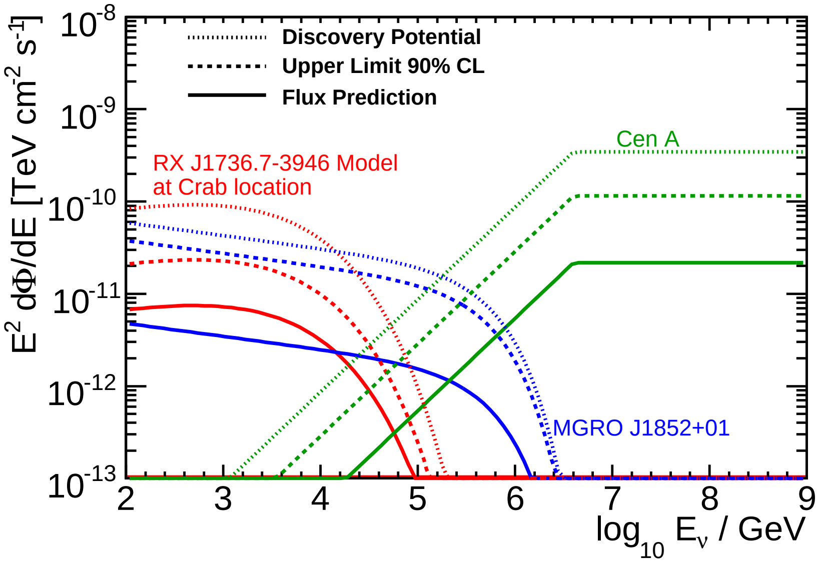

Figure 10.1: Differential flux of three theoretical models shown with the IceCube 40-string upper limit (90% CL) and discovery potential in each case. Shown are the $\nu_\mu + \bar{\nu}_\mu$ predictions of [128] for SNR RX J1713.7-3946 but moved to the location of the Crab Nebula, [31] for MGRO J1852+01, and [129] for Cen A under the most optimistic condition, where the protons have a spectral index $\alpha_p = 3$.

CL upper limits. The green line (solid) corresponds to the flux predicted in [130], using HESS measurements of the gamma ray spectrum, assuming it is dominated by photons from pion decay, and assuming no reprocessing in the source. If the first assumption is wrong, we will see many fewer neutrinos, and if the second assumption is wrong, many more. The black line represents the estimated flux based on a resonant cyclotron absorption model in [131]. The case shown uses the most optimistic Lorentz factor $\Gamma = 10^7$, where favored values are $\Gamma \sim 10^6$. The red and blue lines represent the two predicted fluxes from [132], for the cases of linear and quadratic acceleration, respectively. Both models are excluded at more than 90% CL.

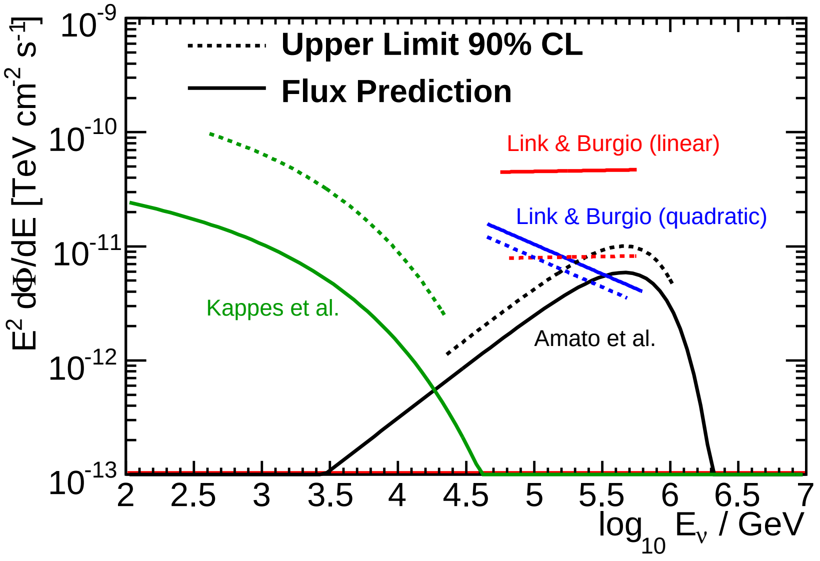

Figure 10.2: Predicted fluxes and upper limits on several models of the Crab. Solid lines indicate the predicted flux and dashed are the 90% CL upper limits. The green lines are the predicted flux and corresponding upper limit based on the model proposed in [130]. The red and blue lines correspond to the model in [132] for the cases of linear and quadratic proton acceleration. The black line represents the estimated flux for the most optimistic case proposed in [131] based on a resonant cyclotron absorption model.

10.5 Starburst Galaxies

Starburst galaxies were already presented as sources of interest in section 7.4. Recent detections [115, 116, 117] of very high energy photons from the nearest luminous starburst galaxies M82 and NGC 253, each characterized by star-forming regions with high supernova rates in the core, support the belief that the observed enhanced gamma ray emission is due to CR interactions. Under the assumption that the GeV–TeV photons originate from the decay of neutral pions produced when protons that are shock-accelerated by SNRs in the starburst core inelastically scatter against target hydrogen atoms with densities of the order of $100\,\mathrm{cm}^{-3}$ [133, 134], an order-of-magnitude calculation of the resulting flux of muon neutrinos based on [135] can be made. The muon neutrino upper limit from M82 is about 400 times higher than the rough prediction. For NGC 253 in the southern sky, the muon neutrino upper limit is about 6000 times higher than the prediction.

In figure 10.3, the photon flux of M82 from the decay of neutral pions nicely connects the Fermi and VERITAS data points over the entire high energy range. The muon neutrino flux resulting from the proton spectrum normalized to the observed gamma ray fluence is also shown. The ν_μ predictions for M82 would have to be 370 times higher to reach the sensitivity of this analysis, and the actual 90% upper limit from M82 is 420 times higher than the prediction. So it would be unexpected if this source, which dominates the starburst catalog, were to give an observable flux of neutrinos. Likewise, figure 10.4 shows the same spectra for NGC 253, where the sensitivity of this analysis is to a flux 4,600 times higher than the prediction and the actual 90% upper limit set is 6,200 times higher than the predicted fluxes. NGC 253 is located at $\delta = -25.29°$, in the down-going region where IceCube has limited sensitivity, whereas M82 is at a declination of $\delta = 69.68°$. It should be noted that for NGC 253, the HESS datapoint lies below the photon flux used to estimate the neutrino flux. Even so, we still follow the best-fit power law from [115] due to the higher statistics from Fermi data.

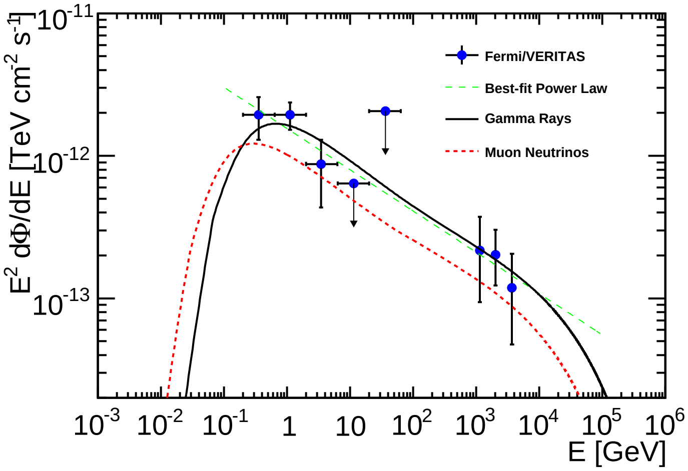

Figure 10.3: Differential flux of photons and muon neutrinos from pp interactions in M82 ($d\Phi_p/dE \propto E^{-\gamma}\exp(-E/E_\circ)$ with $\gamma \sim 2.3$ and $E_\circ \sim 10^3$ TeV). The gamma ray spectrum is normalized to the observed flux from Fermi and VERITAS. Data points and best-fit power law are taken from [115].

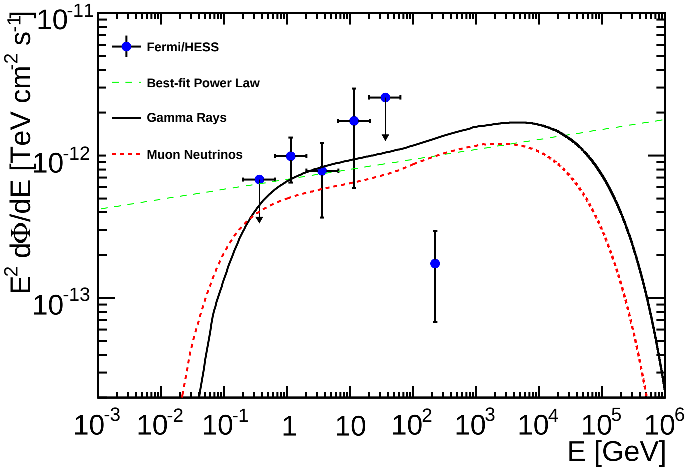

Figure 10.4: Differential flux of photons and muon neutrinos from pp interactions in NGC 253 ($d\Phi_p/dE \propto E^{-\gamma}\exp(-E/E_\circ)$ with $\gamma \sim 1.9$ and $E_\circ \sim 10^3$ TeV). The gamma ray spectrum is normalized to the observed flux from Fermi and HESS. Data points and best-fit power law are taken from [115].

Chapter 11

Conclusions

11.1 Summary

A search for sources of high energy neutrinos has been performed using data taken during 2008–2009 with the 40-string configuration of the IceCube Neutrino Observatory. Five searches were performed: (1) a scan of the entire sky for point sources, (2) a predefined list of 39 interesting source candidates, (3) stacking 16 sources of TeV gamma rays observed by Milagro and Fermi, along with an unconfirmed hot spot (17 total sources), (4) stacking 127 starburst galaxies, and (5) stacking five nearby galaxy clusters, testing four different models for the CR distribution. The searches were performed using a data set consisting primarily of up-going atmospheric neutrinos (northern sky) and higher energy down-going muons (southern sky) in a unified manner.

The most significant result of the five searches came from the all-sky scan with a p-value of 18%. The cumulative binomial probability of obtaining at least one result of this significance or higher in five searches is 63%. This result is consistent with the null hypothesis of background only. The sensitivity of this search using 375.5 days of

40-string data already improves upon previous point-source searches in the TeV–PeV energy range by at least a factor of two, depending on declination.

11.2 Outlook

Construction of the full IceCube detector has now finished, and all 86 strings of IceCube are in operation. This is a milestone for the field of neutrino astronomy. By combining data from the 40- and 59-string configurations, preliminary results already show a factor of 3 improvement in sensitivity. This combined analysis could be unblinded within the next month.

So far, the lack of a definitive signal is actually consistent with most reasonable predictions. The median upper limits presented suggest it will take at least two years with the full detector for a discovery. However, if the significance from certain directions, such as the hottest spot in the all-sky scan, continue to grow, it is possible to achieve a discovery sooner. Perhaps the most promising lead is from the stacking of six SNR seen in TeV gamma rays by Milagro (see Table 9.2).

For the standard IceCube ∼1–100 TeV energy range, there is only room for incremental improvement in the analysis technique itself. But significant strides in sensitivity are possible on either end of the energy spectrum.

The next IceCube analysis will use IceTop to veto down-going cosmic rays, lowering the energy threshold and improving the high energy sensitivity for very down-going events ($\theta < 30^\circ$). This technique is now practical since the IceTop sub-detector lowered its energy threshold, keeping even single hits. Also, improving the reliability of the simulation should lead to a better event reconstruction and selection. At high energy, it may be possible to distinguish between CR muon bundles and the single muons induced by neutrino interactions. This technique was tested in this work but abandoned because this level of detail was not well simulated and the potential sensitivity gain was relatively minor. Improvement in event reconstruction, particularly at high energy, is an active research area. Certainly, using a reconstruction that is aware of changing optical properties instead of only using average ice properties could lead to a better PSF.

For the lower energy range, the future lies with DeepCore, a new dense sub-array completely contained within the center of IceCube by three layers of veto strings from the sides and 30 DOMs (one-half the detector) from the top. Besides helping IceCube's low energy sensitivity, DeepCore also makes it possible to do low energy neutrino astronomy in the southern sky, an important hemisphere since it contains the galactic center and many nearby TeV gamma ray sources. The technique works by using the external layers of IceCube to veto CR muons and looking only for muons which are created by neutrino interactions inside the detector. Even down-going neutrinos created by CR interactions in the atmosphere can be vetoed because they are likely to have an accompanying muon.

As the IceCube collaboration continues to analyze data and improve upon these search techniques, they stand in a unique position to open a new window on our amazing universe.

Bibliography

[1] F. Reines and C. L. Cowan. The Neutrino. *Nature*, 1956.

[2] John N. Bahcall, Aldo M. Serenelli, and Sarbani Basu. New solar opacities, abundances, helioseismology, and neutrino fluxes. *The Astrophysical Journal Letters*, 621(1):L85, 2005.

[3] K. Nakamura et al. Review of particle physics. *J. Phys. G*, 37:075021, 2010.

[4] D.S. Harmer R. Davis, Jr. and K.C. Hoffman. Search for neutrinos from the sun. *Phys. Rev. Lett.*, 20:1205, 1968.

[5] Q. R. Ahmad et al. Direct evidence for neutrino flavor transformation from neutral-current interactions in the sudbury neutrino observatory. *Phys. Rev. Lett.*, 89(1):011301, Jun 2002.

[6] R. Diehl et al. Radioactive 26Al from massive stars in the Galaxy. *Nature*, 2006.

[7] G. Pagliaroli, F. Vissani, M. L. Costantini, and A. Ianni. Improved analysis of SN1987A antineutrino events. *Astropart. Phys.*, 31:163–176, 2009.

[8] W. David Arnett and Jonathan L. Rosner. Neutrino mass limits from sn1987a. *Phys. Rev. Lett.*, 58(18):1906–1909, May 1987.

[9] J. Arafune and M. Fukugita. Physical implications of the kamioka observation of neutrinos from supernova 1987a. *Phys. Rev. Lett.*, 59(3):367–369, Jul 1987.

[10] V. Hess. Uber beobachtungen der durchdringenden strahlung bei sieben freiballonfahrt. *Physikalische Zeitschrift*, 13:1084–1091, 1912.

[11] Barbara Wiebel-Sooth, Peter L. Biermann, and Hinrich Meyer. Cosmic Rays VII. Individual element spectra: prediction and data. 1997.

[12] J. G. Learned and K. Mannheim. High-energy neutrino astrophysics. *Ann. Rev. Nucl. Part. Sci.*, 50:679–749, 2000.

[13] Joerg R. Hoerandel. On the knee in the energy spectrum of cosmic rays. *Astropart. Phys.*, 19:193–220, 2003.

[14] Pierre Sokolsky. Observation of the GZK cutoff by the HiRes experiment and the Pierre Auger Observatory. *Mod. Phys. Lett.*, A23:1290, 2008.

[15] Julia K. Becker. High-energy neutrinos in the context of multimessenger physics. *Phys. Rept.*, 458:173–246, 2008.

[16] Tom Gaisser. *Particle Physics and Cosmic Rays.* Cambridge University Press, U.K., 1991.

[17] Oscar Adriani et al. An anomalous positron abundance in cosmic rays with energies 1.5-100 GeV. *Nature*, 458:607–609, 2009.

[18] J. Chang et al. An excess of cosmic ray electrons at energies of 300–800 GeV. *Nature*, 456:362–365, 2008.

[19] O. Adriani et al. Pamela measurements of cosmic-ray proton and helium spectra.

[20] R. Abbasi et al. Measurement of the Anisotropy of Cosmic Ray Arrival Directions with IceCube. *Astrophys. J.*, 718:L194, 2010.

[21] P. Abreu et al. Update on the correlation of the highest energy cosmic rays with nearby extragalactic matter. *Astropart. Phys.*, 34:314–326, 2010.

[22] Robert Lauer et al. Directional correlations between UHECRs and neutrinos observed with IceCube. 2010.

[23] Pijushpani Bhattacharjee and Gnter Sigl. Origin and propagation of extremely high-energy cosmic rays. *Physics Reports*, 327(3-4):109 – 247, 2000.

[24] V. Berezinsky, M. Kachelrieß, and A. Vilenkin. Ultrahigh energy cosmic rays without greisen-zatsepin-kuzmin cutoff. *Phys. Rev. Lett.*, 79(22):4302–4305, Dec 1997.

[25] Daniel J. H. Chung, Edward W. Kolb, and Antonio Riotto. Superheavy dark matter. *Phys. Rev. D*, 59(2):023501, Nov 1998.

[26] Dmitry V Semikoz and Gunter Sigl. Ultra-high energy neutrino fluxes: new constraints and implications. *Journal of Cosmology and Astroparticle Physics*, 2004(04):003, 2004.

[27] J. Abraham et al. Upper limit on the cosmic-ray photon flux above 1019ev using the surface detector of the pierre auger observatory. *Astroparticle Physics*, 29(4):243 – 256, 2008.

[28] Enrico Fermi. On the origin of the cosmic radiation. *Phys. Rev.*, 75(8):1169–1174, Apr 1949.

[29] D. Caprioli, E. Amato, and P. Blasi. The contribution of supernova remnants to the galactic cosmic ray spectrum. *Astropart. Phys.*, 33:160–168, 2010.

[30] A M Hillas. The origin of ultra-high-energy cosmic rays. *Annual Review of Astronomy and Astrophysics*, 22(1):425–444, 1984.

[31] Francis Halzen, Alexander Kappes, and Aongus O'Murchadha. Prospects for identifying the sources of the Galactic cosmic rays with IceCube. *Phys. Rev.*, D78:063004, 2008.

[32] A. A. Abdo et al. TeV gamma-ray sources from a survey of the galactic plane with Milagro. *Astrophys. J.*, 664:L91–L94, 2007.

[33] A. A. Abdo et al. Milagro Observations of TeV Emission from Galactic Sources in the Fermi Bright Source List. *Astrophys. J.*, 700:L127–L131, 2009.

[34] TeVCat. http://tevcat.uchicago.edu/.

[35] A. Achterberg et al. On the selection of AGN neutrino source candidates for a source stacking analysis with neutrino telescopes. *Astropart. Phys.*, 26:282–300, 2006.

[36] M. Blazejowski et al. A Multi-wavelength View of the TeV Blazar Markarian 421: Correlated Variability, Flaring, and Spectral Evolution. *Astrophys. J.*, 630:130–141, 2005.

[37] H. Athar, M. Jezabek, and O. Yasuda. Effects of neutrino mixing on high-energy cosmic neutrino flux. *Phys. Rev.*, D62:103007, 2000.

[38] Tamar Kashti and Eli Waxman. Flavoring Astrophysical Neutrinos: Flavor Ratios Depend on Energy. *Phys. Rev. Lett.*, 95:181101, 2005.

[39] Rikard Enberg, Mary Hall Reno, and Ina Sarcevic. High energy neutrinos from charm in astrophysical sources. *Phys. Rev.*, D79:053006, 2009.

[40] R. Abbasi et al. A search for a diffuse flux of astrophysical muon neutrinos with the icecube 40-string detector. In Preparation. To be submitted to Phys. Rev. D, 2011.

[41] R. Abbasi et al. Search for neutrino-induced cascades with five years of amanda data. In Preparation, 2010.

[42] M. Ackermann et al. Search for ultra high energy neutrinos with amanda-ii. *Astrophysical Journal.*, 675:1014, 2008.

[43] A. Achterberg et al. Multiyear search for a diffuse flux of muon neutrinos with amanda-ii. *Phys. Rev. D*, 76:042008, 2007.

[44] S. Biagi. Search for a diffuse flux of muon neutrinos with the antares telescope. Seminar at NEUTRINO 2010 Athens, Greece, 2010.

[45] R. Abbasi et al. First search for atmospheric and extraterrestrial neutrino-induced cascades with the icecube detector. In Preparation. To be submitted to Phys. Rev. D, 2010.

[46] S. Grullon. Searching for high energy diffuse astrophysical muon neutrinos with icecube. In *Proceedings from the Lake Louise Winter Institute*, 2010. arXiv:physics/1005.4962v4.

[47] S. Grullon. *A Search for a Diffuse Flux of Astrophysical Muon Neutrinos With the IceCube Neutrino Observatory in the 40-String Configuration*. PhD thesis, University of Wisconsin - Madison, 2010.

[48] I. Kravchenko et al. Rice limits on the diffuse ultrahigh energy neutrino flux. *Phys. Rev. D.*, 73:082002, 2006.

[49] J. Abraham et al. Limit on the diffuse flux of ultrahigh energy tau neutrinos with the surface detector of the pierre auger observatory. *Phys. Rev. D.*, 79:102001, 2009.

[50] R. Abbasi et al. An upper limit on the electron-neutrino flux from the hires detector. *Astrophysical Journal*, 684:790, 2008.

[51] P.W. Gorham et al. Observational constraints on the ultra-high energy cosmic neutrino flux from the second flight of the anita experiment. *Phys. Rev. D.*, 82:022004, 2010.

[52] R. Abbasi et al. Search for cosmogenic neutrinos with the icecube neutrino observatory. In Preparation. To be submitted to Phys. Rev. D, 2010.

[53] Raj Gandhi, Chris Quigg, Mary Hall Reno, and Ina Sarcevic. Ultrahigh-energy neutrino interactions. *Astropart. Phys.*, 5:81–110, 1996.

[54] Dmitry Chirkin and Wolfgang Rhode. Muon Monte Carlo: A high-precision tool for muon propagation through matter. 2004. hep-ph/0407075.

[55] T. Weiler. Resonant absorption of cosmic-ray neutrinos by the relic-neutrino background. *Phys. Rev. Lett.*, 49(3):234–237, Jul 1982.

[56] Thomas J. Weiler. Cosmic-ray neutrino annihilation on relic neutrinos revisited: a mechanism for generating air showers above the greisen-zatsepin-kuzmin cutoff. *Astroparticle Physics*, 11(3):303 – 316, 1999.

[57] J Jackson. *Classical Electrodynamics.* Wiley, 1998.

[58] M Longair. *High Energy Astrophysics Vol. 1.* Cambridge University Press, U.K., 1981.

[59] P. Cherenkov. Visible emission of clean liquids by action of radiation. *C. R. Ac. Sci. U.S.S.R.*, 8:451, 1934.

[60] P. Cherenkov. Visible radiation produced by electrons moving in a medium with velocities exceeding that of light. *Phys. Rev.*, 52:378–379, 1937.

[61] P. B. Price and K. Woschnagg. Role of group and phase velocity in high-energy neutrino observatories. *Astropart. Phys.*, 15:97–100, 2001.

[62] I. Frank and I. Tamm. Coherent radiation of fast electrons in a medium. *C. R. Ac. Sci. U.S.S.R.*, 14:107, 1937.

[63] M. Thunman, G. Ingelman, and P. Gondolo. Charm production and high energy atmospheric muon and neutrino fluxes. *Astroparticle Physics*, 5(3-4):309 – 332, 1996.

[64] Annalisa L'Abbate, Teresa Montaruli, and Igor A. Sokalski. Effect of neutral current interactions on high energy muon and electron neutrino propagation through the earth. *Astropart. Phys.*, 23:57–63, 2005.

[65] A. Achterberg et al. First year performance of the IceCube neutrino telescope. *Astropart. Phys.*, 26:155–173, 2006.

[66] Christopher Wiebusch et al. Physics Capabilities of the IceCube DeepCore Detector. 2009.

[67] Todor Stanev et al. Status, performance, and first results of the IceTop array. *Nucl. Phys. Proc. Suppl.*, 196:159–164, 2009.

[68] R. Abbasi et al. Calibration and Characterization of the IceCube Photomultiplier Tube. *Nucl. Instrum. Meth.*, A618:139–152, 2010.

[69] Hamamatsu Corp. R7081-02 Photomultiplier Tube Data. 2003.

[70] R. Abbasi et al. The IceCube Data Acquisition System: Signal Capture, Digitization, and Timestamping. *Nucl. Instrum. Meth.*, A601:294–316, 2009.

[71] Serap Tilav et al. Atmospheric Variations as observed by IceCube. *in Proc. 31st ICRC, Lodz*, 2010. arXiv:1001.0776.

[72] M. Ackermann et al. Optical properties of deep glacial ice at the South Pole. *J. Geophys. Res.*, 111:D13203, 2006.

[73] J. A. Aguilar et al. Transmission of light in deep sea water at the site of the Antares neutrino telescope. *Astropart. Phys.*, 23:131–155, 2005.

[74] S. L. Miller. Clathrate hydrates of air in antarctic ice. *Science*, 165:489, 1969.

[75] D. Chirkin. Study of the South Pole Ice Transparency with IceCube flashers. *IceCube internal reports*, 2009.

[76] S. Viola et al. Status of nemo project. *AIP Conference Proceedings*, 1213(1):249–251, 2010.

[77] Paschal Coyle. Neutrinos out of the (deep) blue-the status of underwater neutrino telescopes. *Journal of Physics: Conference Series*, 60(1):40, 2007.

[78] J. Ahrens et al. Muon Track Reconstruction and Data Selection Techniques in AMANDA. *Nucl. Instrum. Meth.*, A524:169–194, 2004.

[79] V. J. Stenger. Track fitting for the DUMAND-II Octagon Array. *External Report HDC-1-9, University of Hawaii at Manoa, Manoa, Hawaii, USA*, 1990.

[80] F. James and M. Roos. Minuit, a system for function minimization and analysis of the parameter errors and correlations. *Comp. Phys. Comm.*, 10:343, 1975.

[81] R. Abbasi et al. First Neutrino Point-Source Results From the 22-String IceCube Detector. *Astrophys. J.*, 701:L47–L51, 2009.

[82] R. Abbasi et al. Measurement of the atmospheric neutrino energy spectrum from 100 GeV to 400 TeV with IceCube. *submitted to PRD*, 2010. arXiv:1010.3980.

[83] R. Abbasi et al. Extending the search for neutrino point sources with IceCube above the horizon. *Phys. Rev. Lett.*, 103:221102, 2009.

[84] Francis Halzen, Alexander Kappes, and Aongus O'Murchadha. Gamma-ray Astronomy with Muons: Sensitivity of IceCube to PeVatrons in the Southern Sky. *Phys. Rev.*, D80:083009, 2009.

[85] Till Neunhoffer. Estimating the angular resolution of tracks in neutrino telescopes based on a likelihood analysis. *Astropart. Phys.*, 25:220–225, 2006.

[86] A. Hoecker et al. Tmva - toolkit for multivariate data analysis. 2009.

[87] D. Heck et al. CORSIKA: A Monte Carlo code to simulate extensive air showers. 1998. FZKA-6019.

[88] Askhat Gazizov and Marek P. Kowalski. ANIS: High energy neutrino generator for neutrino telescopes. *Comput. Phys. Commun.*, 172:203–213, 2005.

[89] H. L. Lai et al. Global QCD analysis of parton structure of the nucleon: CTEQ5 parton distributions. *Eur. Phys. J.*, C12:375–392, 2000.

[90] Anderson DZiewonski. Preliminary Reference Earth Model. *Phys. Earth Planet Int*, 25.

[91] G. D. Barr et al. A three-dimensional calculation of atmospheric neutrinos. *Phys. Rev.*, D70:023006, 2004.

[92] Morihiro Honda, T. Kajita, K. Kasahara, S. Midorikawa, and T. Sanuki. Calculation of atmospheric neutrino flux using the interaction model calibrated with atmospheric muon data. *Phys. Rev.*, D75:043006, 2007.

[93] A. D. Martin, M. G. Ryskin, and A. M. Stasto. Prompt neutrinos from atmospheric $c\bar{c}$ and $b\bar{b}$ production and the gluon at very small x. *Acta Phys. Polon.*, B34:3273–3304, 2003.

[94] Rikard Enberg, Mary Hall Reno, and Ina Sarcevic. Prompt neutrino fluxes from atmospheric charm. *Phys. Rev.*, D78:043005, 2008.

[95] Naumov V.A. Sinegovsky S.I. Zaslavskaya E.S. Bugaev, E.V. Prompt leptons in cosmic rays. *Nuovo Cim.*, C12:41, 1989.

[96] M. Ackermann and E. Bernardini. An investigation of seasonal variations in the atmospheric neutrino rate with the AMANDA-II neutrino telescope. 2005. astro-ph/0509330.

[97] Eun-Joo Ahn, Ralph Engel, Thomas K. Gaisser, Paolo Lipari, and Todor Stanev. Cosmic ray interaction event generator SIBYLL 2.1. *Phys. Rev.*, D80:094003, 2009.

[98] Johan Lundberg et al. Light tracking for glaciers and oceans: Scattering and absorption in heterogeneous media with photonics. *Nucl. Instrum. Meth.*, A581:619–631, 2007.

[99] R. Glasstetter and J.R. Hoerandel. Electron, muon and hadron size spectra of EAS in the ”knee” region. *Nuclear Physics B - Proceedings Supplements*, 75(1-2):238 – 240, 1999.

[100] P. Berghaus, R. Birdsall, P. Desiati, T. Montaruli, and J. Ranft. High energy and prompt neutrino production in the atmosphere. *J. Phys. Conf. Ser.*, 136:042019, 2008.

[101] G. D. Barr, T. K. Gaisser, S. Robbins, and Todor Stanev. Uncertainties in atmospheric neutrino fluxes. *Phys. Rev.*, D74:094009, 2006.

[102] R. Abbasi et al. Determination of the Atmospheric Neutrino Flux and Searches for New Physics with AMANDA-II. *Phys. Rev.*, D79:102005, 2009.

[103] Claude Amsler et al. Review of particle physics. *Phys. Lett.*, B667:1, 2008.

[104] Jim Braun et al. Methods for point source analysis in high energy neutrino telescopes. *Astropart. Phys.*, 29:299–305, 2008.

[105] Gary J. Feldman and Robert D. Cousins. A Unified Approach to the Classical Statistical Analysis of Small Signals. *Phys. Rev.*, D57:3873–3889, 1998.

[106] J. Neyman. Outline of a theory of statistical estimation based on the classical theory of probability. *Phil. Trans. Royal Soc. London, Series A*, 236:333–80, 1937.

[107] Jan Conrad, O. Botner, A. Hallgren, and Carlos Perez de los Heros. Including systematic uncertainties in confidence interval construction for Poisson statistics. *Phys. Rev.*, D67:012002, 2003.

[108] Gary C. Hill. Comment on 'Including systematic uncertainties in confidence interval construction for Poisson statistics'. *Phys. Rev.*, D67:118101, 2003.

[109] R. Abbasi et al. Search for Point Sources of High Energy Neutrinos with Final Data from AMANDA-II. *Phys. Rev.*, D79:062001, 2009.

[110] R. U. Abbasi et al. Search for Cross-Correlations of Ultra–High-Energy Cosmic Rays with BL Lacertae Objects. *Astrophys. J.*, 636:680–684, 2006.

[111] Julia K. Becker, Peter L. Biermann, Jens Dreyer, and Tanja M. Kneiske. Cosmic Rays VI - Starburst galaxies at multiwavelengths. 2009. arXiv:0901.1775.

[112] Kohta Murase, Susumu Inoue, and Shigehiro Nagataki. Very high energy cosmic rays and neutrinos from clusters of galaxies. *The Astrophysical Journal Letters*, 689(2):L105, 2008.

[113] John F. Beacom and Matthew D. Kistler. Dissecting the Cygnus Region with TeV Gamma Rays and Neutrinos. *Phys. Rev.*, D75:083001, 2007.

[114] M. C. Gonzalez-Garcia, Francis Halzen, and Soumya Mohapatra. Identifying Galactic PeVatrons with Neutrinos. *Astropart. Phys.*, 31:437–444, 2009.

[115] A. A. Abdo et al. Detection of Gamma-Ray Emission from the Starburst Galaxies M82 and NGC 253 with the Large Area Telescope on Fermi. *Astrophys. J.*, 709:L152–L157, 2010.

[116] V. A. Acciari et al. A connection between star formation activity and cosmic rays in the starburst galaxy m82. *Nature*, 462(7274):770–772, 2009.

[117] F. Aharonian et al. A search for very high energy gamma-ray emission from the starburst galaxy NGC 253 with H.E.S.S. *Astron. Astrophys.*, 442:177–183, 2005.

[118] C. A. Norman, D. B. Melrose, and A. Achterberg. The Origin of Cosmic Rays above 10 18.5 eV. *The Astrophysical Journal*, 454:60–+, November 1995.

[119] Hyesung Kang, Jorg P. Rachen, and Peter L. Biermann. Contributions to the Cosmic Ray Flux above the Ankle: Clusters of Galaxies. *Mon. Not. Roy. Astron. Soc.*, 286:257, 1997.

[120] Thomas H. Reiprich and Hans Boehringer. The mass function of an x-ray flux-limited sample of galaxy clusters. *The Astrophysical Journal*, 567(2):716, 2002.

[121] Christoph Pfrommer and Torsten A. Ensslin. Constraining the population of cosmic ray protons in cooling flow clusters with gamma-ray and radio observations: Are radio mini-halos of hadronic origin? *Astron. Astrophys.*, 426:777–777, 2004.

[122] Sergio Colafrancesco and Pasquale Blasi. Clusters of galaxies and the diffuse gamma-ray background. *Astropart. Phys.*, 9:227–246, 1998.

[123] V. S. Berezinsky, P. Blasi, and V. S. Ptuskin. Clusters of galaxies as storage room for cosmic rays. *The Astrophysical Journal*, 487(2):529, 1997.

[124] K. Kotera et al. Propagation of ultrahigh energy nuclei in clusters of galaxies: resulting composition and secondary emissions. *Astrophys. J.*, 707:370–386, 2009.

[125] Kohta Murase. Email regarding clusters of galaxies. private communication, 2009.

[126] A. Achterberg et al. Five years of searches for point sources of astrophysical neutrinos with the AMANDA-II neutrino telescope. *Phys. Rev.*, D75:102001, 2007.

[127] Paschal Coyle. The ANTARES Deep-Sea Neutrino Telescope: Status and First Results. *in Proc. 31st ICRC, Lodz*, 2010.

[128] G. Morlino, P. Blasi, and E. Amato. Gamma Rays and Neutrinos from SNR RX J1713.7-3946. *Astropart. Phys.*, 31:376–382, 2009.

[129] Hylke B. J. Koers and Peter Tinyakov. Relation between the neutrino flux from Centaurus A and the associated diffuse neutrino flux. *Phys. Rev.*, D78:083009, 2008.

[130] Alexander Kappes, Jim Hinton, Christian Stegmann, and Felix A. Aharonian. Potential neutrino signals from galactic cosmic-ray sources. *The Astrophysical Journal*, 656(2):870, 2007.

[131] Elena Amato, Dafne Guetta, and Pasquale Blasi. Signatures of high energy protons in pulsar winds. *Astron. Astrophys.*, 402:827–836, 2003.

[132] Bennett Link and Fiorella Burgio. TeV mu neutrinos from young neutron stars. *Phys. Rev. Lett.*, 94:181101, 2005.

[133] Elsa de Cea del Pozo, Diego F. Torres, and Ana Y. Rodriguez Marrero. Multimessenger model for the starburst galaxy m82. *The Astrophysical Journal*, 698(2):1054, 2009.

[134] Persic, M., Rephaeli, Y., and Arieli, Y. Very-high-energy emission from m. *A&A*, 486(1):143–149, 2008.

[135] S. R. Kelner, F. A. Aharonian, and V. V. Bugayov. Energy spectra of gamma rays, electrons, and neutrinos produced at proton-proton interactions in the very high energy regime. *Phys. Rev. D*, 74(3):034018, Aug 2006.

[136] A. A. Abdo et al. A Measurement of the Spatial Distribution of Diffuse TeV Gamma Ray Emission from the Galactic Plane with Milagro. *Astrophys. J.*, 688:1078–1083, 2008.

[137] Moskalenko et al. Galprop. http://galprop.stanford.edu/, 2010.

[138] Andrew W. Strong, Igor V. Moskalenko, and Vladimir S. Ptuskin. Cosmic-ray propagation and interactions in the galaxy. *Annual Review of Nuclear and Particle Science*, 57(1):285–327, 2007.

[139] Fermi Collaboration. Fermi lat background models. http://fermi.gsfc.nasa.gov/ssc/data/access/lat/BackgroundModels.html, 2010.

[140] G. Ingelman and M. Thunman. Particle Production in the Interstellar Medium. *Phys. Rev. D54*, 54:4385–4392, 1996.

[141] Torbjorn Sjostrand. High-energy physics event generation with PYTHIA 5.7 and JETSET 7.4. *Comput. Phys. Commun.*, 82:74–90, 1994.

Appendix A

Neutrinos from the Galactic Plane

This appendix describes a way to search for neutrinos from CR interactions with the interstellar medium. The technique is a straightforward modification to the unbinned point source analysis. The possibility for IceCube to see the flux from the galactic plane is presented.

The Earth lies about 8.5 kpc from the center of a fairly typical spiral galaxy of radius about 12 kpc. We observe the galaxy, in projection onto the sky, as a bright band, the Milky Way. IceCube, at the South Pole, is largely sensitive in the direction of the outer reaches, rather than toward the galactic center.

The galaxy has a typical interstellar medium (ISM) density of about 1 particle/cm^3 and magnetic field strength of 3–5 μG [12]. CRs diffusing through our galaxy will interact with the ISM producing secondary particles, including neutrinos and gamma rays (eqs. 1.10 – 1.13). Importantly, the neutrino flux will be proportional to the observed gamma ray flux. The very low density of the ISM ensures that the interaction lengths of the secondary particles are long compared to their decay length. This results in secondaries with the same spectrum as the CR primaries (eq. 1.3). Observations of these secondaries could be used to understand the distribution of CRs and their origin. The galactic plane emission, although small, also represents a foreground for other searches.

A.1 Observations of Neutral Pion Decay

The Milagro experiment has been used to detect the diffuse TeV gamma rays coming from the galactic plane [136]. With one exception, they observe good agreement between their data and the `GALPROP` model. `GALPROP` is a code for propagating CRs in the galaxy [137, 138], making assumptions about the distribution of CR sources. The agreement does not hold for the Cygnus region, where they report an excess over predictions from the `GALPROP` model. The excess in diffuse TeV gamma rays could be due to a local enhancement of CRs interacting to produce neutral pions and gamma rays.

The Fermi gamma ray space telescope has produced a very detailed map of the diffuse galactic plane emission [139]. The `GALPROP` model is used to separate the total gamma ray flux into its components: neutral pion decay, inverse Compton scattering, bremsstrahlung, and an isotropic extragalactic flux. Figure A.1 shows that the dominant component of the gamma ray flux near the galactic plane is caused neutral pion decay.

The Fermi model of galactic plane emission represents the background for many important searches, such as point sources and dark matter from the galactic halo. As such, it is a fairly detailed model. The model is based on three-dimensional surveys of atomic and molecular hydrogen, representing the dominant component of the CR flux. Since the CR flux is unknown except at the location of Earth, it is left as a free parameter and fit using the observed gamma rays [137]. The result of this fit and

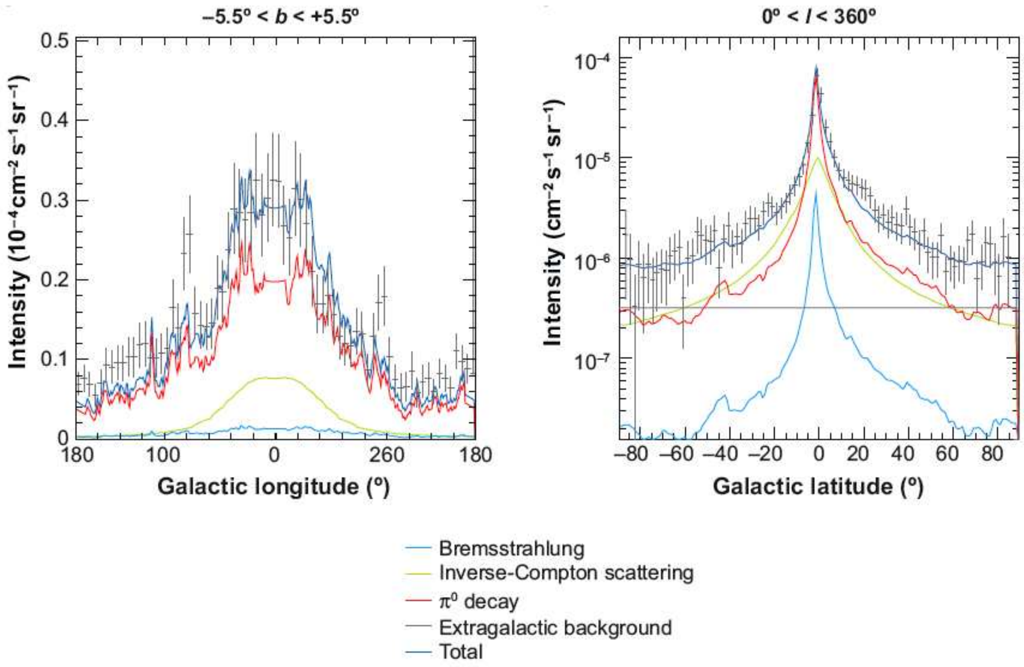

Figure A.1: Gamma ray longitude and latitude profiles for the `GALPROP` model, from [138]. EGRET data points are shown. Near the galactic plane, the model predicts a dominant contribution from neutral pion decay, induced by CR interactions with the ISM.

subtraction of the known sources and isotropic extragalactic flux is a two-dimensional model of the pion decay, shown in figure A.2. Inverse Compton and bremsstrahlung are actually included but contribute a relatively small amount near the plane, according to the `GALPROP` model. For the time being, we are concerned only with the shape of this distribution.

A.2 Search Method

Our goal is to perform a search for neutrinos coming from charged pion decay in the galactic plane. Since there is likely to be a charged pion for every neutral pion, we can simply use the two-dimensional Fermi model as a spatial PDF. Just

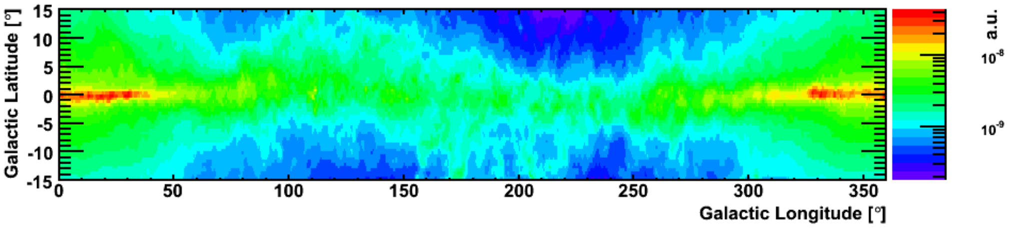

Figure A.2: Two-dimensional model of the Fermi diffuse gamma ray emission from the galactic plane, from [139]. Only the region within 15° of the plane is shown.

like the modification required for stacking in section 6.6, our signal PDF for the likelihood search is given by the convolution of the source PDF and our detector's two-dimensional Gaussian PSF. Each IceCube event has its own reconstructed angular uncertainty σ_{MPE} (determined from the shape of the muon track likelihood fit [85]), so the convolution is done for all possible values of σ_{MPE}. In practice, the largest value of σ_{MPE} allowed by the event selection is 3.0°, so the convolution is performed in bins of 0.1°, from 0° to 3°. The results of these numerical convolutions for the cases of $\sigma_{\mathrm{MPE}} = 0.0°, 1.0°, 2.0°$, and $3.0°$ are shown in figure A.3.

For the small-scale extended sources used in stacking ($\lesssim 3°$), the detector response is constant to a good approximation. For an extended source like the galactic plane that spans the whole sky, we must also consider the relative detector efficiency for each direction in order to determine how signal events will be distributed. Simulation is used to determine the detector efficiency in the same binning as galactic plane model, and the bin-by-bin product of these two-dimensional histograms is used as the spatial PDF in eq. 6.3.

The Fermi galactic plane model is also used as a PDF to simulate signal events.

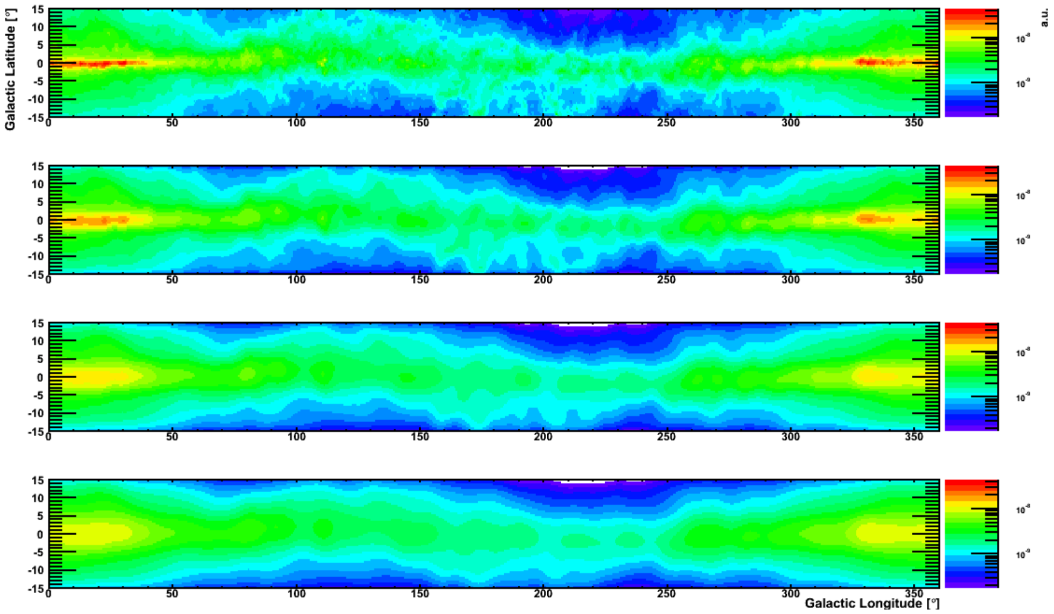

Figure A.3: The Fermi galactic plane model is convolved with the two-dimensional Gaussian PSF of IceCube events, represented by $\sigma_{\rm MPE}$, which ranges between 0° and 3°. The results of this convolution are shown (from top to bottom) for the case of $\sigma_{\rm MPE} = 0.0°, 1.0°, 2.0°$, and 3.0°. The fine structure of the model becomes washed out as the PSF of the events increases.

The sensitivity of this method was calculated in the same manner as the point source search and found to require a spatially integrated flux of $d\Phi/dE = 1.9\times10^{-7}\ \mathrm{TeV}^{-1}\mathrm{cm}^{-2}\mathrm{s}^{-1}\cdot(E/\mathrm{TeV})^{-2.7}$, corresponding to a Poisson mean of 64.6 events.

A.3 Simplified Galactic Model

The Fermi model does not directly give us the normalization for how many neutrinos to expect, although a calculation is possible. Neutrino production may be included in the predictions of `GALPROP` in the future, but at present they are not. For now, we use a flux prediction with some simplified assumptions given by Ingelman and Thunman [140].

They create a simplified three-dimensional model of the galaxy, taking the galaxy to be rotationally symmetric in the plane with a radius of 12 kpc and a constant density $\rho_0 = 1$ nucleon/cm^3 in the plane. Outside the plane, the density decreases as

$$\rho(h) = \rho_0 e^{-h/h_0}, \tag{A.1}$$

where h is the height above or below the plane and $h_0 = 0.26$ kpc. The Earth is in the plane a distance of 8.5 kpc from the center. The CR flux is taken to be the same as the flux observed at Earth throughout the entire galaxy. Particle interactions are modeled using `PYTHIA` [141].

A.4 Outlook for IceCube

The flux calculations of Ingelman and Thunman [140] described in the previous section yield a spatially integrated flux of $d\Phi/dE = 2.4 \times 10^{-8}$ TeV^{-1}cm^{-2}s^{-1} $\cdot$ $(E/\mathrm{TeV})^{-2.7}$, corresponding to a mean of 8 events in the final data sample of the 40-string configuration of IceCube. While exciting to realize that there are most likely events in the data sample that actually come from astrophysical neutrinos, it is important to realize that these events are about one-eigth as many as needed to reach the sensitivity of this analysis. Using that the sensitivity scales with the square-root of the number of signal events and assuming the full IceCube detector gives twice as many events, it would take 32 years of observing before the flux would reach our sensitivity.

There are, fortunately, numerous possible ways that the flux from the galactic plane could be observed sooner. The assumption of only a factor of 2 more events in the full detector was conservative, and studies using simulation and multi-variate cut strategies have shown that an additional factor of 2 improvement is possible by relaxing the condition that the events have a good PSF. For such an extended source as the galactic plane, the PSF matters less than in a point-source search. Using the DeepCore starting-event veto could greatly enhance the sensitivity, particularly because it opens the southern sky, which includes the galactic center, to low energy neutrino astronomy. Low energy sensitivity is important since the galactic plane flux is roughly $d\Phi/dE \propto E^{-2.7}$. Finally, the possibility to do a combined search with a detector in the Mediterranean Sea, such as KM3NeT, if built, could double the number of events. Even using the smaller, existing ANTARES detector could help greatly since it is most sensitive to the southern sky. With all of these enhancements, it could be possible to see the galactic plane in neutrinos in 5–10 years.